



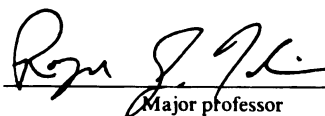


This is to certify that the  
dissertation entitled  
"CO on Pt(111) and Stepped Pt(335) Surfaces:  
Vibrational Stark Effect  
and Electron Energy Loss Investigation"  
presented by

Jih-Shiuan Luo

has been accepted towards fulfillment  
of the requirements for

Ph.D. degree in Physics

  
Major professor

Date November 12, 1992



**PLACE IN RETURN BOX to remove this checkout from your record.  
TO AVOID FINES return on or before date due.**

DATE DUE	DATE DUE	DATE DUE
_____	_____	_____
_____	_____	_____
_____	_____	_____
_____	_____	_____
_____	_____	_____
_____	_____	_____
_____	_____	_____

**MSU is An Affirmative Action/Equal Opportunity Institution**

c:\clrc\datedue.pm3-p.1

**CO ON Pt(111) AND STEPPED Pt(335) SURFACES: VIBRATIONAL STARK  
EFFECT AND ELECTRON ENERGY LOSS INVESTIGATION**

by

**Jih-Shiuan Luo**

**A DISSERTATION**

**Submitted to**

**Michigan State University**

**DOCTOR OF PHILOSOPHY**

**Department of Physics and Astronomy  
and Center for Fundamental Materials Research**

**1992**



## ABSTRACT

### CO ON Pt(111) AND STEPPED Pt(335) SURFACES: VIBRATIONAL STARK EFFECT AND ELECTRON ENERGY LOSS INVESTIGATION

BY

Jih-Shiuan Luo

Three experiments were designed to clarify the source of a surprising difference observed earlier between the vibrational Stark shift of two different atop C=O stretch modes, CO on the step edge and CO on the (111) terrace, on the stepped Pt(335) surface.

First, we found that the observed data of CO on Pt(335) cannot be explained by a difference in intramolecular structure between the two CO species -- a chemical mechanism. Our electron energy loss spectroscopy (EELS) measurements for CO on Pt(335) indicate that any such differences are too small to account for the data. Consequently, an alternative, physical mechanism has to be responsible. We found that the observed Stark effect of CO on Pt(335) results from strong screening of the static field at terrace sites, even though no difference in the screening of the IR field is observed.

Second, we developed a model for the populations of four CO species versus coverage for CO on Pt(335), which plausibly accounts for our EELS and temperature programmed desorption data. In this work bridge-bonded CO is first observed on this highly stepped surface.

Third, we used reflection absorption infrared spectroscopy (RAIRS) and electroreflectance vibrational infrared spectroscopy (EVS) to confirm that the

Stark shift of terrace CO on Pt(335) is significantly suppressed. The Stark shift of CO on Pt(111) is quite comparable to that of edge CO and is significantly bigger than that of terrace CO on Pt(335). In the same experiment, we observed that the screening effects for the IR field and the static field are fundamentally different. Most importantly, this result and the conclusion for CO on Pt(335) suggest that the present physical picture of electric field screening at surfaces is qualitatively wrong. We also found that our measured Stark shift of CO on Pt(111) in ultrahigh vacuum (UHV) is only one half that in electrochemical cells. Such a difference is possibly related to extra screening of the static electric field in UHV.

*To Chin-Yu*  
with whom it is so joyful to share life.

## ACKNOWLEDGMENTS

I am grateful to Professor Roger G. Tobin, my thesis adviser, for his insight, support, encouragement, and efforts to provide me with a complete Ph.D. training.

I would also like to thank Dr. David K. Lambert, my research advisor at General Motors Laboratories, who originally designed and built the infrared spectroscopic systems. I have benefited a great deal from working with him during the course of this research.

Contributions from Professor Tobin and Dr. Lambert are embedded throughout this work. Their desire for excellence and honesty were an education in themselves.

The EELS data shown in Chapters 4 and 5 were collaborative efforts with Dr. Galen B. Fisher and Craig L. DiMaggio. Because of their great skill in EELS measurement and helpful conversations, we were able to coax valuable information out of the very complicated adsorption system. The discovery of bridge CO on Pt(335) resulted from a collaboration with Dr. Frederick T. Wagner and Thomas E. Moylan. This important result stimulated more investigations for this work.

All experiments for this work were performed at GM Labs. I would like to thank GM researchers for their hospitality that made my stay at GM a pleasant experience. A few of them are particularly mentioned here. Dr. Pei-

Chung Wang provided friendship and morning (4 AM) coffee. Dr. Louis Green, Dr. Christopher M. Thrush, and Dr. Dale. L. Partin provided technical assistance and helpful conversations.

I would also like to express my gratitude to my parents for their efforts in educating me and mental support in these years.

Finally, my appreciation to my fiancée, Dr. Chin-Yu Yeh, is wholehearted. Her long-term companionship constantly jump starts my research momentum.

This work is partially supported by The Petroleum Research Fund, administered by the American Chemical Society, and the National Science Foundation under Grant # DMR-8815616.

## TABLE OF CONTENTS

LIST OF FIGURES.....	xi
LIST OF TABLES.....	xxiii
<b>1. INTRODUCTION.....</b>	<b>1</b>
References.....	8
<b>2. TECHNIQUES.....</b>	<b>9</b>
I. Introduction.....	9
II. Infrared Spectroscopy (IRS).....	11
1. General Requirements.....	11
2. Electroreflectance Vibrational Infrared Spectroscopy (EVS).....	14
(A) Introduction.....	14
(B) Experimental Set Up for EVS.....	15
(C) Quantitative Description for EVS.....	19
3. Polarization Modulated Reflection Absorption Infrared Spectroscopy (RAIRS).....	21
(A) Experimental Set Up for Polarization Modulated RAIRS....	21
(B) Quantitative Description for Polarization Modulated RAIRS.....	24

4.	Determination of Stark Tuning Rate.....	28
	(A) Spectral Analysis.....	28
	(B) Determination of Electric Field.....	31
III.	Electron Energy Loss Spectroscopy (EELS).....	34
IV.	Temperature Programmed Desorption (TPD).....	36
V.	Experimental.....	38
	1. Application of IRS and EELS.....	38
	2. Sample Preparation and Characterization.....	39
VI.	Summary.....	40
	References.....	57
3.	VIBRATIONAL STARK EFFECT AT SURFACES.....	60
	I. Introduction.....	60
	II. Stark Tuning Rate Theory.....	60
	III. Earlier Results of CO on Pt(335).....	64
	References.....	76
4.	VIBRATIONAL OVERTONES OF CO ON Pt(335): EVIDENCE FOR ANOMALOUS ELECTROSTATIC SCREENING.....	77
	I. Introduction.....	77
	II. Background.....	78
	III. Experimental.....	82
	IV. Results and Analysis.....	83
	1. Atop Overtone Intensity.....	83

2. Atop-Bridge Double Loss Intensity.....	90
V. Conclusion.....	91
References.....	103
 5. CO ADSORPTION SITE OCCUPATION ON Pt(335):	
A QUANTITATIVE INVESTIGATION USING TPD AND EELS.....	106
I. Introduction.....	106
II. Experimental.....	109
III. Results.....	109
1. TPD.....	109
2. EELS.....	111
IV. Model and Analysis of Site Occupation.....	112
1. Very Low Coverage ( $\theta \leq 0.12$ ).....	113
2. Low Coverage ( $0.12 < \theta \leq 0.22$ ).....	113
3. Intermediate Coverage ( $0.22 < \theta \leq 0.42$ ).....	114
4. High Coverage ( $\theta \geq 0.42$ ).....	114
V. Discussion.....	116
1. Comparison between Pt(335) and Pt(112).....	116
2. Effect of Annealing.....	119
VI. Summary.....	121
References.....	130



6.	ELECTRIC SCREENING IN AN ADSORBED LAYER: CO ON Pt(111).....	132
	I. Introduction.....	132
	II. Dipole-Dipole Screening.....	133
	1. The Standard Model.....	133
	2. Determination of $\alpha_v$ , $\alpha_e$ and $\tilde{U}(0)$ .....	139
	3. Summary.....	142
	III. Experimental.....	143
	IV. Results.....	144
	V. Discussion.....	146
	References.....	160
7.	CONCLUSION.....	164

## LIST OF FIGURES

### *Chapter 1*

- Figure 1-1.** 7  
Side view of the Pt(335) surface, showing atop adsorption sites for edge and terrace CO.

### *Chapter 2*

- Figure 2-1.** 41  
The reflection geometry showing the s and p components of an applied electric field  $\vec{E}$  with wavevector  $\vec{k}$ .
- Figure 2-2.** 42  
The surface electric field  $E/E_0$  in (a), and the quantity  $(E/E_0)^2/\cos\theta$  in (b) for platinum at  $2100\text{ cm}^{-1}$  ( $\epsilon = -375 - 200i$ ) as a function of the angle of incidence,  $\theta$  (Bradshaw and Schweizer [1]).
- Figure 2-3.** 43  
The image dipoles appearing on an adsorbed diatomic molecule oriented perpendicular and parallel to a metal surface.

**Figure 2-4.** **44**

Illustration of a process for obtaining RAIR spectrum from two scans of IR reflection measurements: scans with clean sample and with CO on the sample.

**Figure 2-5.** **45**

Illustration of a process for obtaining EVS spectrum by modulating the electrostatic field applied to the surface.

**Figure 2-6.** **46**

Schematic of the system used for electroreflectance vibrational infrared spectroscopy (EVS).

**Figure 2-7.** **47**

Optical system for RAIRS and EVS showing small mirror B (used as a beam splitter), detector D, electrode E, lens L, mirrors M, off-axis paraboloidal mirrors OAP, polarizers P, and sample S (Lambert [21]).

**Figure 2-8.** 48

Schematic diagram of computer-controlled wavemeter. Back-to-back hollow corner cube reflectors are mounted on a ball slide translation stage driven by a stepping motor. The stage moves freely except near the end of its travel where a beaded chain coupling becomes rigid and reverses its motion. A small mirror BS is used like a beam splitter before the detectors. Light from the diode laser is collimated using a mirror M and off-axis paraboloid (OAP) (Lambert [30]).

**Figure 2-9.** 49

Schematic of the system used for polarization modulated reflection absorption infrared spectroscopy (RAIRS).

**Figure 2-10.** 50

Optical E field with ellipsometric phase difference  $\Delta$  between s- and p-polarized light incident on the PEM.

**Figure 2-11.** 51

Normalized intensity vs horizontal displacement from the focal point on the sample surface.

**Figure 2-12.** 52

Measured and calculated capacitance between sample and spherical counter electrode vs. the gap  $d$  between them. Points are the measured

data on five different days and curve is the calculated capacitance. Agreement between the measured and calculated capacitance is discussed in the text.

**Figure 2-13.** 53  
Block diagram of an electron energy loss spectrometer.

**Figure 2-14.** 54  
Schematic diagram of the system for electron energy loss spectroscopy (EELS) (Sexton [35]).

**Figure 2-15.** 55  
Schematic of the system for temperature programmed desorption (TPD).

**Figure 2-16.** 56  
Geometrical  $c(4 \times 2)$  structure of CO on Pt(111).

### ***Chapter 3***

**Figure 3-1.** 72  
Polarization modulated RAIR spectra of CO on Pt(335) at 300 K obtained by Lambert and Tobin [6]. The CO coverages were 0.06, 0.5, 0.54, and 0.63 ML for spectra a - d, respectively; the determination of coverages is, however, partially incorrect as indicated in the text.

**Figure 3-2.** 73

EVS spectra of CO on Pt(335) at 300 K obtained by Lambert and Tobin [6]. Spectra a - d correspond directly to spectra a - d in Figure 3-1.

**Figure 3-3.** 74

Illustration of model's dipole-dipole coupling and Stark effect of CO on Pt(335). In the model, the electrostatic field shifts the vibrational frequency for edge CO but not for terrace CO. The Stark effect that increases the difference in frequency between the two CO species results in reduced dipole-dipole coupling. Such coupling transfers absorption intensity from edge into terrace CO mode. The EVS spectrum is then obtained by subtracting the RAIR spectrum without E field from that with E field.

**Figure 3-4.** 75

Comparison between the measured spectra at 0.54 ML and spectra calculated from the dipole coupling model discussed in the text and illustrated in Figure 3-3.

## ***Chapter 4***

**Figure 4-1.** 95

Side view of the Pt(335) surface, showing atop adsorption sites for edge and terrace CO.

**Figure 4-2.****96**

EEL spectra of CO on Pt(335) vs coverage. The sample was dosed with CO at 100 K, then annealed at 280 K for 1 minute to obtain an equilibrated layer. Spectra were measured with the sample at 100 K.

**Figure 4-3.****97**

Normalized EELS intensities for the three high frequency peaks, as a function of total CO coverage in monolayer (ML). The lines are linear fits to the data.

**Figure 4-4.****98**

Comparison of the measured intensity ratio  $I_{2a}/I_a$  (from Figure 4-3) with calculated intensities for various values of  $\beta_i$ . A value of  $\beta_i$  close to 1 is required for a chemical explanation of the Stark tuning rate. See the text for a detailed description of the calculation. (a) Calculations assuming  $\eta = 2$  (uncorrelated double loss scattering). Only values of  $\beta_i < 0.4$  are consistent with the data; the best fit is for  $\beta_i = 0.15$ . The dipole contribution  $I_{oa}/I_{2a}$  at saturation is 0.53, 0.98 and 1.00 for  $\beta_i = 0.15, 0.5$  and 1.0, respectively, compared to a range of 0.25 - 0.75 determined from off-specular EEL spectra. (b) Calculations assuming  $\eta = 1$  (fully correlated double scattering). The best fit is for  $\beta_i = 0.35$ .  $I_{oa}/I_{2a} = 0.98, 0.98$  and 1.00 for  $\beta_i = 0.35, 0.5$  and 1.0, respectively.

**Figure 4-5.****99**

Reduced chi-squared  $\chi^2_{\nu}$  as a function of  $\beta_i$ , for various values of the EELS sensitivity ratio  $f_2/f_1$  and for (a)  $\eta = 2$  and (b)  $\eta = 1$ . Values of  $\beta_i$  approaching unity are possible only for unrealistically small values of  $f_2/f_1$ .

**Figure 4-6.****100**

EEL spectra at saturation coverage (0.63 ML) in the specular direction and at three off-specular angles.

**Figure 4-7.****101**

EELS intensities of the elastic peak and four loss peaks as a function of off-specular angle, from Figure 4-4. (a) Uncorrected intensities, on a logarithmic scale. (b) Intensities  $I_a$ ,  $I_{ab}$ , and  $I_{2a}$ , normalized to their respective values in the specular direction, on a linear scale. The angular dependence of  $I_{2a}$  is intermediate between the dipole loss  $I_a$  and the double loss  $I_{ab}$ .

**Figure 4-8.****102**

Comparison of the intensity ratios (a)  $I_{ab}/I_a$  (from Figure 4-3) with bridge coverage  $\theta_b$  (from Chapter 5) and (b)  $I_{ab}/I_b$  with atop coverage  $\theta_a$ , as a function of total CO coverage. For uncorrelated scattering, the EELS and coverage data should have the same coverage dependence in



either plot. The data are too uncertain for a clear conclusion to be drawn.

## Chapter 5

**Figure 5-1.** 1 2 2

Proposed geometrical ( $\sqrt{3} \times \sqrt{3}$ )  $R30^\circ$  structure of CO on the (111) surface.

**Figure 5-2.** 1 2 3

(a) TPD spectra of CO on Pt(335) at various coverages. The overlayer was annealed to 280 K and cooled to 100 K before desorption. The individual spectra have CO coverages of (a) 0.015, (b) 0.026, (c) 0.053, (d) 0.10, (e) 0.13, (f) 0.17, (g) 0.21, (h) 0.30, (i) 0.42, (j) 0.46, (k) 0.56, (l) 0.58, and (m) 0.63 ML. (b) Typical two-component fit to the TPD data, at  $\theta = 0.58$  ML.

**Figure 5-3.** 1 2 4

(a) Points are coverages of edge and terrace CO as determined from the TPD data. The lines are from our model. (b) Ratio  $I_{ba}$  of atop to bridge EELS intensity versus total CO coverage. The right axis shows the corresponding population ratio  $\theta_b/\theta_a$ . Crosses were measured after annealing; open circles were measured after annealing to 280 K. The line is from our model. (c) Model's population of the four CO species versus total CO coverage; ta = terrace atop; ea = edge atop; tb = terrace bridge; eb = edge bridge.

**Figure 5-4.** 125

EELS spectra of CO on Pt(335) versus coverage. The sample was annealed to 280 K after dosing, then cooled to 100 K before the measurement.

**Figure 5-5.** 126

Possible structures of CO on Pt(335). (a) Edge structure with 2/3 of edge sites filled. (b) Proposed structure at  $\theta = 0.42$ . (c) Proposed structure at  $\theta = 0.22$ , showing partial occupation of terrace sites adjacent to the edge and possible tilting of edge CO. (d) Two possible structures at saturation ( $\theta = 0.63$ ).

**Figure 5-6.** 127

Sketch showing the addition of an atop molecule to the edge, accompanied by the displacement of one bridge CO to an adjacent atop site. Each additional molecule adds two atop COs and removes one bridge CO.

**Figure 5-7.** 128

Coverages of bridge and atop CO on Pt(111) versus total CO coverage, from ref. [14]. The lines are guides to the eye.

**Figure 5-8.** 129

Sketch to illustrate the tilting of CO on Pt(112). Adapted from ref. [4].

## Chapter 6

### Figure 6-1. 153

Sketch showing the partial cancellation of the applied field  $E_0$  due to the induced field from adsorbed molecules that are treated as polarizable points. This gives  $\gamma E_0$  to be the final field.

### Figure 6-2. 154

Illustration of the jellium edge and image plane. The jellium edge lies at  $a/4$  above the nuclei of the surface substrate layer;  $a$  is the lattice constant of the substrate. The position of the image plane and the spacing between the image plane and CO are discussed in the text (Persson and Liebsch [18]).

### Figure 6-3. 155

Vibrational spectra of the C=O stretch mode of atop  $^{13}\text{C}^{18}\text{O}$  on Pt(111) in UHV obtained with RAIRS. The CO coverages (in ML) are indicated. The curve is a smoothed fit to the data.

### Figure 6-4. 156

Vibrational spectra obtained with EVS that correspond to those in Figure 6-3. The measured  $S_E/\langle E \rangle$  is the fractional modulation of reflected intensity, normalized by  $E$  applied to the surface.

**Figure 6-5.**

157

Frequency  $\nu$  of peak IR absorption vs total CO coverage. Our measured  $\nu$  for  $^{13}\text{C}^{18}\text{O}$  have been multiplied by the factor 1.049 to compare with  $\nu$  for  $^{12}\text{C}^{16}\text{O}$  (to account for the isotope difference). The sources of data are: ● this work (200 K), + Hayden and Bradshaw in ref. [31] (95 K), □ Tushaus et al. in ref. [38] (125 K), Δ Beckerle et al. in ref. [27] (150 K), ▽ Beckerle et al. in ref. [27] (300 K), and × Olsen and Masel in ref. [33] (300 K).

**Figure 6-6.**

158

Integrated IR absorbance of CO vs total CO coverage. Our data are compared with previous experiments. The symbols have the same meaning as in Figure 6-5. A curve is fitted to our data as a guide to the eye. Different angles of incidence were used for the different experiments so exact agreement is not expected. In the plot, the data of Beckerle et al. (Δ) have been multiplied by a factor 0.5. The ratio of their intensity to ours, calculated as in Appendix of Ref. [43], is expected to be 1.14. The actual ratio is  $2.6 \pm 0.2$ .

**Figure 6-7.**

159

(a) Measured Stark tuning rate ( $d\nu/dE_0$ ) vs total CO coverage. Data were taken on three different days as indicated by the three symbols. The error bars are  $1\sigma$  random error + systematic error.

(b) Comparison between the coverage dependence of  $\gamma_{DC}$   $\square$  [from Figure 6-7a and Equation (26) and  $\gamma_{IR}$   $\bullet$  [from Figure 6-6 and Equation (25)]. We assume that  $e^*$  and  $dv/dE_{loc}$  are independent of coverage. Both  $\gamma_{DC}$  and  $\gamma_{IR}$  are normalized to the values measured on the same day with 0.5 ML of CO. Linear fits to both sets of data are shown.

## LIST OF TABLES

<b>Table 2-1.</b>	<b>38</b>
-------------------	-----------

Vibrational frequencies of two CO species vs. two different CO isotopes.

<b>Table 4-1.</b>	<b>94</b>
-------------------	-----------

Parameters used in the calculation of overtone intensities and Stark tuning rates for atop CO on Pt(335). Unless otherwise indicated, all parameters are assumed equal for edge and terrace CO. The nominal values represent our best estimates and were used for Figs. 4-6 and 4-7; the ranges represent the estimated uncertainties in the parameters. The parameters were varied over these ranges to test the sensitivity of the model. The dipole non-linearity parameter for edge CO,  $\beta_e$ , was determined from the Stark tuning rate  $dv/dE$ , through Equation (1). All values listed were determined from independent experiments, without reference to the present EELS data.

## CHAPTER 1

### INTRODUCTION

This work deals with the vibrational properties of a simple molecule (CO) adsorbed on both flat and stepped Pt surfaces, both with and without an applied electrostatic field. Through the use of a variety of experimental techniques, we have been able to characterize both the chemical and physical effects resulting from the presence of a monatomic step. We have shown, for the first time, that the step profoundly influences the local screening of applied electric fields in ways that are not foreseen by existing theories of surface electrodynamics. Furthermore, a careful study of screening on a flat surface reveals that even in that simpler case the electrodynamics is not well understood.

These studies are significant in a number of ways.

First, the discovery of large and unexpected electrostatic screening effects on both flat and stepped surfaces reveals that the current understanding of surface electrodynamics is still seriously incomplete. Both the near-surface response of conduction electrons in the metal and the screening due to the polarizability of other adsorbates need to be reexamined theoretically. Because stepped surfaces are far more difficult to study, both experimentally and theoretically, our discovery of screening anomalies on the flat Pt(111) surface is of particular importance.

Second, the study of stepped transition metal surfaces is important for understanding heterogeneous catalysis. Transition metals, such as platinum, are important catalysts in the petroleum and chemical industries and in pollution control. The study of regularly stepped surfaces is a step toward the understanding of real catalysts, which contain large concentrations of surface

defects, steps and kinks, which have a major impact on the catalytic activity of the surface [1,2,3]. In addition to providing new and surprising data on chemisorption on stepped surfaces, our work demonstrates the possibility of separating competing effects through a combination of experimental probes.

Third, the study of the response of adsorbates to electrostatic fields in ultrahigh vacuum (UHV) is important to the understanding of electrochemistry, in which large electrostatic fields are present at the surface. Because the metal/vacuum interface is much simpler than the metal/electrolyte interface, and because the fields in UHV experiments are much smaller, the results of UHV experiments are more easily understood. Previous measurements by Lambert [4] of CO on flat Ni surface provided support for prevailing models of the metal/electrolyte interface. Our results on Pt(111), however, are not in agreement with electrochemical data, as will be discussed in Chapter 6.

Finally, in a more speculative vein, the electric effects of CO on stepped surfaces are in principle applicable to the development of atomic scale electronic devices. Stroscio and Eigler [5] have demonstrated the ability to manipulate individual CO molecules on Pt(111) with a scanning tunneling microscope (STM) at 4 K. Because edge and terrace CO display dramatically different responses to an applied electrostatic field, one could envision a single CO molecule on a stepped Pt surface as a "bit" of information that can be "written" with an STM tip and "read" spectroscopically.

The immediate motivation for this work comes from a measurement of the Stark tuning rate (the ratio of shift in vibrational frequency to intensity of an applied electrostatic field) of CO on the stepped Pt(335) by Lambert and Tobin [6] using polarization modulated reflection absorption infrared spectroscopy (RAIRS) [4,7,8] and electroreflectance vibrational infrared



spectroscopy (EVS) [4,7,8]. These techniques, and the other surface probes used in this work, are described in Chapter 2. The Pt(335) surface is regularly stepped, with (111) terraces four atoms wide and (100) steps of monatomic height, as shown in Figure 1-1.

In their experiment, Lambert and Tobin [6] observed two CO species that adsorbed on (111) terrace sites and on step edges. They found that terrace CO is similar to CO on the flat (111) surface in vibrational frequency, dynamic dipole moment, and desorption temperature [6,9]. However, they observed that the response to the electrostatic field is at least ten times smaller for CO adsorbed on terraces than for CO adsorbed at edges, while the response to the infrared (IR) electric field is about the same for both species. A detailed summary of the experiment is presented in Chapter 3, along with a theoretical analysis of the vibrational Stark effect for adsorbates.

Two mechanisms can be proposed to account for these results. The first mechanism is physical: the small Stark tuning rate of terrace CO may be due to a much smaller local electrostatic field at terrace sites than at edge sites. However, both Lambert and Tobin [6] and Reutt-Robey et al. [10] found that the IR cross section for terrace CO is quite comparable to that of edge CO, implying that there is no significant difference in the screening of the IR field at the two sites. Standard models of screening at surfaces do not predict such strong screening, and they cannot account for a large difference between the screening of the IR and static fields. For example, a simple classical calculation by Greenler et al. [11] estimated that the field would be a factor 1.5 lower on the terrace than at the step edge, not nearly enough to account for the difference in Stark tuning rates.

The second possibility is a chemical mechanism: there could be a significant difference in intramolecular structure between CO adsorbed at the

two sites. In this case, the fields at the two sites could be nearly the same, and the small Stark tuning rate of the terrace CO would be caused by a change in its internal electronic structure. Specifically, as shown in Chapter 4, the nonlinearity of the dipole moment function would need to be significantly enhanced. A consequence would be an enhancement of the intensity of the first overtone of the CO stretch vibration for terrace CO compared to edge CO; this enhancement should be detectable through electron energy loss spectroscopy (EELS).

I performed three different investigations in order to determine which of these mechanisms accounts for the difference in Stark tuning rate between edge and terrace CO, and to explore the nature of that mechanism. I found that the dominant mechanism is screening; there is little difference in internal structure between the two CO species. I also found that surprising screening effects are not confined to stepped surfaces. Anomalous screening is also found on the flat Pt(111) surface, though the effects are more subtle.

Chapter 4 presents the results of EELS overtone measurements for CO on Pt(335). As mentioned above, a chemical difference between step and terrace CO should be revealed as an enhancement of the overtone intensity for terrace CO. No such enhancement was found; consequently, a significant difference in internal electronic structure is not likely. These results exclude the possibility of a chemical explanation for the difference in Stark tuning rates. We can therefore conclude that screening of the static field at terrace sites must be responsible.

Analysis of the overtone intensities requires knowledge of the concentrations of the different CO species on the surface. Our EELS data revealed [12] that all previous models [6,9,13] of CO adsorption on Pt(335) and similar surfaces had been incorrect in that they assumed only atop sites

(where CO is bonded on top of a single Pt atom) were occupied. We showed that there is also substantial occupation of bridge sites (where CO is bonded between two Pt atoms). At certain coverages, bridge-bonded CO accounts for more than 40% of the total. Through a quantitative analysis of EELS and temperature programmed desorption (TPD) data, I was able to develop a satisfactory model for the coverage of all four CO species (edge atop, edge bridge, terrace atop and terrace bridge) as a function of total CO coverage. This work is described in Chapter 5.

The third experiment, presented in Chapter 6, was a measurement of the Stark tuning rate of CO on the flat Pt(111) surface using RAIRS and EVS. The tuning rate on Pt(111) is similar to that of edge CO on Pt(335) and nearly ten times larger than that of terrace CO. The difference in tuning rates on the stepped surface therefore represents a suppression of the response at terrace sites, rather than an enhancement at edge sites. The tuning rate measured on Pt(111) in UHV, however, is only one half that inferred from electrochemical measurements. This is the first direct comparison of Stark tuning rates for the same adsorbate on the same surface in the two different environments, and suggests that models relating the two are less well understood than previously believed [4].

Since the Stark tuning rate depends on the screening of the static field, while the IR absorption intensity depends on the screening of the IR field, a comparison of the two can be used to test screening models. Standard models of dipole-dipole coupling between adsorbates, discussed in Chapter 6, predict that the screening of static and IR fields should be essentially the same. Measurements at different coverages of CO on Pt(111), however, show that there is a significant difference in the screening of the two fields. The discovery of anomalous screening in this relatively simple and intensively

studied system reinforces our conclusions for the more complicated (335) surface and provides a simpler platform for future experimental and theoretical studies of screening.

In summary, these measurements have determined the mechanism responsible for the surprising results of Lambert and Tobin [6], revealed significant deficiencies in the present understanding of surface electrodynamics, and demonstrated the power of EVS, in combination with other surface probes, to give new information about surface chemistry and physics.

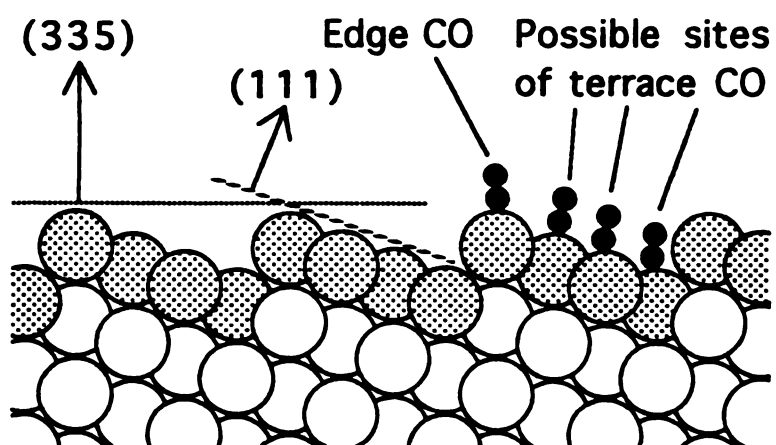


**Figure 1-1. Side view of the Pt(335) surface, showing atop adsorption sites for edge and terrace CO.**

## References

1. G.A. Somorjai, *Chemistry in Two Dimensions: Surfaces*, (Cornell University Press, Ithaca, New York, 1981).
2. L.K. Verheij, M.B. Hugenschmidt, L. Collin, B. Poelsema and G. Comsa, *Chem. Phys. Lett.* 166, 523 (1990).
3. M.A. Henderson and J.T. Yates, Jr., *Surf. Sci.* 268, 189 (1992).
4. D.K. Lambert, *J. Chem. Phys.* 89, 3847 (1988).
5. J.A. Stroscio and D.M. Eigler, *Science* 254, 1319 (1991).
6. D.K. Lambert and R.G. Tobin, *Surf. Sci.* 232, 149 (1990).
7. D.K. Lambert, *Phys. Rev. Lett.* 50, 2106 (1983).
8. D.K. Lambert, *Appl. Opt.* 27, 3744 (1988).
9. B.E. Hayden, K. Kretzschmar, A.M. Bradshaw and R.G. Greenler, *Surf. Sci.* 149, 394 (1985).
10. J.E. Reutt-Robey, Y.J. Chabal, D.J. Doren and S.B. Christman, *J. Vac. Sci. Technol. A* 7, 2227 (1989).
11. R.G. Greenler, J.A. Dudek and D.E. Beck, *Surf. Sci.* 145, L453 (1984).
12. J.S. Luo, R.G. Tobin, D.K. Lambert, F.T. Wagner and T.E. Moylan, *J. Electron Spectrosc. Relat. Phenom.* 54/55, 469 (1990).
13. M.A. Henderson, A. Szabo and J.T. Yates, Jr., *J. Chem. Phys.* 91, 7245 (1989).

## *Chapter 2*

# TECHNIQUES

### I. Introduction

Three surface-sensitive vibrational techniques were used in the experiments: two infrared spectroscopies (IRS), reflection absorption infrared spectroscopy (RAIRS) and electroreflectance vibrational infrared spectroscopy (EVS), and electron energy loss spectroscopy (EELS). The EVS technique is unique in being able to measure the Stark shift of adsorbates in ultrahigh vacuum (UHV). But the techniques RAIRS and EELS are widely used in modern surface analysis. Review articles for RAIRS and EELS are widely available, and remarks made in this chapter are largely based on several of these reviews [1,2,3,4,5,6,7].

So far, EELS is one of the most prevalent techniques used in surface vibrational spectroscopy. A monochromatic electron beam, 1-10 eV, is directed onto a surface and the energy distribution of the scattered beam is measured. More specifically, the impinging EELS electrons excite vibrational modes of adsorbates through short-range impact or long-range dipole interactions (more detailed discussion is presented below and in Chapter 3). The total energy of the EELS electrons is reduced due to these interactions. Information about the surfaces is then obtained by measuring the loss energy spectrum of the EELS electrons.

Among the reasons for the popularity of EELS are high sensitivity, making possible the investigation of partial monolayers on perfect single-crystal surfaces; large dynamic range; and commercial availability [4]. The

principal negative aspects of EELS are the UHV requirements, less reliable quantitative intensity and relatively poor resolution. By trading off the sensitivity, the best resolution that has been achieved with EELS is  $7.9\text{ cm}^{-1}$  [8] while for routine surface analysis it is degraded to around  $80\text{ cm}^{-1}$ . Although this is fine for species identification and fingerprinting (due to the limitation of resolution, two species with vibrational frequencies less than  $40\text{ cm}^{-1}$  apart are essentially indistinguishable [9,10]), it is inadequate for lineshape studies that are required for dynamic studies [4,11,12].

Instead of using electrons to interact with adsorbed molecules as in EELS, IRS uses photons. In IRS, the change in reflectivity with and without an adsorbate on the surface is measured. When surface analysis requires the precise measurement of vibrational frequency [13,14,15,16,17], width [12,18], intensity and the coverage-dependent shift of vibrational bands [13,14,19,20], IRS is the preferred technique due to its intrinsically high resolution. In addition, IRS gives information on the multiplicity of adsorption states [15,16,17], on lateral interactions and thus on adlayer growth and order-disorder phenomena [12], and on vibrational lifetimes and dephasing effects [4]. IRS has a further advantage: it is a "photons in and photons out" technique and is thus pressure-independent, making possible in situ experiments on single-crystal metal surfaces during heterogeneous reactions as well as on electrode surfaces. While the sensitivity of IRS is approximately the same as EELS, EELS still has some advantages over IRS: it is difficult to apply IRS at vibrational frequencies below  $1000\text{ cm}^{-1}$ .

In this chapter, descriptions of the two techniques are presented. The description is lengthier for IRS because we have used a diode laser as the IR source and because the technique is quite complicated. The IRS apparatus was designed and built by David K. Lambert; the techniques are well documented



in several papers [21,22,23,24]. Preliminary EELS work was done in collaboration with F. Wagner and T. Moylan, and more extensive work with G. Fisher and C. DiMaggio. While the GM Researchers made the actual EELS measurements, I performed extensive analysis of the spectra. Because I did not personally perform the measurements, the discussion about EELS will be short.

A short description of temperature programmed desorption (TPD), a widely used surface technique, is also presented. Mainly, TPD provides important information on adsorbate coverage and adsorption sites.

In the end, I briefly describe the process of sample preparation and characterization.

## **II. IRS**

### **II-1. General Requirements**

In IRS, our intention is to extract information about the interaction between the IR electromagnetic field and the oscillating dipole of the adsorbate associated with a particular normal vibration mode. In order to maximize the signal obtained from the rather small quantity of adsorbed molecules on metallic substrates, a careful choice of experimental conditions is required. One of the most important choices was first pointed out by Francis and Ellison [25]: only the p-polarized component of the IR beam incident on a metal surface is able to interact strongly with an adsorbate, and the interaction is enhanced at near-grazing incidence. The electric fields of s- and p-polarized radiation are perpendicular and parallel to the plane of incidence, respectively, as shown in Figure 2-1.

These considerations were first investigated theoretically by Greenler [26], who calculated the absorption intensity as a function of the angle of

incidence. The basis of Greenler's calculation is to consider the reflection of IR radiation from a clean and highly reflecting metal surface. The incident IR impinges at an angle  $\theta$  relative to the surface normal. In Figure 2-2, we demonstrate the dependence of the electric field strength  $E/E_0$ , on the angle of incidence,  $\theta$ , for both p- and s-polarized light at a platinum surface with  $\nu = 2000 \text{ cm}^{-1}$  [1]. Here,  $E_0$  is the amplitude of the electric field in the incident beam and  $E$  is the resultant amplitude at the surface. In Figure 2-2a, p-polarized light is further split into components  $E_{p\perp}$  and  $E_{p\parallel}$ , perpendicular and parallel to the surface, respectively. For p-polarized light, the field strength  $E/E_0$  increases with increasing  $\theta$ , reaching a maximum between 80 and 90° but falling rapidly to zero at 90°. The important quantity is really the total luminosity on the surface,  $(E/E_0)^2/\cos\theta$ . In Figure 2-2b, we plot the total luminosity for  $E_{p\perp}$ ; the other two components are at least 1000 times smaller [6]. It is clear that the parallel components are effectively screened. The metal surface that screens the parallel field will also screen out any dynamic dipole moment appearing on the molecule in a direction parallel to the surface. This can be visualized in Figure 2-3. Figure 2-3 shows two instantaneous dipoles, which are perpendicular and parallel to a metal surface. Because, for the dipole oriented normal to the surface, the image dipole is in the same direction, reinforcement occurs; for the parallel dipole, there is a very effective cancellation. Here, it is clear that only vibrations with a dynamic dipole moment perpendicular to the surface will be observed in IRS. This is the well known surface selection rule for metal surfaces [27,28]. Also, the interaction of an electric field with a dipole moment will only happen when the vector of the electric field has components parallel to the orientation of the dipole moment. This indicates that only  $E_{p\perp}$  needs to be considered for observing the vibrational spectrum of adsorbed molecules on a

metal surface. From Figure 2-2, it is clear that an angle of incidence between 80 and 90° will optimize the sensitivity of IRS.

At least two spectral scans are required for IRS. The first scan is of the clean metal and the second scan is of the metal surface with the adsorbate. The reflectivity change is then obtained by subtracting the spectrum of clean surface from that of the surface with adsorbate, as demonstrated in Figure 2-4; such a change is due to a vibrational interaction of adsorbate with light.

To measure the change in reflectivity, high signal/noise ratio with high stability is usually necessary. Such a change could be as small as 0.1% because the amount of molecule is usually less than a monolayer on the metal surface. The coverage could be less than 0.1 ML (1 ML corresponds to 1 adsorbate per surface substrate atom). Three different sources of apparent noise or instability can be introduced in IRS [6]. The first is the true noise associated with short-term fluctuations, such as photon shot noise, Johnson noise in the detector, and noise from additional electronic components such as amplifiers. Noise-like features in the spectrum can also arise from longer term drifts during the course of a scan. Such drifts are likely to be produced by slow changes in source temperature, detector responsivity, optical alignment, water vapor levels in the atmosphere, and similar factors. A third effect, obviously related to the second, is that of drifts over a yet longer time-scale in the interval between running the background spectrum and the adsorbate spectrum. How small a signal one can measure really depends on how well one can control or eliminate those unwanted noises or instabilities.

## II-2. EVS

### II-2(A) Introduction

The purpose of our experiments was to measure the Stark shift of CO on Pt surfaces. Two infrared spectroscopies are required: EVS and polarization modulated RAIRS (PS is used in Lambert's papers [21,22,23,24]). With EVS, the reflectivity change induced by an applied electric field is measured. With RAIRS, the change in reflectivity induced by an adsorbed gas is measured.

Only one scan is required to obtain an EVS spectrum. EVS detects the difference between the laser signal reflected from the sample with and without an electrostatic field. Because the change due to the applied field is quite small, EVS is a derivative technique. The EVS signal is very sensitive to the line shape of any vibrational mode. Essentially, only a vibrational mode with a sharp (narrow) line shape can be observed with EVS. There is a fundamental difference between the response of adsorbed molecules and that of gas phase molecules to the applied field: adsorbed molecules are oriented with respect to the field, while gas phase molecules are not. As a consequence, the response of adsorbed molecules is first order in the field while the response of gas phase molecules is second order. Also, there are eight orders of magnitude more adsorbed molecules than gas phase molecules at the area where the electric field is applied,  $2 \times 10^{-10}$  mole of adsorbed molecules at  $25 \text{ mm}^2$  and  $2 \times 10^{-18}$  mole of gas phase molecules in  $100 \text{ mm}^3$  at  $4 \times 10^{-10}$  torr. No EVS signal is received from bare metal because the resonant frequencies of substrate vibrations are out of the scanning range. So EVS is a zero background technique since only adsorbed molecules are detected.

The primary effect of an applied electrostatic field is to shift the frequency of the vibrational mode by on the order of  $10^{-3} \text{ cm}^{-1}$ . To observe

such a small frequency shift, the electric field is modulated and the signal from the detector is demodulated by a lock-in amplifier. The lock-in amplifier subtracts the signal without electric field from the signal with electric field. For a single mode, a derivative of the RAIRS spectrum is obtained as demonstrated in Figure 2-5. The combination of EVS and RAIRS provides a direct measurement of the Stark tuning rate  $dv/dE$  for adsorbed molecules, where  $\nu$  is the vibrational frequency and  $E$  is the applied field.

Using a diode laser is particularly important for EVS. The peak to peak EVS signal, with  $2.4 \times 10^3 V_{rms}$  and 0.4 mm between sample and electrode, could be as small as  $3 \times 10^{-6}$  normalized to the intensity of incident light for CO on Ni(110). A conventional thermal (blackbody) IR source is not bright enough to achieve this sensitivity, given the limited throughput achievable in an EVS experiment. Thus a stripe-geometry double-heterostructure diode laser, grown by molecular-beam epitaxy on a PbTe substrate with  $Pb_{0.9885}Eu_{0.0015}Te_{0.0019}Se_{0.9981}$  active region, is used. The diode laser can be tuned by controlling the laser current and heat-sink temperature and the optical power with single-mode frequency reaching the detector is in the range of 0.2 - 6  $\mu W$ .

## II-2(B) Experimental Set Up for EVS

The set up for EVS is demonstrated in Figure 2-6. Light from a tunable diode laser is reflected from the sample surface to an IR detector. Light reaching the detector is modulated both by a mechanical chopper and by the electric field applied to the surface. Two lock-in amplifiers are used to determine simultaneously the two modulation signals. The output from the lock-in in the upper channel is proportional to the intensity change induced

by the applied field, and the output from the lock-in in the lower channel is proportional to the total intensity of the IR beam. The ratio of the two lock-in outputs can eliminate the non-reproducibility in intensity of the diode laser.

The optical system used for both EVS and RAIRS is shown in detail in Figure 2-7. Not all the components shown are in place during EVS and RAIRS. Tiny mirror B (which serves as a beam splitter) and M3 are in place only during calibration of the laser with the wavemeter and are removed during EVS and RAIRS. Mirror M6 is in place only during alignment. With M6 removed, a visible laser beam, collinear with the IR beam, is used to check the position of the IR beam arriving at the sample, which is supposed to be underneath the electrode. The same visible laser beam is also used to determine the angle of incidence on the sample. In this study, the angle of incidence is about  $85^\circ$ . Once the optical alignment is set, the only change between operating RAIRS and EVS is adjusting the angle set up on polarizers P1 and P2.

The rms electric field applied to the sample is about  $3 \times 10^4$  V/cm. For EVS, the stronger the electric field  $E$  that is applied, the bigger the signal that is observed. However, if  $E$  is too large breakdown will occur. With a 0.4-mm gap between the sample and the 9.5-mm diameter spherical electrode, the breakdown field in vacuum ( $< 10^{-5}$  torr) is on the order of  $10^5$  V/cm.

The diode laser is stepped through a set of predetermined laser currents and heat sink temperatures; the current is about 0.1 Ampere and the temperature is slowly raised from about 70 to 100 K. This results in single-mode output. The frequency of each single mode is calibrated with the wavemeter [29]. The wavemeter, shown in Figure 2-8, is operated open loop under computer control and is essentially a variable path length Michelson interferometer in which the two separated beams reflect from back-to-back

corner cube reflectors carried by translation a stage. A beam splitter is used to combine the beam from the diode laser and the beam from a 0.6328- $\mu\text{m}$  He-Ne laser into a single collinear beam incident to the interferometer. The interferometer beam splitter is ZnSe coated for use at the Brewster angle in the 4-12-mm range and at 0.6328  $\mu\text{m}$ . Separate IR and visible light interferograms are obtained by using a small mirror to reflect visible light to a silicon photodiode, while transmitted IR light is focused on a HgCdTe detector. Two interferograms (IR and visible) form the input to a counter-timer used to determine their frequency ratio. The frequency of beam from the diode laser can be determined from the relationship [29]

$$\omega_{\text{IR}} = \omega_{\text{vis}} \frac{n_{\text{vis}}}{n_{\text{IR}}} \times \frac{f_{\text{IR}}}{f_{\text{vis}}}.$$

Here,  $f_{\text{IR}}/f_{\text{vis}}$  is the measured ratio of fringes from the IR laser to fringes from the He-Ne laser;  $n_{\text{vis}}$  and  $n_{\text{IR}}$  are the index of refraction of air at the He-Ne laser and the IR frequencies, respectively; and  $\omega_{\text{vis}}$  and  $\omega_{\text{IR}}$  are the frequencies of the visible and IR beams, respectively. The largest systematic error observed by Lambert was 0.034  $\text{cm}^{-1}$  [21] The frequency generated by the diode laser under single-mode lasing is quite reproducible: 95% of the frequencies differ by no more than 0.4  $\text{cm}^{-1}$  within 24 hours.

However, the laser intensity can vary by as much as 20% between successive scans (at the same operating condition). In repeating a scan through many modes, the change in reflectivity caused by the adsorbate is typically small relative to the change in detected intensity caused by the laser. For example, in the present study, the maximum change in reflectance caused by adsorbed CO is smaller than 10%. The variation in laser intensity between scans could change the spectral baseline and affect the quantitative analysis.

Consequently, to study adsorbate vibrations, a technique must respond to reflectivity changes without being sensitive to variations in source intensity. This is achieved in our experiments by using two simultaneous modulations to measure the total reflected intensity and the surface response separately.

Three important points about operating a diode laser should be mentioned here. (1) The direction of linear polarization of light from the laser can vary with laser operating conditions; a  $90^\circ$  variation has been observed in a previous study [21]. (2) The spectral range for a diode laser is limited. A given mode can be continuously tuned through a range of  $\approx 1 \text{ cm}^{-1}$ . (3) To study adsorbate vibrations, a much larger optical frequency range is needed. Our laser can be tuned through many modes with gaps  $\approx 1.5 \text{ cm}^{-1}$  to give the required range. The frequency of a single mode generated by the diode laser lies between  $1800$  and  $2050 \text{ cm}^{-1}$ .

We used a photoconductive HgCdTe detector with  $0.1 \text{ eV}$  bandgap,  $1\text{-mm}^2$  sensitive area, and  $60^\circ$  field of view to  $300\text{-K}$  blackbody radiation. The diode laser signal is very small compared to the background blackbody radiation. This detector, cooled by liquid nitrogen, has noise low enough to be dominated by the statistics of room-temperature blackbody radiation from the field of view. The linearity of the detector is then achieved owing two reasons: (1) we avoid saturating the detector, and (2) the detector signal is small.

The output of a detector staring at a tunable diode laser gives a spectrum of voltage versus electrical frequency that is dominated by  $1/f$  noise at low frequencies ( $\leq 10 \text{ kHz}$  [30]; the modulation frequencies for EVS and RAIRS are  $100 \text{ kHz}$  and  $76 \text{ kHz}$ , respectively.) At higher frequencies, the spectrum flattens out, and either detector noise or laser noise becomes the dominant noise source. In our experiment, the effect of current noise was negligible.



During EVS measurements, polarizers P1 and P2 are used to fix the direction of linear polarization so that only p-polarized light (required in order to observe the vibrational mode) is incident on the sample.

## II-2(C) Quantitative Description for EVS

The objective of EVS is to measure the effect of the electric field applied to the surface on the reflectivity  $R_p$  to p-polarized light. The measured effect will be described using the notation [21]

$$S_E = \frac{\text{rms variation of } R_p \text{ caused by } E}{R_p \text{ without } E}. \quad (1)$$

If  $f_E$  is the frequency of the ac electric field applied to the surface (100 kHz in the present case), then the rms voltage  $V(f_E)$  measured by the lock-in operating at  $f_E$  is [21]

$$V(f_E) = BI(f_E)D(f_E)T(f_E)\cos(\delta_E). \quad (2)$$

Here,  $B$  is the time average of the fraction of incident power transmitted by the mechanical chopper. Also,  $I(f_E)$  is the rms modulation at frequency  $f_E$  of the optical power incident on the detector when the optical beam is not blocked by the chopper,  $D(f_E)$  is the detector responsivity defined as (rms output voltage)/(rms optical power modulation),  $T(f_E)$  is the voltage transfer function of the circuitry between the detector and lock-in amplifier, and  $\delta_E$  is the difference in lock-in reference phase from the phase that would give the maximum output.

If  $f_C$  is the frequency at which the mechanical chopper interrupts the light, the rms voltage  $V(f_C)$  measured by the lock-in at  $f_C$  is [21]

$$V(f_C) = I_0GD(f_C)T(f_C)\cos(\delta_C). \quad (3)$$

Here,  $I_0$  is the power incident on the detector when the optical beam is not blocked by the chopper,  $G = (\text{rms optical power modulation at } f_c \text{ caused by the chopper})/I_0$ , and  $\delta_c$  is the difference in lock-in reference phase from the phase that would give the maximum output. From the above equations [21], we get

$$S_E = \frac{I(f_E)}{I_0} = \frac{G}{B} \frac{D(f_c)}{D(f_E)} \frac{T(f_c)}{T(f_E)} \frac{\cos(\delta_c)}{\cos(\delta_E)} \frac{V(f_E)}{V(f_c)}. \quad (4)$$

We used a chopper blade with two symmetrical blades with a 50% duty cycle. The chopper reduces the average intensity reaching the detector by a factor  $B = 0.50$  [21]. For a perfect square intensity versus time waveform,  $G = \sqrt{2}/\pi = 0.45$  [21].

The ratio of  $D(f_c)/D(f_E)$  has been measured by Lambert. He found that the data of  $D(f_c)$  versus  $f$  is well fit by the empirical equation [21]

$$D(f) = \frac{A}{f_D^2 + f^2}, \quad (5)$$

where to 90% confidence,  $169 \text{ kHz} < f_D < 220 \text{ kHz}$ . Here,  $f_D$  is the detector roll-off frequency. In the present experiment,  $D(f_c)/D(f_E) = 1.278 \pm 0.044$ .

The ratio of  $T(f_c)/T(f_E)$  is measured by replacing the detector by an attenuator with the same output impedance and comparing the rms voltage input to the network with the rms voltage output at  $f_E$  and  $f_c$ . The measurement gives  $T(f_c)/T(f_E) = 4.4 \times 10^{-7}$ , accurate to within 5%.

The effect of the phase  $\delta_E$  on the measured signal, proportional to  $\cos(\delta_E)$ , is measured by a comparison between the maximum signal with the phase set as for the spectra, and the maximum signal with the phase changed by  $90^\circ$ . The phase  $\delta_c$  can usually be set quite accurately. In most cases,  $\cos(\delta_c)/\cos(\delta_E) \approx 1$ .

Usually, only  $\cos(\delta_E)$  may change slightly. So,  $S_E$  in Equation (4) can be written as

$$S_E = \frac{5.1 \times 10^{-7} V(f_E)}{\cos(\delta_E) V(f_C)}. \quad (6)$$

A typical EVS spectrum of CO on Pt(111) is shown in Figure 6-4 of Chapter 6.

### II-3. Polarization Modulated RAIRS

#### II-3(A) Experimental Set Up for Polarization Modulated RAIRS

The set up for polarization modulated RAIRS is shown in Figure 2-9 [21]. A commercial zinc selenide photoelastic modulator (PEM) is used for this work. Briefly, A PEM is a transparent cubic crystal that, when unstressed, has an isotropic index of refraction. A periodic strain is induced in one axis of the crystal by driving it at the frequency of its fundamental longitudinal mode. This strain results in a periodically changing index of refraction for radiation polarized in that axis; this, in turn, causes a periodic phase retardation for radiation with that polarization. The polarization modulation technique has been used previously by several other groups [31,32], and is described in detail by Golden et al. [31]. In Figure 2-9, the upper channel lock-ins give the intensity difference of s- and p-polarized beams,  $(I_p - I_s)$ , and the lower channel lock-in gives the intensity sum of the two polarized beams,  $(I_p + I_s)$ . Because  $I_p$  and  $I_s$  are, on the average, attenuated to the same extent by randomly oriented gas phase molecules, but only  $I_p$  is attenuated by adsorbed surface species, presumably no reference scan is necessary for this technique. This technique gives the ratio  $(I_p - I_s)/(I_p + I_s)$ , allowing cancellation of the absorption by the randomly oriented molecules. The

resulting signal contains only the spectrum of the adsorbed surface molecules, and the non-reproducibility of diode laser beam is eliminated. However, a spurious signal is observed in lock-in (A), possibly due to an ambient blackbody radiation and modulated with the PEM frequency, and is removed by using an extra lock-in (B) referenced at the chopper frequency.

In practice, to obtain a useful polarization modulated RAIRS spectrum, it is still necessary to subtract a spectrum of the clean surface from a spectrum with the adsorbate present because of the variation (usually quite small) in polarization of the IR beam at different frequencies. Since polarization modulated RAIRS measures the difference in intensity between s- and p-polarized light, anything that changes that difference between the two spectra should be avoided. Sources of such irreproducibility include changes in the angle of incidence of light on the sample and changes in the polarization state of the light from the laser. Also, a change of the focal point of the light on the sample can cause the difference in reflectivity between s- and p-polarized light to vary and can therefore be a source of irreproducibility. Unfortunately, such a change is sometimes unavoidable. The sample position is believed to be slightly changed, for example, during the process of heating and recooling the sample to determine the coverage of adsorbates. A small change in sample position usually reveals a significant irreproducibility when subtracting two spectra.

The major source of noise seems to come from an effect of Fabry-Perot interference. The IR signal versus IR frequency varies in a cycle of  $1\text{ cm}^{-1}$ . The component that causes this interference is estimated to be  $5\text{ mm}/n$  thick ( $n$  is the index of refraction of the material causing such an effect). However, we have not been able to locate this component. This kind of noise is

significantly enhanced in spectra subtraction if the optical alignment is changed between RAIRS scans.

Polarizers P1 and P2 are used to reduce the maximum variation in polarization incident on the sample. The polarizers are set to reduce the maximum variation to  $1.8^\circ$  when the polarization of incident light is changed by  $90^\circ$  [21]. The PEM is oriented with its stress axis  $45^\circ$  from the direction of p-polarization.

The first step in the optical alignment procedure is the same for both EVS and RAIRS. We first set P1, P2, and P3 to transmit only p-polarized light. Then the PEM stress amplitude is set so that the detector voltage waveform, as monitored on an oscilloscope, is nearly sinusoidal at twice the stress oscillation frequency. The lock-in amplifier referenced to twice the stress oscillation frequency of the PEM is adjusted in phase to give maximum signal. During EVS, the PEM is turned off while the set up for the rest of the optical components remains the same. During RAIRS, polarizers P1 and P2 are rotated to null the signal from the lock-in referenced to PEM. A spectrum is obtained of the ratio of the two lock-in outputs for the clean surface. An adsorbate layer is prepared on the surface and a second spectrum is obtained of the ratio of the two lock-in outputs. The difference between the two spectra is proportional to the reflectivity change induced by the adsorbate layer. The PEM stress amplitude, with about 80-kHz stress frequency, has been kept constant since only a small frequency range is scanned.

### II-3(B) Quantitative Description for Polarization Modulated RAIRS

The objective of RAIRS is to measure the effect of adsorbed molecules on  $R_p$  (reflection of p-polarized light; changes in reflection of s-polarized light are also detected, but they are small.). The corresponding physical quantity will be denoted [21] as

$$\frac{\Delta R}{R} = \frac{R_p \text{ with CO} - R_p \text{ without CO}}{R_p \text{ without CO}}. \quad (7)$$

The optical system used for RAIRS is shown in Figure 2-7. In considering the effect of the PEM and polarizer P3 on transmitted light,  $I_s$  is the transmitted intensity with PEM turned off and with polarizer P3 set to pass only s-polarized light;  $I_p$  is the transmitted intensity with the PEM turned off and with polarizer P3 set to pass only p-polarized light;  $\Delta$  is the ellipsometric phase difference between the optical E fields of the s- and p-polarized light as shown in Figure 2-10 incident on the PEM;  $\phi(t)$  is the optical phase difference induced by the PEM between the component of transmitted light polarized along the stress axis and the orthogonal polarization state. The PEM is assumed to be oriented with its stress axis  $45^\circ$  from the direction of p-polarization. The intensity  $I(t)$  transmitted with polarizer P3 to pass p-polarized light is [21]

$$I(t) = \frac{(I_p + I_s)}{2} + \frac{(I_p - I_s)}{2} \cos[\phi(t)] + \sqrt{I_p I_s} \sin(\Delta) \sin[\phi(t)]. \quad (8)$$

The alignment procedure for RAIRS is described in section II-3(A). It involves polarizers P1 and P2, the phase of the lock-in amplifier, and the amplitude of stress oscillation in the PEM. Equation (8) can be used to justify the alignment procedure. With polarizers P1 and P2 set to pass only p-polarized light, Equation (8) becomes

$$I_+(t) = I_p \frac{(1 + \cos[\phi(t)])}{2}. \quad (9)$$

If we let  $f_M$  be the stress oscillation frequency of the PEM, the waveform of  $I_+(t)$  is most nearly sinusoidal at  $2f_M$  if the stress amplitude of the PEM is chosen so that [21]

$$\phi(t) = \pi \cos(2\pi f_M t). \quad (10)$$

Setting the reference phase of the lock-in amplifier (at  $2f_M$ ) to obtain maximum signal and P1 and P2 to pass p-polarized light makes the lock-in sensitive only to the  $\cos(4\pi f_M t)$  Fourier component of the signal, since the orthogonal reference phase gives

$$\int_0^\pi \cos[\pi \cos(x)] \sin(2x) dx = 0. \quad (11)$$

With lock-in reference phase and PEM amplitude set in this way, the lock-in output is independent of  $\Delta$  angle [21]. The term in Equation (8) that involves  $\Delta$  makes no contribution since

$$\int_0^\pi \sin[\pi \cos(x)] \cos(2x) dx = 0. \quad (12)$$

Consequently, the lock-in output is proportional to  $(I_p - I_s)$ , the difference in reflectivity between s- and p- polarized light incident on the PEM.

A complete measurement requires at least four scans of laser frequency. One essential scan is of the clean surface. The second essential scan is of the adsorbate covered surface. Calibration requires two additional scans that are not sensitive to the surface condition.

The surface sensitive scans will be discussed first. We define  $V(2f_M)$  as the rms voltage measured by a lock-in at reference frequency  $2f_M$ . Before

beginning, polarizers P1 and P2 are set to null  $V(2f_M)$  (at laser frequencies different from CO vibrational frequency). The rms voltage, output from lock-in A, can be written as [21]

$$V_A(2f_M) = \frac{(I_{0p} - I_{0s})}{2} D(2f_M) T(2f_M) \langle \Gamma(f_c) \rangle \{ \cos[\phi(t)] \} + S, \quad (13)$$

$$\text{with } \Gamma(f_c) = \begin{cases} 0 & 0 < 2\pi(f_c t) \leq 1/2 \\ 1 & 1/2 < 2\pi(f_c t) \leq 1 \end{cases}$$

Here, the step function  $\Gamma(f_c)$  originates from the signal chopped by a mechanical chopper. The detector responsivity  $D(2f_M)$  and the electrical transfer function  $T(2f_M)$  are defined as in Equation (4). The lock-in is operated at  $2f_M$ , so only the  $2f_M$  frequency component remains and, taking the rms, is denoted  $\{ \}$ . The last term,  $S$ , is a constant spurious signal, which may be caused by ambient radiation and may go through the PEM.

Lock-in B, referenced to  $f_c$ , serves as a filter to eliminate signals that are not chopped by the mechanical chopper. The spurious signal is thus removed. The rms voltage output from the lock-in B is

$$V_B(f_c) = \frac{(I_{0p} - I_{0s})}{2} D(2f_M) T(2f_M) \langle \cos[\phi(t)] \rangle T'(f_c). \quad (14)$$

Here,  $T'(f_c)$  is the electrical transfer function from lock-in A to lock-in B.

Similarly, if we define  $V_c(f_c)$  as the rms voltage measured by a lock-in C referenced to  $f_c$  during the null scan, then

$$V_c(f_c) = D(f_c) T(f_c) \left\langle \frac{(I_{0p} + I_{0s})}{2} + \frac{(I_{0p} - I_{0s})}{2} \cos[\phi(t)] \right\rangle \quad (15)$$

$$\approx D(f_c) T(f_c) I_{0p}.$$

At a frequency other than resonant frequency during the null scan, the intensities of the two polarized IR beams are essentially equal in that  $I_{0p} \approx I_{0s}$ ,



and  $(I_{0p} + I_{0s}) \gg (I_{0p} - I_{0s})$ . Here,  $D(f_c)T(f_c)$  is similar to  $D(2f_M)T(2f_M)$  but relates to a different frequency.  $\langle \rangle$  is the time average and  $I_{0p(s)}$  is the intensity transmitted by polarizer P3 with polarizers P1 and P2 set to null  $V(2f_M)$ . Finally, the ratio of the two lock-in rms voltages from surface sensitive scans is

$$Q_i = \frac{V_B(f_c)}{V_C(f_c)} = \frac{(I_{0p} - I_{0s})}{I_{0p}} \times \gamma, \quad (16)$$

$$\text{where } \gamma = \frac{D(2f_M)T(2f_M)\langle \cos[\phi(t)] \rangle T'(f_c)}{D(f_c)T(f_c)}.$$

Here,  $i$  refers to either "with CO" or "without CO" in Equation (16).

The calibration scans are made with polarizers P1 and P2 set to pass only p-polarized light. During one scan, both rms voltage referenced to  $2f_M$  and  $f_c$  are measured. During the other calibration scan, the PEM is turned off and only rms voltages referenced to  $f_c$  are measured. The rms voltage measured by the lock-ins at frequencies  $2f_M$  and  $f_c$ , respectively, with the PEM turned on can be written as

$$V_{B+}(f_c) = \frac{I_{+p}}{2} D(2f_M)T(2f_M)\langle \cos[\phi(t)] \rangle T'(f_c),$$

$$V_{C+}(f_c) = I_{+p} D(f_c)T(f_c) \left\langle \frac{1 + \cos[\phi(t)]}{2} \right\rangle, \quad (17)$$

$$Q_A = I_{+p} \gamma \left\langle \frac{2}{1 + \cos[\phi(t)]} \right\rangle.$$

Here,  $I_{+p}$  is the intensity incident on the detector with the PEM off and with polarizers P1 and P2 set to pass only p-polarized light. When the PEM is turned off,  $V_{C+}(f_c)$  becomes

$$V_{C+}(f_c) = I_{+p} D(f_c)T(f_c). \quad (18)$$

We actually measure the ratio of rms voltage with PEM turned on and off at reference frequency  $f_c$ :

$$Q_B = \frac{V_{c+}(f_c)_{\text{PEM on}}}{V_{c+}(f_c)_{\text{PEM off}}} = \left\langle \frac{1 + \cos[\phi(t)]}{2} \right\rangle. \quad (19)$$

In theory,  $Q_B$  can be calculated to be  $[1 + J_0(\pi)]/2 = 0.3481$  [21];  $J_0$  is the Bessel function of zero order. Experimental measurements of  $Q_B$  fall within 0.38 to 0.45. The measurement of  $Q_B$  is almost insensitive to frequency and may vary slightly from day to day. However, most importantly,  $Q_A \times Q_B$  is quite reproducible, differing no more than 10% from day to day.

As a consequence, we can rewrite Equation (7) as

$$\begin{aligned} \frac{\Delta R}{R} &= \frac{(I_{0p})^{\text{CO}} - (I_{0p})^{\text{clean}}}{I_{0p}} \\ &= \frac{Q_{\text{CO}} - Q_{\text{clean}}}{Q_A \times Q_B}. \end{aligned} \quad (20)$$

The difference in  $I_{0p}$  between the clean surface and the CO-adsorbed surface is negligible. Typical polarization modulated RAIR spectra of CO on Pt(111) is shown in Figure 6-3 of Chapter 6.

## II-4. Determination of Stark Tuning Rate

### II-4(A) Spectral Analysis

To determine the Stark tuning rate of adsorbed molecules, it is necessary to combine RAIRS and EVS. Both RAIRS and EVS measure an induced change in reflectivity for p-polarized light. The notation used for change in reflectivity  $R$  caused by CO adsorption or by applied E field is

$$\Delta_x = \frac{R(\text{with } X) - R(\text{without } X)}{R(\text{without } X)}. \quad (21)$$

Here,  $X$  is the effect causing the change. With RAIRS, the quantity  $\Delta_{CO}$  is measured as essentially

$$\Delta_{CO}(\nu, E=0) = \frac{\Delta R(\nu)}{R(\nu)}. \quad (22)$$

With EVS, the quantity  $S_E = \Delta_E$  is measured. For our purposes, we demonstrate the case with single-mode absorption only. With  $\Delta_{CO} = \Delta_{CO}(\nu, E)$ , the relation between  $\Delta_E$  and  $\Delta_{CO}$  can be written as

$$\frac{\Delta_E}{\langle E \rangle} = \frac{d\Delta_{CO}(\nu, E)}{dE} = \frac{\partial \Delta_{CO}(\nu, 0)}{\partial \nu} \frac{d\nu_0}{dE} + \frac{\partial \Delta_{CO}(\nu, E)}{\partial E}. \quad (23)$$

In Equation (23), the first term is the change of  $\Delta_{CO}$  due to a vibrational frequency shift by the applied field and the second term is the change in intensity of  $\Delta_{CO}$  at resonant frequency  $\nu_0$  caused by the applied field. For small electric fields, the derivatives can be evaluated at  $E=0$ . Note that  $(d\nu_0/dE)$  in the second term of Equation (23) is a constant. It is easier to compare the first term with the second term quantitatively in Equation (23) by integrating Equation (23) over frequency:

$$\frac{\int \Delta_E(\nu') d\nu'}{\langle E \rangle} = \left( \frac{d\nu_0}{dE} \right)_{E=0} \Delta_{CO}(\nu, 0) + \frac{\partial}{\partial E} \int \Delta_{CO}(\nu', E) d\nu' \Big|_{E=0}. \quad (24)$$

For CO on Ni and Pd, at frequencies near or above resonance ( $\nu \geq \nu_0$ ), the second term in Equation (24) has been shown to be a factor 50 smaller than the first [22,33]. In other words, the direct effect of the electric field on the IR intensity is much smaller than the indirect intensity change arising from the change in resonant frequency. Neglecting the second term, then the EVS signal becomes

$$S_E(\nu, E) = \Delta_E \approx \left( \frac{\partial \Delta_{co}(\nu, 0)}{\partial \nu} \frac{d\nu_0}{dE} \right) \langle E \rangle. \quad (25)$$

Here,  $(d\nu_0/dE)$  is the Stark tuning rate and  $S_E$  is the signal obtained from EVS measurement.

By integrating  $S_E$ , the relationship between EVS and RAIRS measurements becomes clear:

$$\int^{\nu} S_E d\nu' \approx \Delta_{co}(\nu, 0) (d\nu_0/dE) \langle E \rangle = \frac{\Delta R}{R} \langle E \rangle (d\nu_0/dE) \quad (26)$$

$$\int_{\nu_{\min}}^{\nu} d\nu \int^{\nu} d\nu' S_E \approx \langle E \rangle \left( \int_{\nu_{\min}}^{\nu} \frac{\Delta R}{R} d\nu \right) (d\nu_0/dE) \quad (27)$$

where  $\nu_{\min} < \nu_0 < \nu_{\max}$  is the scanning frequency range of the diode laser. That is, the first integral of  $S_E(\nu)$  is proportional to the RAIRS signal  $\Delta R/R$  (Equation (26)) and the second integral is proportional to the integrated RAIRS intensity (Equation (27)). Either relation provides a means of experimentally determining the Stark tuning rate  $(d\nu_0/dE)$ . In practice, we determine the Stark tuning rate in both ways: comparing absorption peak height and comparing absorption cross-section.

$$(d\nu_0/dE) \approx \int^{\nu} S_E d\nu' / \left( \frac{\Delta R(\nu_0)}{R(\nu_0)} \langle E \rangle \right) \quad (28)$$

$$(d\nu_0/dE) \approx \int_{\nu_{\min}}^{\nu} d\nu \int^{\nu} d\nu' S_E / \left( \langle E \rangle \int_{\nu_{\min}}^{\nu} \frac{\Delta R}{R} d\nu \right) \quad (29)$$

In principle, either way should produce the same Stark tuning rate. However, our diode laser spectrum has a gap of about  $1.5 \text{ cm}^{-1}$  following every  $1 \text{ cm}^{-1}$  continuous mode, meaning that parts of the vibrational line shape information are missing due to the gaps. In our analysis, we have applied the spline fit to fill these gaps. The Stark tuning rates obtained using the two methods usually differ by no more than 10%. Previously, the Stark tuning rates differed by as much as a factor of two when the gap appeared in the

crucial part of vibrational line shape. The gaps usually cause more uncertainty for EVS than for RAIRS.

#### II-4(B) Determination of Electric Field

From Equations (28) and (29), the quantity  $\langle E \rangle$  used to modulate the CO vibrational frequency during EVS must be known in order to determine the Stark tuning rate. In EVS, we actually measure the rms voltage between electrode and sample. To exactly determine  $\langle E \rangle$ , we must know several quantities.  $\langle E \rangle$  can be written as [22]

$$\langle E \rangle = \frac{\langle V \rangle}{d} \langle K \rangle \Lambda. \quad (30)$$

Here,  $\langle V \rangle$  is measured rms voltage during EVS,  $d$  is the distance between sample and electrode,  $\langle K \rangle (\langle V \rangle / d)$  is the effective field when the alignment is perfect, and  $\Lambda$  is the off-aligning factor for determining  $\langle K \rangle$ .

The electric field varies with position on the surface. To a good approximation of linear response, the reflectivity modulation caused by the actual electric field is the same that would be produced by a uniform "effective field",

$$E_{eff} = \frac{\int E(x) I(x) d^2x}{\int I(x) d^2x}. \quad (31)$$

The integration in Equation (31) is two dimensional. Here,  $I$  is the intensity profile of the IR laser beam and  $E$  is the externally applied electrostatic field. Determining  $I(x)$  involved translating a knife edge through the focus and measuring the change in detected light.  $E(x)$  also can be written as

$$E(x) = E_0 f(x). \quad (32)$$

Here,  $E_0 = E(0) = \langle V \rangle / d$  and  $f(x)$  can be calculated theoretically [22] as shown in Figure 2-11. With the center position of  $I(x)$  perfectly aligned with that of  $E(x)$ , shown in Figure 2-11,  $\langle K \rangle$  can be calculated as

$$\langle K \rangle = \frac{\int E(x)I(x)dx}{E_0 \int I(x)dx}. \quad (33)$$

The alignment between the center of the electric field and the center of IR intensity is not always perfect. This indicates that the actual  $\langle K \rangle$  is smaller by a factor of  $\Lambda$  since the maxima for both quantities locate on the center positions; where  $\Lambda$  can be written as

$$\Lambda = \frac{\int E(x + \Delta x)I(x)dx}{\int E(x)I(x)dx}. \quad (34)$$

Here,  $\Delta x$  is the deviation in position from the perfect alignment. We measure  $\Lambda$  by changing optical alignment to obtain an optimized EVS signal after concluding our EVS experiments. Consequently, we ratio the signal measured during EVS to the optimized signal to obtain  $\Lambda$ :

$$\Lambda = \frac{(S_E)_{\text{measured in EVS}}}{(S_E)_{\text{optimized}}}. \quad (35)$$

The sample-to-electrode rms voltage,  $\langle V \rangle$ , is measured using a capacitive voltage divider. The voltage divider was calibrated in three independent ways at the EVS modulation frequency by Lambert [22]. The largest fractional deviation from the mean was 5.6%.

Finally, we measure the distance,  $d$ , between sample and electrode by using a capacitance bridge. We measure a series of capacitances by varying  $d$ . We cannot obtain an absolute value of  $d$  but can determine relative positions from a micrometer on the sample manipulator. Absolute  $d$  is

determined by fitting experimental measurements of capacitance versus  $d$  into a theoretical calculation that assumes sample size is infinitely large [22]. Certainly, the real the sample size is limited to approximately 0.7 cm x 1.4 cm. However, the calculated capacitance versus  $d$  should match experimental measurements quite well when  $d$  is very small ( $d < 2$  mm). We convert our measurement of capacitance versus relative  $d$  into capacitance versus absolute  $d$ . The converted data at small  $d$  have nearly the same value as calculated data, as shown in Figure 2-12.

Figure 2-12 shows that our measured data do not fit well with the calculated curve; previous measurements on Ni samples by Lambert obtained a much better fit with the calculated capacitance [22]. We took measurements on the same Pt(111) sample more than 15 times, and some of the measurements were done by Lambert. The data are very consistent except for two measurements where the sample was found shorted to ground (the sample was short through defective electric wiring). The two anomalies are in surprisingly good agreement with the calculations. The spacing between sample and electrode was always visually checked. Spacing determined from our analysis was consistent with our visual estimates. Overall, we obtained at least 90% confidence with our measurements of  $d$ . The reasons for the deviation between our data and the calculations is not clear.

The uncertainty in  $d$  is a lot less than the discrepancy in Figure 2-12 suggests. The only thing we need from the capacitance measurements is to find where  $d = 0$ ; after that we can find the position from the micrometer reading. Since capacitance must diverge as  $d \rightarrow 0$ , good agreement between the measured data and the calculations at large  $d$  is not essential for the determination of  $d$ .

### III. EELS

Electron energy loss spectroscopy uses electrons as a means of excitation, as well as to carry information back from the surface. Therefore, not only must the analyzer be capable of high energy resolution, but the incident beam must be highly monochromatic; i.e., it must contain electrons within an energy window not broader than a few millielectron volts. No physical source of electron emission is known with such a narrow energy distribution. Therefore, spectrometers must use a thermionic or field emitter followed by an electron optical device that acts as a monochromator. The monochromator is typically followed by a lens system that allows the energy of the electrons at the target to be independently chosen from the monochromator pass energy. The basic configuration required for an EELS system is represented by a block diagram as shown in Figure 2-13. Briefly, thermal electrons at relatively high energy are retarded and focused into a dispersive monochromator where only a small fraction in a narrow energy band are transmitted. The monochromatized beam is then accelerated to the desired energy and focused onto the surface of interest at a relatively large angle of incidence,  $\theta_i$ , typically set at 45-70°.

For most of the vibrational measurements, we are interested only in electrons coherently reflected from the surface. In this way, scattered electrons experiencing essentially no momentum transfer are confined to a small cone about the specularly reflected beam ( $\theta_i = \theta_r$ ). To achieve high resolution, electrons inelastically scattered from the surface are retarded and focused into a second dispersive energy analyzer, usually, but not necessarily, of the same type as that in the monochromator. Finally, electrons



adventitiously scattered from the electron optical components and which would otherwise reach the electron detector should be suppressed.

The specific EELS system applied in our experiments is well documented by Sexton [34]. A schematic of the system is shown in Figure 2-14. It consists of two  $127^\circ$  cylindrical energy selectors (which act as monochromator and energy analyzer) with 35-mm mean radius, mounted in a fixed geometry. Electrons are accelerated from the hairpin tungsten cathode and focused by the einzel lens on the input slit of the monochromator. The monochromator selects an electron beam with energy width  $55\text{--}80\text{ cm}^{-1}$  that is accelerated onto the sample at a fixed angle of  $60^\circ$  from the normal and a variable energy of 2-5 eV. After reflection from the crystal surface, the beam is retarded and focused onto the entrance slit, which is scanned at constant resolution to reveal the beam profile and energy loss features. Exiting electrons are multiplied by a channeltron and counted as pulses. The half angle of acceptance (size of electron lobe allowed to go through the entrance slit) is  $1.5^\circ$ .

During operation, the monochromator is usually run continuously and the specimen surface is placed at the reflecting position and manipulated to find the reflected beam. Other electronic instruments are usually turned off to avoid flooding the energy loss spectrometer with electrons.

Spectral analysis is relatively straightforward. To obtain the cross-section of electrons interacting with an adsorbed molecule, the peak height of an observed vibrational peak in the EEL spectrum is normalized by the elastic peak height. The EEL spectral range is  $0\text{--}4500\text{ cm}^{-1}$  and the resolution is  $60\text{--}80\text{ cm}^{-1}$ . A typical EEL spectrum is shown in Figure 4-2 of Chapter 4.

## IV. TPD

Temperature programmed desorption (TPD) is a technique to measure desorption that yields equilibrium adsorption information. In the case of CO on Pt(111) at saturation coverage, adsorbed CO starts to desorb from the surface into vacuum at sample temperatures above 300 K. The schematic set up for TPD is shown in Figure 2-15. In TPD, we heat up the sample at a constant rate. Higher sample temperature can significantly increase the probability for adsorbed molecules to escape from the surface. In the case of CO on Pt(111), a simple estimate indicates that the probability of CO desorption increases by factor of 10 at 300 K compared to 200 K; this is discussed in more detail below. The desorption causes the pressure in the UHV chamber to increase and a mass spectrometer is used to measure the increase in partial pressure caused by the desorbed CO. With an ideal pump of infinite efficiency, we find the relation between the change of pressure and desorption rate to be [35]

$$p^* \propto -d\theta/dt, \quad (36)$$

$$\text{where } p^* = p - p_0 \text{ and } T = T_0 + \beta t.$$

Here,  $\theta$  is coverage of CO;  $p_0$  and  $p$  are baseline pressure and pressure measured during TPD, respectively;  $T_0$  is initial temperature before TPD; and  $\beta = dT/dt$  is heating rate. We then can construct a plot of pressure change  $p^*$  versus temperature  $T$ , and information on relative coverage is obtained by integrating the total area under the desorption curve as indicated below:

$$\int_{T_0}^{T_f} p^* dT \propto \int_{T_0}^{T_f} -\frac{d\theta}{dt} dT = \int_{\theta_0}^0 -\left(\frac{dT}{dt}\right) d\theta = \beta \theta_0. \quad (37)$$

Here,  $T_0$  and  $T_f$  are the beginning and end, respectively, of the temperature ramp and  $\theta_0$  is initial (total adlayer) coverage before TPD.

Absolute coverage is usually obtained by some other techniques. One example is to combine LEED and vibrational spectroscopic measurements. For CO on Pt(111), coverage of one CO molecule for every two Pt atoms is determined by: (1) a LEED pattern that indicates a  $c(4 \times 2)$  structure, and (2) EELS spectra that indicate two species, atop and bridge CO, on Pt(111) [36]. One can reconstruct the structure based on the information indicated above. The result is shown in Figure 2-16 and gives a coverage of "one CO per two Pt atoms". The other absolute coverages are then obtained by comparing TPD results with that of known coverage.

A useful equation that is associated with the rate of desorption from unit surface area is shown in the following [35,37]:

$$\frac{dp^*}{dT} + \frac{p^*}{\beta\tau} = \frac{\nu_n \theta^n \exp(-E_d/kT)}{\beta\theta_0}, \quad (38)$$

where  $n$  is the order of the desorption reaction,

$\nu_n$  is the pre-exponential factor,

$\tau$  is associated with pumping speed. ( $\tau \rightarrow 0$  for an ideal pump and the second term in LHS becomes dominant.),

and  $E_d$  is the activation energy of desorption (kcal/mole).

In the left-hand side of Equation (38), the first term is usually much smaller than the second term and negligible. Later, we will use Equation (38) to fit TPD spectra and to determine coverage of edge and terrace CO species on Pt(335). This will be discussed in detail in Chapter 5.

Species identification is a secondary function of TPD. Adsorbates at different sites may have different activation energies. However, such differences are not usually big enough to be distinguished in the TPD spectrum; atop and bridge CO on Pt(111), for example. For CO on Pt(335), two

distinctive desorption features are observed and identified as terrace and edge CO [16,17]. More detail is presented in Chapter 5.

## V. Experimental

### V-1. Application of IRS and EELS

To detect the C=O stretch mode on Pt surfaces, we can use either  $^{12}\text{C}^{16}\text{O}$  (effective mass = 6.857 amu) to detect bridge CO or  $^{13}\text{C}^{18}\text{O}$  (effective mass = 7.548 amu) to detect atop CO, as indicated in Table 2-1. Due to the limitation in frequency range of our diode laser (1800-2050  $\text{cm}^{-1}$ ), we can only detect one CO species using a single isotope. Despite the limitation in frequency range, the two IRS techniques provide detailed spectral information and unique information about the Stark effect of adsorbed molecules on surfaces.

EELS is used to study CO on Pt(335) because it is necessary to detect bridge and atop CO modes simultaneously. Also, we have used EELS to measure the overtone intensity of CO on Pt(335), which requires a much wider spectral range and is not accessible by using our diode laser.

**Table 2-1**

Vibrational frequencies of two CO species vs. two different CO isotopes.

isotope/species	atop CO frequency	bridge CO frequency
$^{12}\text{C}^{16}\text{O}$	2090-2105 $\text{cm}^{-1}$	1850-1890 $\text{cm}^{-1}$
$^{13}\text{C}^{18}\text{O}$	1992-2006 $\text{cm}^{-1}$	1760-1800 $\text{cm}^{-1}$

## V-2. Sample Preparation and Characterization

Pt crystals with (335) and (111) surface orientations were mounted in two separated UHV chambers equipped with EELS and IRS, respectively.

The Pt(335) was oriented to within  $0.5^\circ$  using Laue X-ray diffraction. The sample was spot welded to two Ta wires, which were also used for heating. The sample was cleaned by sequential cycling in oxygen between 600 K and 1000 K,  $\text{Ar}^+$  ions sputtering at 300 K and annealing at 1275 K. Sample cleanliness was carefully checked by both Auger spectroscopy and EELS.

The Pt(111) crystal was also oriented to within  $0.5^\circ$  using Laue X-ray diffraction. The sample was cleaned in cycles of oxygen treatment and Ar sputtering. Sputtering was performed at room temperature for one to two hours with Ar pressure at above  $5 \times 10^{-5}$  torr. The kinetic energy of  $\text{Ar}^+$  ions is about 600 eV and the ion current reaching the sample is about 1  $\mu\text{A}$ . The sample was then annealed at 1350 K for 3 minutes after sputtering. Oxygen treatment was performed at 1000 K with oxygen pressure at greater than  $5 \times 10^{-7}$  torr for about 20 minutes, and the sample was then annealed at 1375 K for 30 minutes to 1 hour. Auger spectroscopy was used to ensure sample cleanliness before the CO was adsorbed. The sample was checked repeatedly until the Auger peak height ratio of O(503)/Pt(237) was smaller than about 5% (noise level). The width of the C=O stretch vibrational line was found to be even more sensitive to surface preparation; the sample was cleaned until no further reduction in line width was seen. With the sample fully cleaned, and with 0.5 ML CO coverage, the FWHM line width at 200 K was  $\approx 3.5 \text{ cm}^{-1}$ .

## **VI. Summary**

Techniques necessary to obtain diode laser vibrational spectra with both polarization modulated RAIRS and EVS have been discussed in detail. A technique to obtain electron energy loss spectroscopy has also been discussed. Advantages and disadvantages of using IR and electron techniques were compared. Finally, descriptions of temperature programmed desorption and sample preparation and characterization were presented.

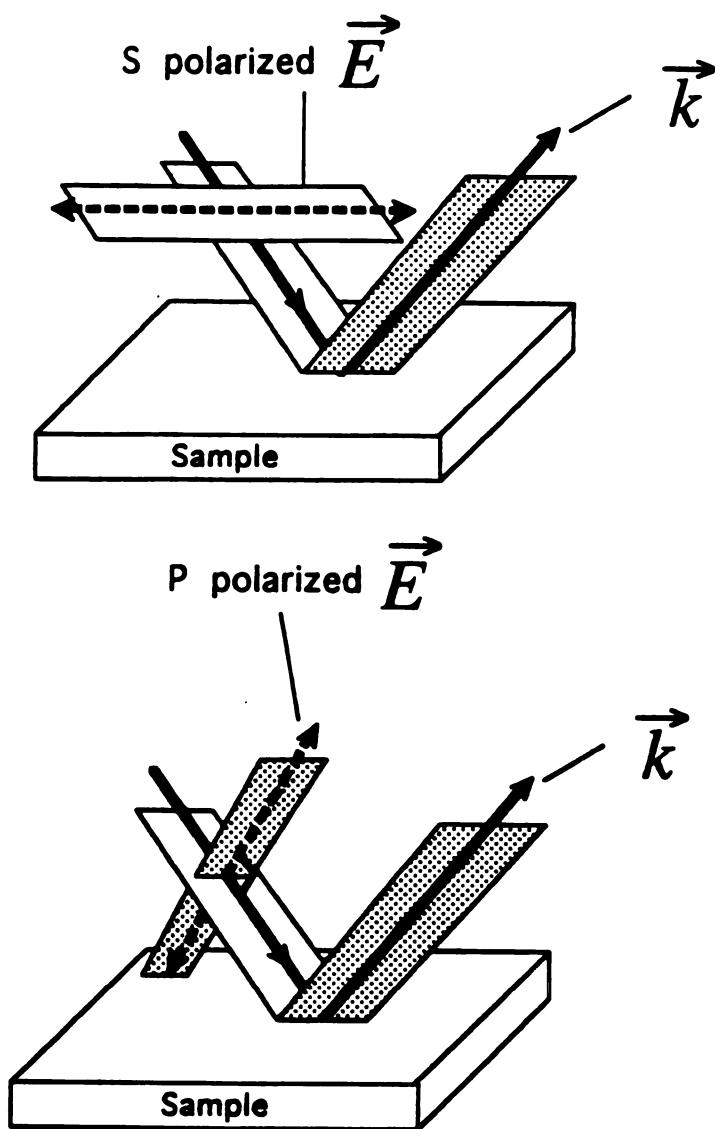


Figure 2-1. The reflection geometry showing the s and p components of an applied electric field  $\vec{E}$  with wavevector  $\vec{k}$ .

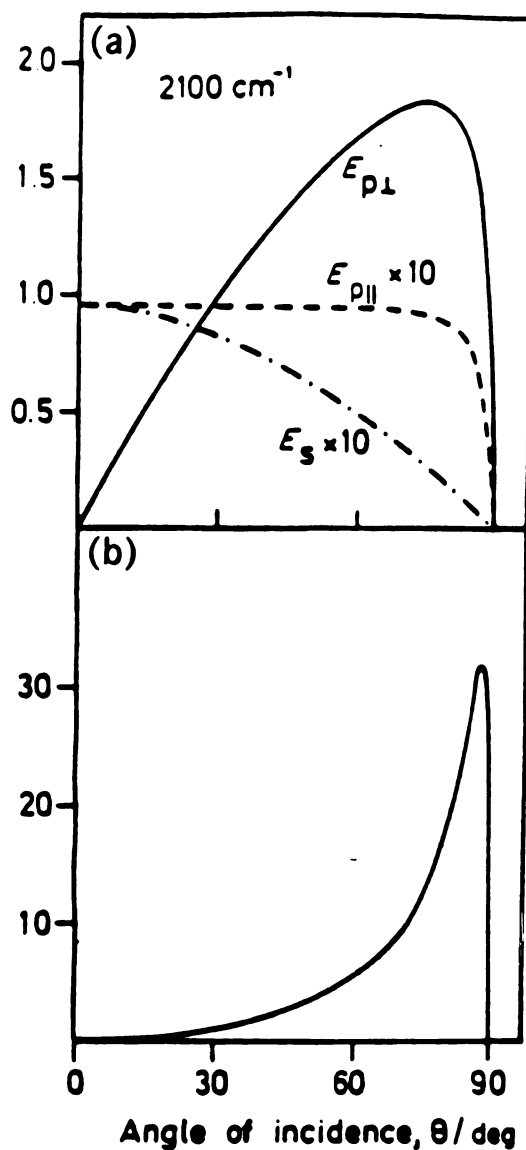


Figure 2-2. The surface electric field  $E/E_0$  in (a), and the quantity  $(E/E_0)^2/\cos \theta$  in (b) for platinum at  $2100 \text{ cm}^{-1}$  ( $\epsilon = -375 - 200i$ ) as a function of the angle of incidence,  $\theta$  (Bradshaw and Schweizer [1]).



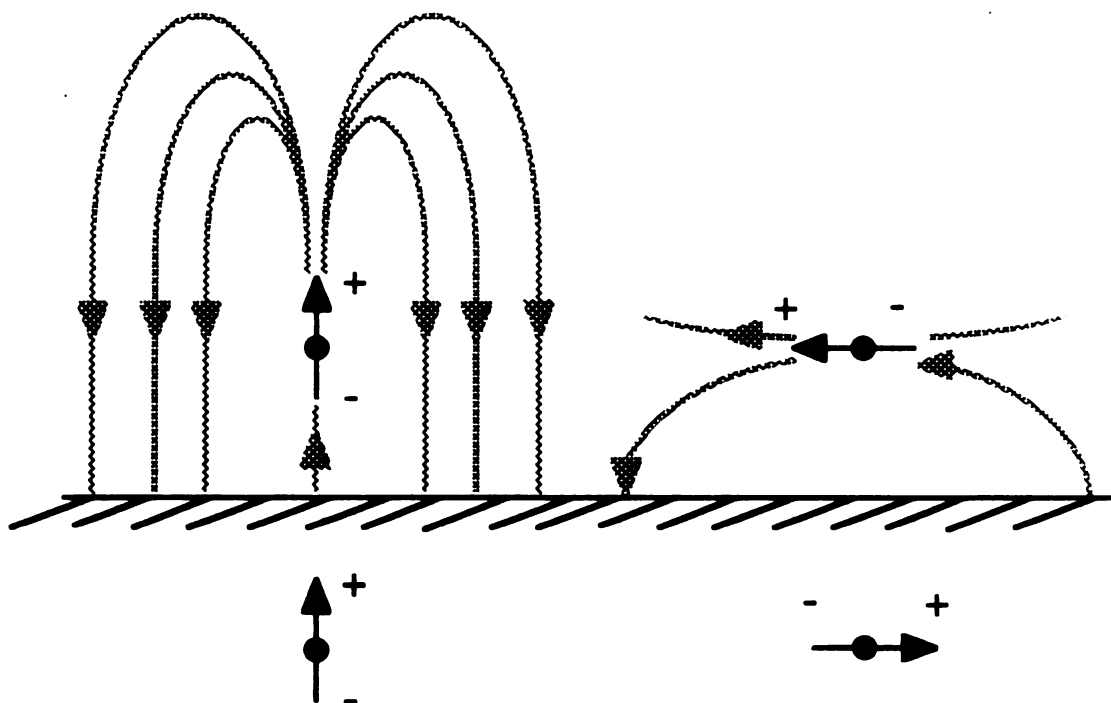
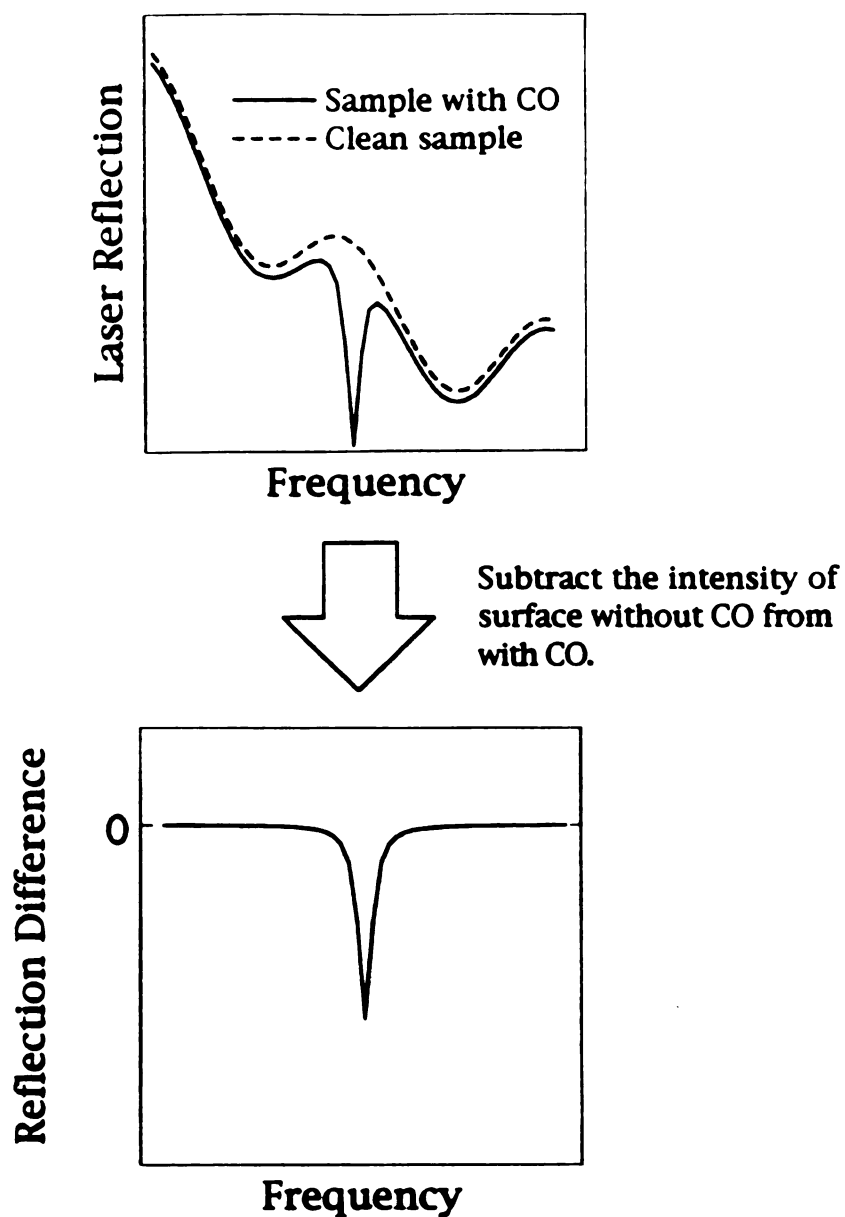


Figure 2-3. The image dipoles appearing on an adsorbed diatomic molecule oriented perpendicular and parallel to a metal surface.



**Figure 2-4.** Illustration of a process for obtaining RAIR spectrum from two scans of IR reflection measurements: scans with clean sample and with CO on the sample.

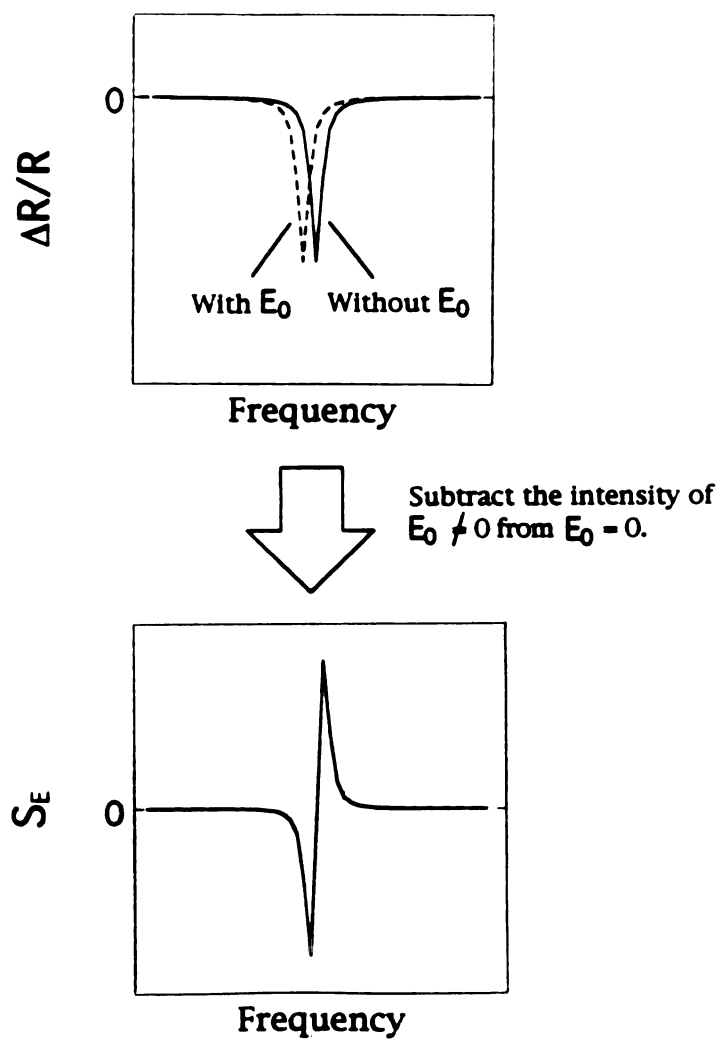


Figure 2-5. Illustration of a process for obtaining EVS spectrum by modulating the electrostatic field applied to the surface.

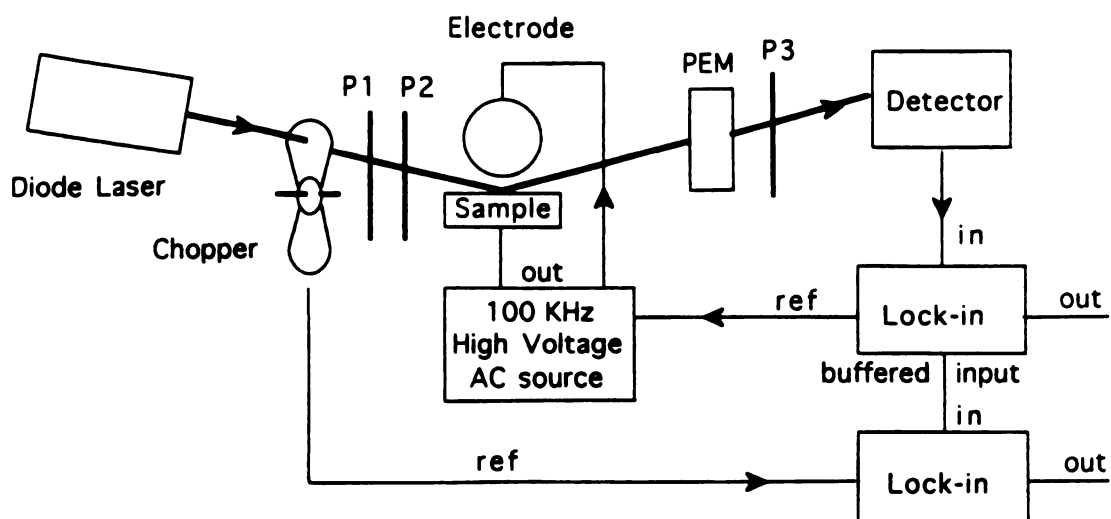


Figure 2-6. Schematic of the system used for electroreflectance vibrational infrared spectroscopy (EVS) (Lambert [21]).

**Figure 2-7. Optical system for RAIRS and EVS showing small mirror B (used as a beam splitter), detector D, electrode E, lens L, mirrors M, off-axis paraboloidal mirrors OAP, polarizers P, and sample S (Lambert [21]).**

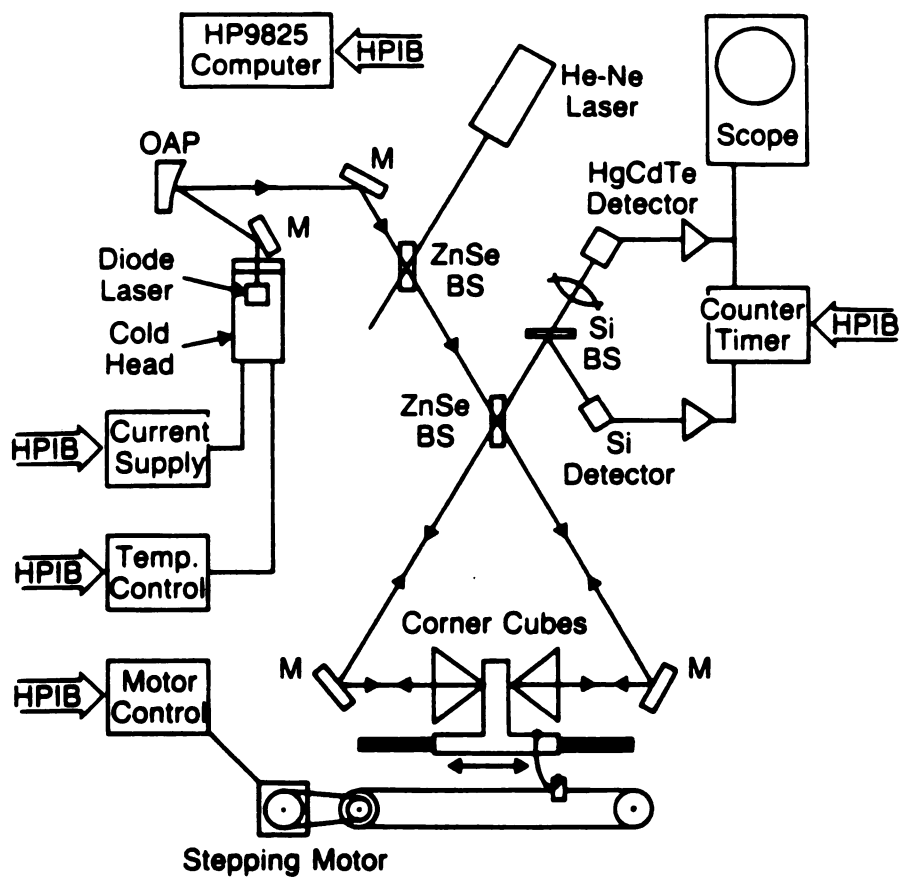


Figure 2-8. Schematic diagram of computer-controlled wavemeter. Back-to-back hollow corner cube reflectors are mounted on a ball slide translation stage driven by a stepping motor. The stage moves freely except near the end of its travel where a beaded chain coupling becomes rigid and reverses its motion. A small mirror BS is used like a beam splitter before the detectors. Light from the diode laser is collimated using a mirror M and off-axis paraboloid (OAP) (Lambert [29]).

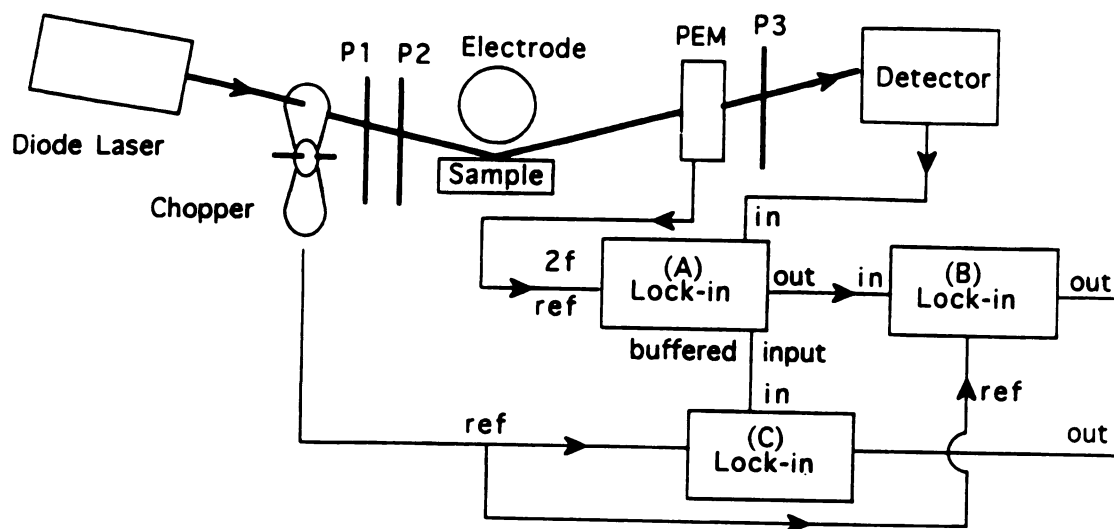


Figure 2-9. Schematic of the system used for polarization modulated reflection absorption infrared spectroscopy (RAIRS).

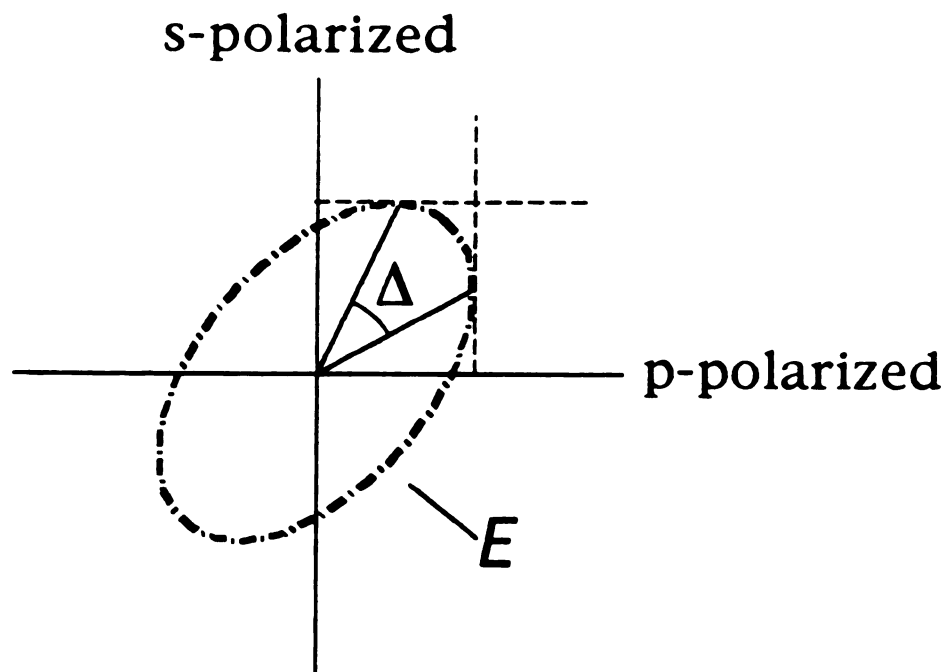


Figure 2-10. Optical E field with ellipsometric phase difference  $\Delta$  between s- and p-polarized light incident on the PEM.



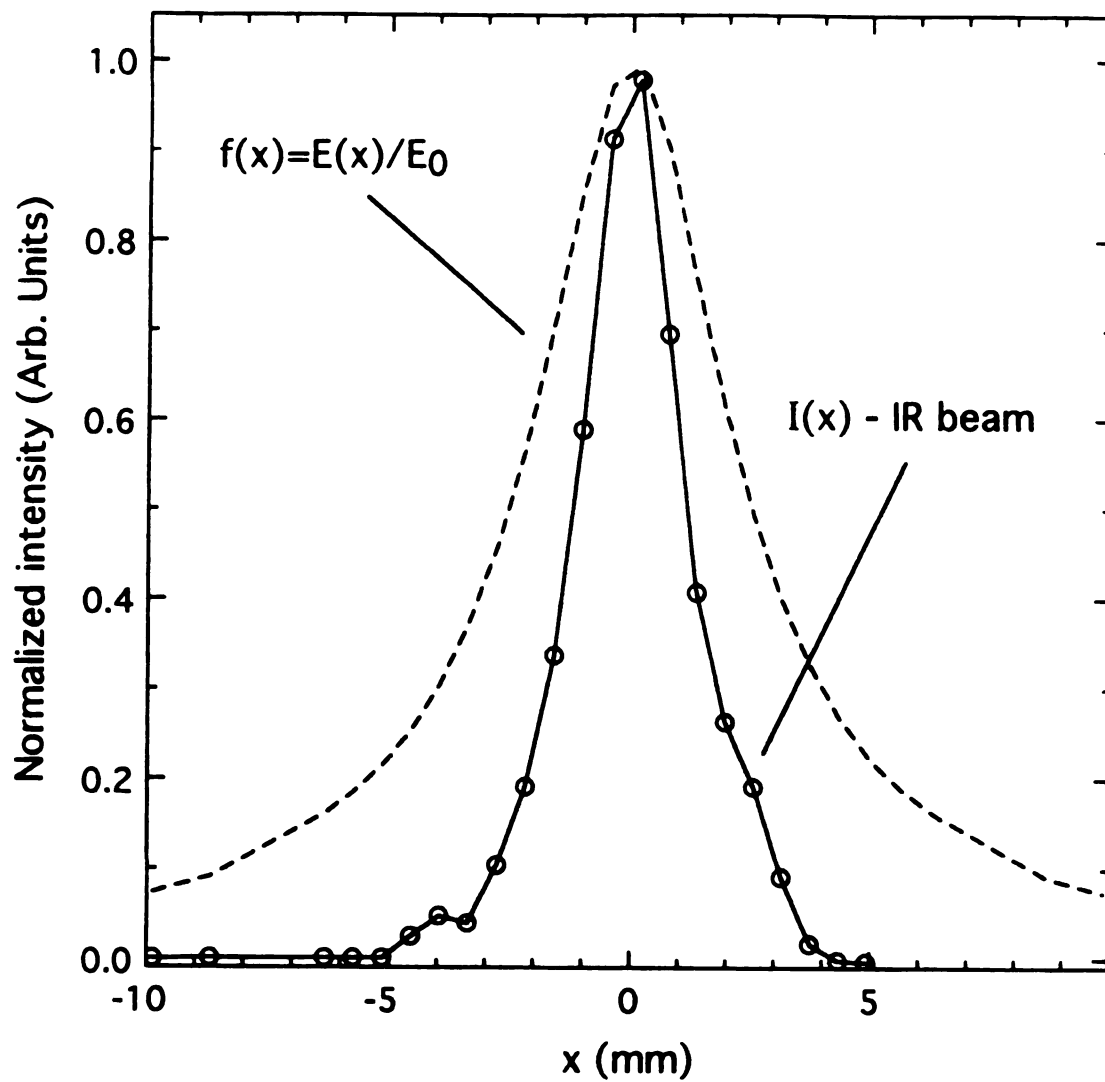


Figure 2-11. Normalized intensity vs horizontal displacement from the focal point on the sample surface.

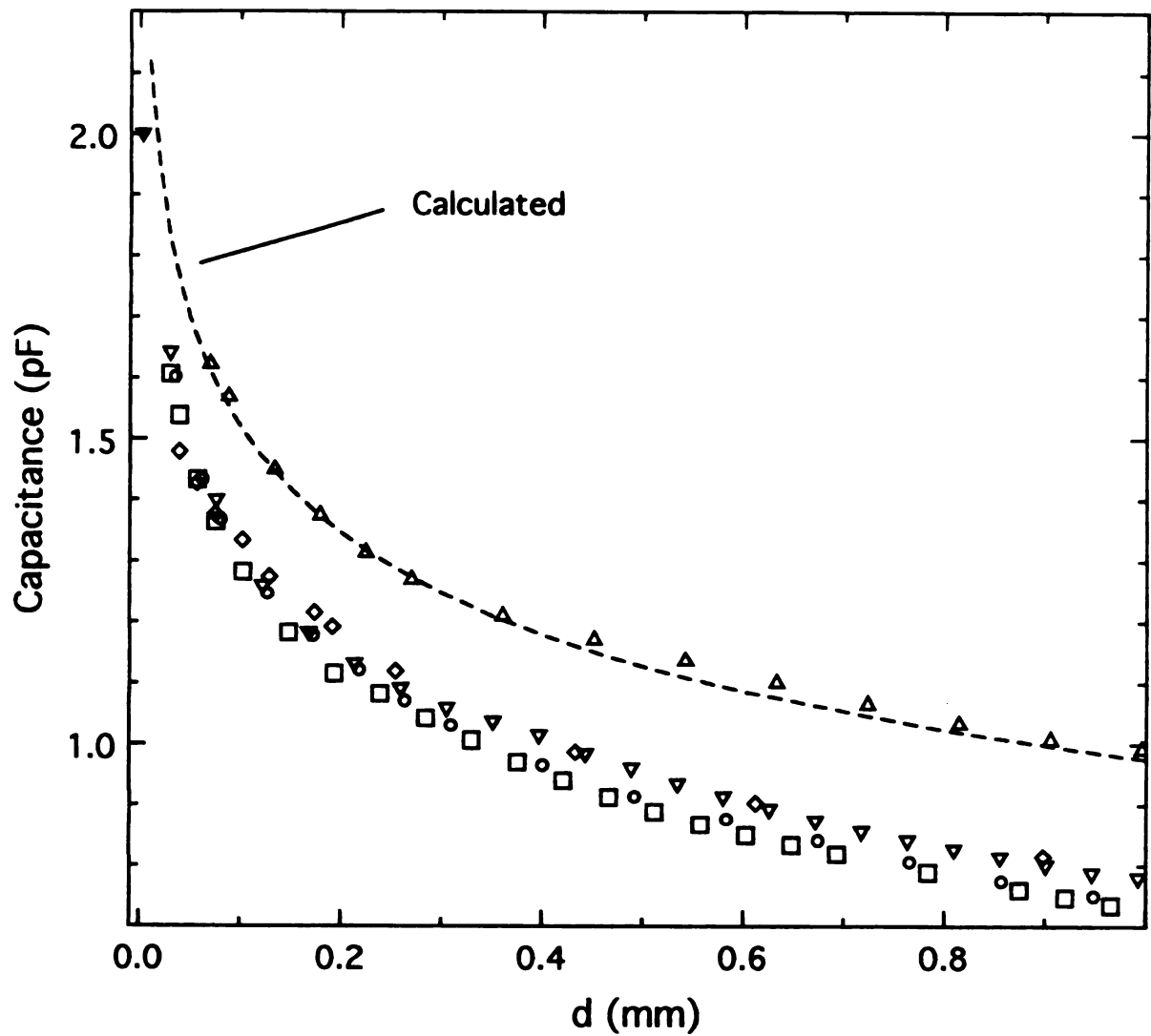


Figure 2-12. Measured and calculated capacitance between sample and spherical counter electrode vs. the gap  $d$  between them. Points are the measured data on five different days and curve is the calculated capacitance. Agreement between the measured and calculated capacitance is discussed in the text.

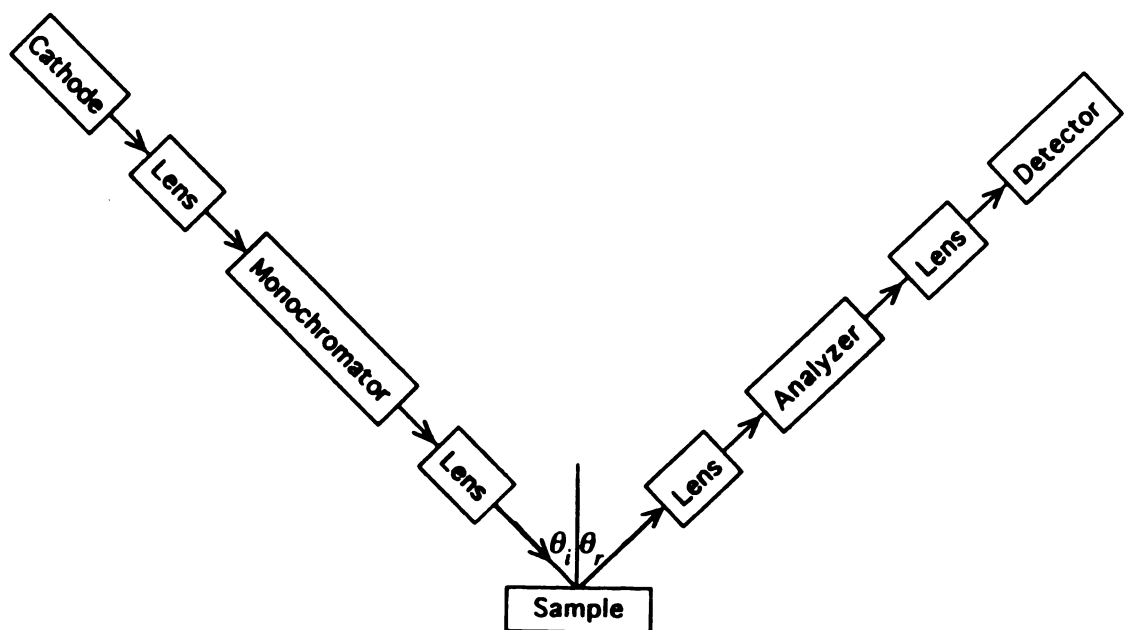


Figure 2-13. Block diagram of an electron energy loss spectrometer.

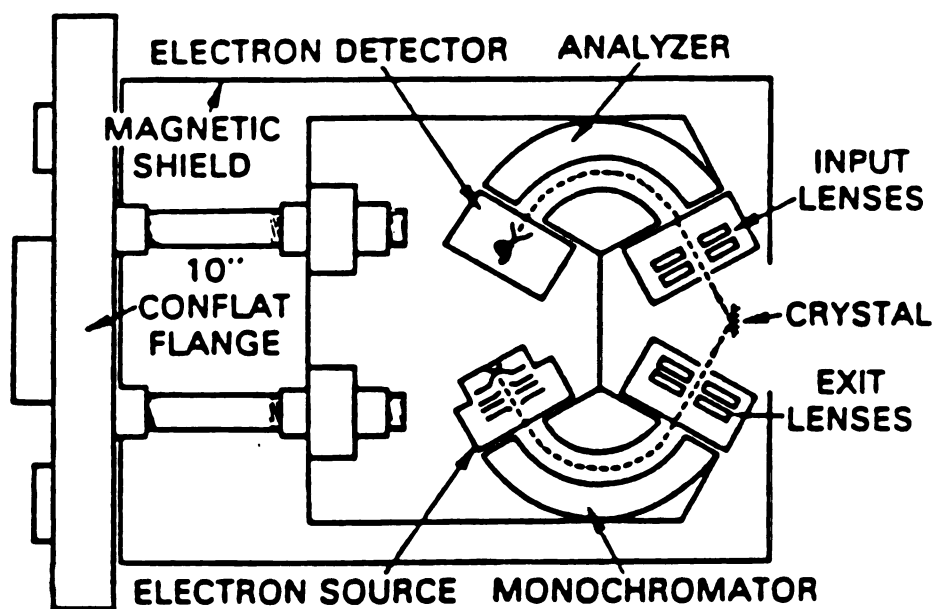


Figure 2-14. Schematic diagram of the system for electron energy loss spectroscopy (EELS) (Sexton [34]).

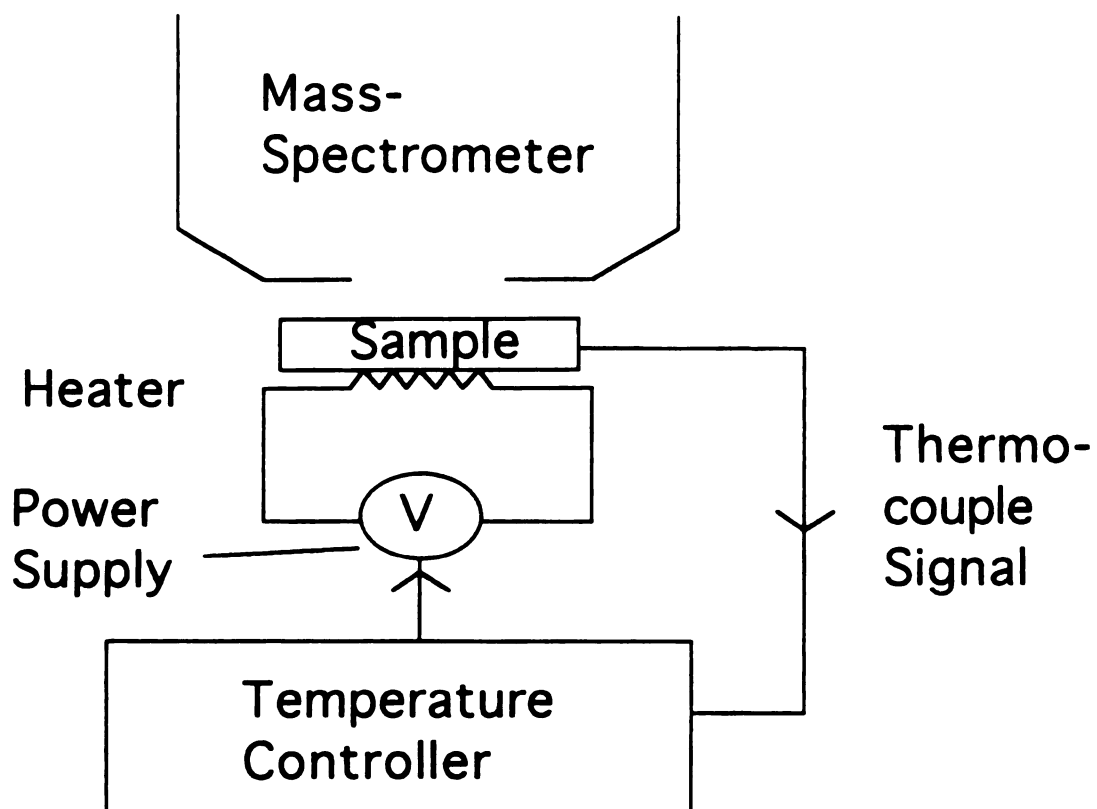


Figure 2-15. Schematic of the system for temperature programmed desorption (TPD).

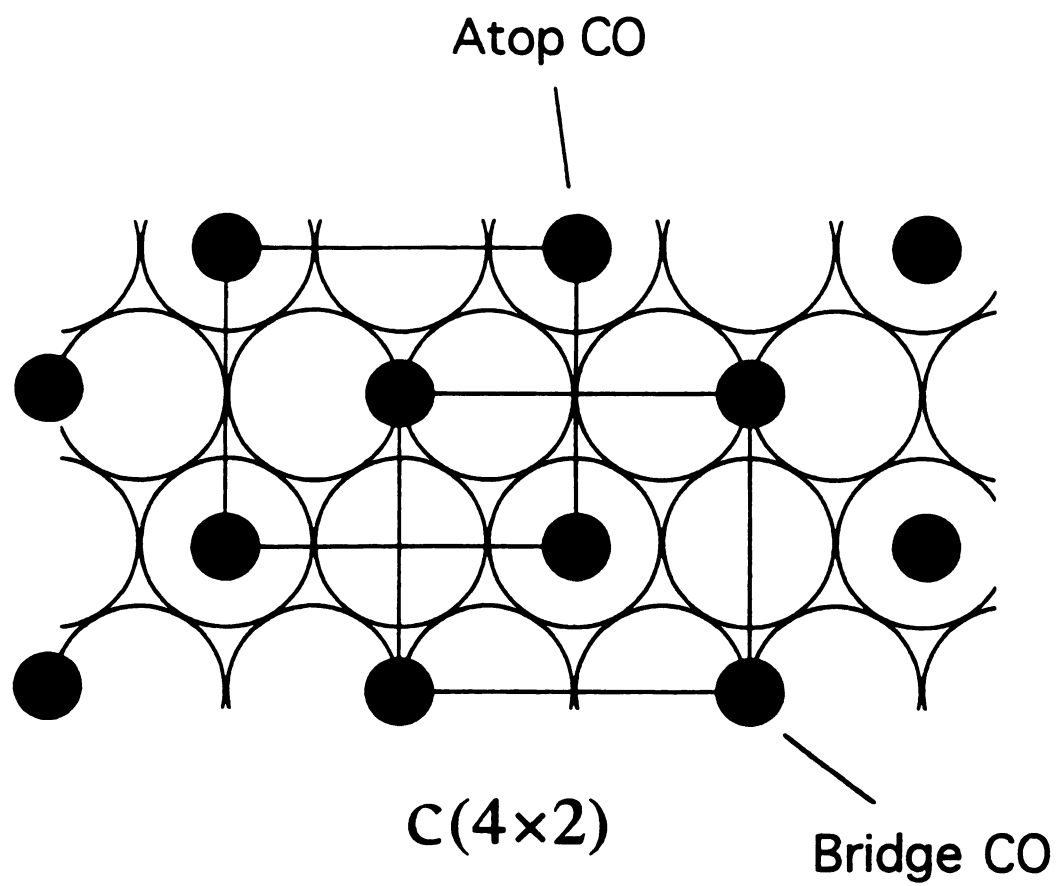


Figure 2-16. Geometrical  $c(4 \times 2)$  structure of CO on Pt(111).

## References

1. A.M. Bradshaw and E. Schweizer, in *Spectroscopy of Surfaces*, edited by R.J.H. Clark and R.E. Hester, (John Wiley & Sons, New York, 1988).
2. N.R. Avery, in *Vibrational Spectroscopy of Molecules on Surfaces*, edited by J.T. Yates, Jr. and T.E. Madey, (Plenum, New York, 1987).
3. M.A. Chesters and N. Sheppard, in *Spectroscopy of Surfaces*, edited by R.J.H. Clark and R.E. Hester, (John Wiley & Sons, New York, 1988).
4. J.W. Gadzuk, in *Vibrational Spectroscopy of Molecules on Surfaces*, edited by J.T. Yates, Jr. and T.E. Madey, (Plenum, New York, 1987).
5. B.E. Hayden, in *Vibrational Spectroscopy of Molecules on Surfaces*, edited by J.T. Yates, Jr. and T.E. Madey, (Plenum, New York, 1987).
6. P. Hollins and J. Pritchard, *Prog. Surf. Sci.* **19**, 275 (1985).
7. H. Ibach and D.L. Mills, *Electron Energy Loss Spectroscopy and Surface Vibrations*, (Academic, New York, 1982).
8. G. Kisters, J.G. Chen, S. Lehwald and H. Ibach, *Surf. Sci.* **245**, 65 (1991).
9. J.S. Luo, R.G. Tobin, D.K. Lambert, G.B. Fisher and C.L. DiMaggio, *Surf. Sci.* **274**, 53 (1992).
10. J.S. Luo, R.G. Tobin, D.K. Lambert, F.T. Wagner and T.E. Moylan, *J. Electron Spectrosc. Relat. Phenom.* **54/55**, 469 (1990).
11. R.G. Tobin, *Surf. Sci.* **183**, 226 (1987).
12. R.G. Tobin, R.B. Phelps and P.L. Richards, *Surf. Sci.* **183**, 427 (1987).
13. M. Tushaus, E. Schweizer, P. Hollins and A.M. Brashaw, *J. Electron Spectrosc. Relat. Phenom.* **44**, 305 (1987).
14. C.W. Olsen and R.I. Masel, *Surf. Sci.* **201**, 444 (1988).

15. J.E. Reutt-Robey, D.J. Doren, Y.J. Chabal and S.B. Christman, J. Chem. Phys. **93**, 9113 (1990).
16. D.K. Lambert and R.G. Tobin, Surf. Sci. **232**, 149 (1990).
17. B.E. Hayden, K. Kretzschmar, A.M. Bradshaw and R.G. Greenler, Surf. Sci. **149**, 394 (1985).
18. E. Schweizer, B.N.J. Persson, M. Tushaus, D. Hoge and A.M. Bradshaw, Surf. Sci. **213**, 49 (1989).
19. A. Ortega, F.M. Hoffmann and A.M. Bradshaw, Surf. Sci. **119**, 79 (1982).
20. B.N.J. Persson and R. Ryberg, Phys. Rev. B **24**, 6954 (1981).
21. D.K. Lambert, Appl. Opt. **27**, 3744 (1988).
22. D.K. Lambert, J. Chem. Phys. **89**, 3847 (1988).
23. D.K. Lambert, Solid State Commun. **51**, 297 (1984).
24. D.K. Lambert, Phys. Rev. Lett. **50**, 2106 (1983).
25. S.A. Francis and A.H. Ellison, J. Opt. Soc. Amer. **49**, 131 (1959).
26. R.G. Greenler, J. Chem. Phys. **44**, 310 (1966).
27. R.F. Willis, *Vibrational Spectroscopy of adsorbates*, (Springer-Verlag, Berlin, 1980).
28. P.J. Feibelman, Prog. Surf. Sci. **12**, 287 (1982).
29. D.K. Lambert, Appl. Opt. **25**, 2867 (1986).
30. D.K. Lambert, SPIE **438**, 158 (1983).
31. W.G. Golden, D.S. Dunn and J. Overend, J. Catalysis **71**, 395 (1981).
32. L.F. Sütcu, J.L. Wragg and H.W. White, Phys. Rev. B **41**, 8164 (1990).
33. D.K. Lambert, J. Chem. Phys. **94**, 6237 (1991).
34. B.A. Sexton, J. Vac. Sci. Technol **16**, 1033 (1979).



35. P.A. Redhead, *Vacuum* **12**, 203 (1962).
36. H. Steininger, S. Lehwald and H. Ibach, *Surf. Sci.* **123**, 264 (1982).
37. C.-M. Chan and W.H. Weinberg, *Appl. Surf. Sci.* **1**, 377 (1978).

## *CHAPTER 3*

### VIBRATIONAL STARK EFFECT AT SURFACES

#### I. Introduction

Two vibrational effects occur for an adsorbate when an electric field is applied to the surface. The first effect is a shift in the vibrational frequency and the second is a change in the vibrational intensity [1]. For CO on transition metals, the second effect is less significant than the first effect because the intensity change is too small to be observed in our EVS measurements. Theoretical calculations also indicate that the second effect is about 50 times smaller than the first effect for CO on Pt(111) (see section II-4 in Chapter 2 [2,3]). Therefore, we will discuss only the first effect, the Stark shift, here.

There are several theoretical approaches currently available in studying the Stark shift [1,3,4,5]. A phenomenological approach [3] obtains essentially the same first order result as more elaborate semiclassical or *ab initio* calculations. Since the applied electrostatic field is estimated to be at least 100 times smaller than the surface electric field provided by surface electrons, first order is sufficient to explain the observed data. Here, we will review the simplest phenomenological calculation by Lambert [3]. The phenomenological theory is also used to analyze the data of CO on Pt(335) by Lambert and Tobin [6].

#### II. Stark Tuning Rate Theory

The Stark tuning rate of an adsorbed molecule can be theoretically obtained given the Hamiltonian [3]

$$\begin{aligned}
H &= P^2/2\mu - \mathbf{M} \cdot \mathbf{E}_0(0) + 1/2 \int \tilde{\rho}(\mathbf{r}) \tilde{\phi}(\mathbf{r}) dV \\
&= P^2/2\mu + V(Q),
\end{aligned} \tag{1}$$

$$\text{where } V(Q) = a_{00} + a_{20}Q^2 + a_{30}Q^3 + \dots$$

In Equation (1), we define  $Q$  as a generalized coordinate corresponding to oscillation of a normal mode and  $P$  as the corresponding generalized momentum with effective mass  $\mu$ . Also,  $V(Q)$  is the generalized intramolecular potential of an adsorbate; this will be explained in more detail below. The charge distribution  $\rho$  and electrostatic potential distribution  $\phi$  at the surface can be described in two situations: without an adsorbed molecule  $[\rho_0(\mathbf{r}), \phi_0(\mathbf{r})]$  and with an adsorbed molecule  $[\rho_0(\mathbf{r}) + \tilde{\rho}(\mathbf{r}), \phi_0(\mathbf{r}) + \tilde{\phi}(\mathbf{r})]$ . In Equation (1),  $\mathbf{E}_0$  is provided by substrate atoms, so  $\mathbf{E}_0 = -\nabla\phi_0$ .  $\mathbf{M}$  is the dipole moment of the adsorbate obtained from expansion of  $\tilde{\rho}(\mathbf{r})$ . Essentially, the first term of potential energy in Equation (1) is related to interaction between the adsorbed molecule and the surface atoms and the second term is associated with self energy of the adsorbate.

When an external electric field  $\mathbf{E}_{\text{applied}}$  is applied, the Hamiltonian will change. The external field will also change the generalized adsorbate dipole moment  $\mathbf{M}(Q)$  and  $V(Q)$ . Such a change will result in a change in the electronic wavefunctions of the adsorbate for a fixed nuclear position. Since we applied a very small electric field,  $\mathbf{E}_{\text{applied}} \ll \mathbf{E}_0$ , field-induced change in  $\mathbf{M}(Q)$  and  $V(Q)$  are ignored to good approximation. If we assume that the applied field is parallel to the dipole moment of adsorbate, and we define the local field  $E_{\text{local}}$  is the total electric field (the applied field plus induced fields due to the applied field) that acts upon the individual adsorbate treated as polarizable point, the Hamiltonian becomes:

$$H = P^2/2\mu + V(Q) - M(Q) \cdot E_{\text{local}}, \tag{2}$$

with  $E_{local} = \gamma_{DC} E_{applied}$ .

Here,  $\gamma_{DC}$  is a screening factor of the electrostatic field, as is discussed in more detail in Chapter 6. Also, the dipole moment in general coordinates can be expressed as

$$M(Q) = -(a_{01} + a_{11}Q + a_{21}Q^2 + \dots) \quad (3)$$

From Equation (2), with application of Equations (1) and (3), we can calculate the frequency with applied electric field to the first order of perturbation. The Hamiltonian with two perturbed terms due to the local field can be written as

$$H = H_0 + (a_{11}E_{local})Q + (a_{21}E_{local})Q^2, \quad (4)$$

$$\text{with } H_0 = P^2/2\mu + a_{20}Q^2 + a_{30}Q^3.$$

Note that  $H_0$  is the Hamiltonian without being perturbed by the electric field but with the small anharmonic term  $a_{30}$ . By solving  $H_0$ , we obtain the following eigenfunction at the  $n$ th energy level [7]

$$\begin{aligned} |\tilde{n}\rangle = & |n\rangle - 3\sigma\sqrt{\frac{(n+1)^3}{8}}|n+1\rangle + 3\sigma\sqrt{\frac{n^3}{8}}|n+1\rangle \\ & - \frac{\sigma}{3}\sqrt{\frac{(n+3)(n+2)(n+1)}{2}}|n+3\rangle + \frac{\sigma}{3}\sqrt{\frac{n(n-1)(n-2)}{2}}|n-3\rangle \\ & + \dots \end{aligned} \quad (5)$$

$$\text{with } \sigma = \frac{a_{30}}{4\pi^2c^2\mu\nu_0^2}\sqrt{\frac{\hbar}{2\pi c\mu\nu_0}}.$$

where  $|n\rangle$  is the eigenfunction of a harmonic oscillator and  $\nu_0 = \sqrt{a_{20}/2\pi^2c^2\mu}$  is the harmonic oscillator vibrational frequency. The first-order perturbation energy at the  $n$ th energy level can be obtained by calculating  $\Delta E_n^{(1)} = \langle \tilde{n} | a_{11}Q + a_{21}Q^2 | \tilde{n} \rangle$ . The required calculations are as follows:

$$\langle \tilde{n} | Q | \tilde{n} \rangle = -3\sqrt{2} \sigma (\sqrt{(n+1)^4/8} - \sqrt{n^4/8}) \times \sqrt{\frac{\hbar}{2\pi c \mu \nu_0}} \quad (6)$$

$$\langle \tilde{n} | Q^2 | \tilde{n} \rangle \approx (n + 1/2) \times \sqrt{\frac{\hbar}{2\pi c \mu \nu_0}} \quad (7)$$

Here, the terms that contain  $(a_{30})^2$  in Equation (7) are neglected.

Applying Equations (6) and (7), we obtain the final energy for the Hamiltonian  $H$ . The final vibrational frequency with applied field can be calculated as:

$$\nu = (E_1 - E_0)/(hc) \approx \nu_0 + (\Delta E_1^{(1)} - \Delta E_0^{(1)})/(hc). \quad (8)$$

Here,  $E_1$  and  $E_0$  are the final energies for the first excited state and the ground state, respectively. Combining Equations (6), (7), and (8) we obtain the final vibrational frequency

$$\nu \approx \nu_0 + \frac{1}{4\pi^2 c^2 \mu \nu_0} (a_{21} - \frac{3a_{11}a_{30}}{4\pi^2 c^2 \mu \nu_0^2}) \times E_{local}. \quad (9)$$

The second term in Equation (9) is the frequency shift due to the applied field; only the linear electric effect is considered sufficient enough for a small field. The local field Stark tuning rate  $(d\nu/dE_{local})$  can be easily obtained by differentiating Equation (9) with respect to  $E_{local}$ :

$$d\nu/dE_{local} \approx \frac{a_{11}}{4\pi c \sqrt{2\mu} a_{20}} \left( \frac{2a_{21}}{a_{11}} - \frac{3a_{30}}{a_{20}} \right). \quad (10)$$

Here, the units for Equation (10) are " $\text{cm}^{-1}/(\text{V}/\text{cm})$ ",  $a_{20}$  is related to the vibrational frequency,  $a_{11}$  is related to the unscreened dynamic dipole moment,  $a_{30}$  is the cubic anharmonicity of the potential and is also related to the dissociation energy of CO, and  $a_{21}$  is the quadratic term in the dipole moment expansion. The curvature of the potential  $a_{20}$  and the linear dynamic dipole moment  $a_{11}$  can be determined from the measurements of RAIRS. The

cubic anharmonicity  $a_{30}$  is estimated by an indirect method described in Chapter 4. The quadratic  $a_{21}$  can be estimated from the overtone intensity in the EEL spectrum. For CO on Ni(100) [1], the first term is negligible compared to the second term in Equation (10), and the value of the Stark tuning rate estimated by using the parameters shows good agreement with the measured value.

Experimentally, we can measure only the external field Stark tuning rate,  $dv/dE_{\text{applied}}$ , directly. The relationship between the external and local field Stark tuning rate is as follows:

$$(dv/dE_{\text{applied}}) = \frac{dv}{d(E_{\text{local}}/\gamma_{DC})} = \gamma_{DC}(dv/dE_{\text{local}}), \quad (11)$$

where  $E_{\text{local}} = \gamma_{DC}E_{\text{applied}}$  is defined earlier in Equation (2). Derivation of  $\gamma_{DC}$  is referred to in Chapter 6. The external applied field  $E_{\text{applied}}$  polarizes the neighboring adsorbed molecules which are treated as polarizable points; the induced dipole moments of the polarized adsorbates produce an electric field that cancels part of the applied field. The final field is the local field  $E_{\text{local}}$  reduced by a factor of  $\gamma_{DC}$ ; therefore the EVS signal is related to the Stark tuning rate.

### III. Earlier Results of CO on Pt(335)

The major motivation for this work comes from an interesting result observed by Lambert and Tobin [6]. They studied CO on Pt(335) using polarization modulated RARS, and EVS, as discussed in Chapter 2. The Pt(335) surface is stepped, with (111) terraces four atoms wide and (100) steps one atom high as shown in Figure 1-1 of Chapter 1. The spectra cover the 2000-2160  $\text{cm}^{-1}$  range, so Lambert and Tobin measured only atop CO in this study. Some other

studies of the same or similar systems [8,9,10,11,12] indicate that, at low coverage, CO adsorbs only on the step edges, which are characterized by a vibrational frequency in the 2057-2080  $\text{cm}^{-1}$  range as shown in Figure 3-1 and a desorption temperature of 500-600 K as shown in Figure 5-2 of Chapter 5. When nearly all the edge sites are filled, CO begins to occupy terrace sites. Terrace CO has a vibrational frequency in the 2085-2100  $\text{cm}^{-1}$  range as shown in Figure 3-1, and desorbs in the 350-450 K range as shown in Figure 5-2 of Chapter 5; in this respect, terrace CO is very similar to CO on Pt(111).

Results of CO on Pt(335) obtained by Lambert and Tobin [6] are basically consistent with the other studies [8,9,10,11,12]. At low coverage, they observed only a single mode at 2066  $\text{cm}^{-1}$  as shown in Figure 3-1. At this coverage, TPD shows only the high-temperature peak. This spectral feature is therefore assigned to CO adsorbed on the step edges (edge CO). The low-coverage mode shifts to higher frequency as the coverage increases, and a second mode appears at 2088  $\text{cm}^{-1}$  as CO begins to occupy the terrace sites. As the coverage increases further, the high-frequency mode shifts to higher frequency and increases in intensity while the intensity of the low-frequency mode diminishes. The high-temperature peak in the TPD spectrum does not shrink at high coverage, however, so it is difficult to explain the loss of intensity from the low-frequency mode by an actual shift of molecules between sites.

Dipole-dipole coupling between the two species may explain the observed loss of intensity [6]. Such a coupling results in intensity borrowing; intensity of the low-frequency mode is transferred into intensity of the high-frequency mode due to the coupling effect. The smaller the difference in frequency between the two modes, the stronger the dipole coupling. For CO on Pt(355), edge CO and terrace CO are separated by no more than 40  $\text{cm}^{-1}$  [6,11], so the dipole coupling is expected to be quite significant. When edge sites are

nearly filled and increasing amounts of CO occupy the terrace sites, the intensity borrowing effect (coupling) increases with increasing CO coverage. The intensity of low-frequency mode (edge CO) gradually diminishes while the intensity of the high-frequency mode (terrace CO) is gradually enhanced with increasing CO coverage. Eventually, only one mode is observed at saturation in RAIRS.

Turning to the EVS spectra as shown in Figure 3-2, it is obvious that terrace CO shows no appreciable Stark effect; there is no derivative-like feature at the expected frequency. Instead of a zero crossing there is a small peak that mirrors the peak in the RAIR spectrum. Such an effect is not caused by the fact that the electric field changes the amount of adsorbate. An explanation for the observed peak that does not involve population change is discussed below.

At low coverage, only one mode is observed, so the analysis for determining the Stark tuning rate is relatively straightforward and has been described in section II-4 of Chapter 2. The EVS signal  $S_E$  and the RAIRS spectrum  $\Delta R/R$  are related by the following equations:

$$(S_E)_e = (dv/dE)_e \langle E \rangle_e \frac{d(\Delta R/R)_e}{dv} \quad (12)$$

$$(S_E)_t = (dv/dE)_t \langle E \rangle_t \frac{d(\Delta R/R)_t}{dv} \quad (13)$$

Here, subscripts e and t refer to edge and atop CO, respectively;  $(dv/dE)$  is the local field Stark tuning rate;  $\langle E \rangle$  is the local rms field applied to the adsorbate. Note that subscript "local" is dropped to simplify the notation. Only edge CO is observed at low coverage. The local field Stark tuning rate of edge CO can be determined directly from Equation (12) with a combination of RAIRS and EVS measurements and an estimate of the local field  $\langle E \rangle$ . Lambert and Tobin [6]



determined  $\langle E \rangle$  from the measured value of the applied external field  $\langle E_{\text{applied}} \rangle$  and an estimate of  $\gamma_{DC}$  for edge CO. Their method for estimating  $\gamma_{DC}$  is discussed below.

In Lambert and Tobin's analysis, the screening factor  $\gamma_{DC}$  was indirectly estimated by assuming  $\gamma_{DC} = \gamma_R$ , where  $\gamma_R$  is the screening factor of the IR field adsorption. It is believed that  $\gamma_R$  originates from the same dipole screening mechanism as  $\gamma_{DC}$  described earlier, so both  $\gamma_R$  and  $\gamma_{DC}$  are coverage dependent and  $\gamma_{DC} = \gamma_R = 1$  at near zero coverage. One can measure the screened dynamic dipole moment  $\gamma_R a_{11}$  of CO from the RAIRS absorption intensity. At near zero coverage,  $a_{11}$  is obtained directly. Lambert and Tobin estimated  $\gamma_R$  for edge CO by comparing  $a_{11}$  obtained from RAIRS of CO on Pt(111) with  $\gamma_R a_{11}$  obtained from RAIRS of CO on Pt(335) at low coverage.  $\gamma_{DC}$  is thus determined with the assumption  $\gamma_{DC} = \gamma_R$ . A more detailed discussion of both  $\gamma_R$  and  $\gamma_{DC}$  can be found in Chapter 6. With  $\gamma_{DC}$  determined, Equation (12) gives  $(d\sqrt{dE})_e = (8.3 \pm 1.5) \times 10^{-7} \text{ cm}^{-1}/(\text{V}/\text{cm})$ .

A phenomenological model was used to analyze the data of CO on Pt(335) at higher coverage where CO starts to occupy the terrace sites. Because the two CO species strongly interact with each other on Pt(335) at higher coverage, the analysis necessary to obtain the Stark tuning rates of the two CO species becomes very complicated. Their model includes the dipole coupling mechanism between the edge and terrace CO; edge and terrace CO are treated as coupled oscillators. In the model, only atop CO species are considered, and screening factors  $\gamma_{DC}$  and  $\gamma_R$  are assumed to be the same at the two sites. Essentially, they assumed that  $(\gamma_{DC})_e = (\gamma_{DC})_t = (\gamma_R)_e = (\gamma_R)_t$ . Therefore  $\langle E \rangle_e = \langle E \rangle_t$  are assumed in their analysis.

For edge CO, the coupled-oscillator model gives  $(dv/dE)_e = (7.5 \pm 2.0) \times 10^{-7} \text{ cm}^{-1}/(\text{V}/\text{cm})$  at all coverage; this is essentially consistent with the measurement at low coverage with only edge CO species. In contrast, the local field Stark tuning rate of terrace CO  $(dv/dE)_t$  is at least an order of magnitude smaller. The model suggests that  $(dv/dE)_t \leq 8.0 \times 10^{-8} \text{ cm}^{-1}/(\text{V}/\text{cm})$ .

A model fit to the experimental data at 87% saturation coverage is used to illustrate the physical picture provided by the model. When the electrostatic field is applied to the surface, the electric field shifts the vibrational frequency of edge CO but barely shifts the vibrational frequency of terrace CO. This results in increasing the difference in frequency between the two species and in reducing the intensity borrowing effect that transfers the intensity of edge CO into that of terrace CO as shown in Figure 3-3. Thus, we obtain the EVS signal by subtracting the RAIR spectrum without E field from that with E field as shown in Figure 3-3. Although some deviation between the simple model fit and experimental data is clearly shown in Figure 3-4, the model generally provides good approximation for a quantitative analysis. Also, the major conclusion by Lambert and Tobin that there is a significant difference between the Stark tuning rate of edge and of terrace CO is not sensitive to the model; this is discussed in detail below.

It is conclusive that the EVS signals at the two sites are distinctively different:  $(S_E)_e \gg (S_E)_t$ . Both Lambert and Tobin [6] and Reutt-Robey et al. [12,13] found that the IR cross section,  $\propto \Delta R/R$ , for terrace CO is similar to that for edge CO. From Equations (12) and (13), the difference in EVS signal is related to the quantities of  $(dv/dE)$  and  $\langle E \rangle$  at the two sites.

Assuming, as Lambert and Tobin did, that the screening factor of the electrostatic field is the same at the two sites, then local fields at the two sites

must be the same:  $\langle E \rangle_t = \langle E \rangle_e$ . The local field Stark tuning rate between terrace CO and edge CO then has to be intrinsically different:  $(dv/dE)_t < (dv/dE)_e$ . Consequently, intramolecular structure related to parameters,  $a_{11}, a_{21}, a_{20}$ , and  $a_{30}$  must be responsible for the difference between the Stark tuning rates at the two sites; a chemical mechanism was essentially applied to account for the observed data. A detail discussion of our investigation related to intramolecular structures of CO on Pt(335) using EELS is presented in Chapter 4. Our data indicates that the intramolecular structures of CO are, however, unlikely to be very different at the two sites.

This implies that the local field Stark tuning rates at the two sites are essentially similar:  $(dv/dE)_t \approx (dv/dE)_e$ . The difference in EVS signals is the result of a significantly smaller local field applied to the terrace sites than to the edge sites. This means that the screening factor of the electrostatic field for terrace CO is much smaller than that for edge CO:  $\langle E \rangle_t < \langle E \rangle_e$ . Since the IR cross sections of the two species are similar, screening factors of the IR field also are similar at the two sites. This line of reasoning indicates that  $(\gamma_{DC})_t < (\gamma_{DC})_e$  while  $(\gamma_R)_t \approx (\gamma_R)_e$ . Such a physical explanation results in a rather surprising outcome:  $\gamma_{DC} \approx \gamma_R$ . A direct comparison between the two screening factors can be found in Chapter 6, which presents measurements of the static screening and the IR screening as function of CO coverage on flat Pt(111) surface. Our data of CO on Pt(111) indicate that, even on the flat (111) surface,  $\gamma_{DC} \approx \gamma_R$ . The physical mechanism suggests that the external field Stark tuning rate,  $(dv/dE_{\text{applied}}) = \gamma_{DC}(dv/dE)$ , for terrace CO is significantly smaller than that for edge CO while the local field Stark tuning rates for both CO species are the same.

The deviation between the experimental data and the coupled-oscillator model has several possible explanations. Two of the most important are that

(1), the model considers only two atop CO species, excluding two other CO species, edge bridge and terrace bridge CO, on Pt(335) that should be included in the model; and (2), characterization of total CO coverage is incorrect in the analysis. I discovered that, when the Pt(111) sample is close to the electrode (with a gap about 0.4 mm), CO coverage where the sample is right underneath the electrode is actually much less than where it is away from the electrode. Annealing the sample at 260 K does not improve the homogeneity of the CO layer. For CO on Pt(111), IR spectra can also be used to calibrate the CO coverage; more details can be found in Chapter 6. The IR spectral data indicate less CO coverage than the TPD data when the sample stays close to the electrode during CO dosage. Essentially, TPD provides average coverage information over the surface while IR spectra provides local coverage information under the electrode; the size of the IR beam spot on the surface is about 0.5 mm  $\times$  5 mm. Also, TPD and IR spectra give consistent coverage results for CO on Pt(111) when the sample is moved away from the electrode during dosage. Therefore, we conclude that the coverage under the electrode was much lower. Such a shadow effect, however, does not affect the calibration of saturation coverage. While the model used by Lambert and Tobin is quit crude, their major conclusion about the Stark tuning rates of the two CO species stands.

To summarize, a simple phenomenological theory in dealing with the vibrational Stark effect is reviewed. The theory was used to analyze the observed data of CO on Pt(335) that leads to an important conclusion: the Stark tuning rate observed by Lambert and Tobin can be possibly affected by either physical or chemical effects. The cause of the surprising difference between the Stark tuning rate of edge and terrace CO on Pt(335) is the major motivation for my Ph.D. thesis work. Mainly, the physical effects relate to different

screening of the electrostatic fields and the chemical effects involve induced changes in intramolecular structures due to site difference on Pt(335). Our experimental measurements, presented in Chapters 4, 5 and 6, show that screening, and not chemical effects, is responsible for these observed differences.

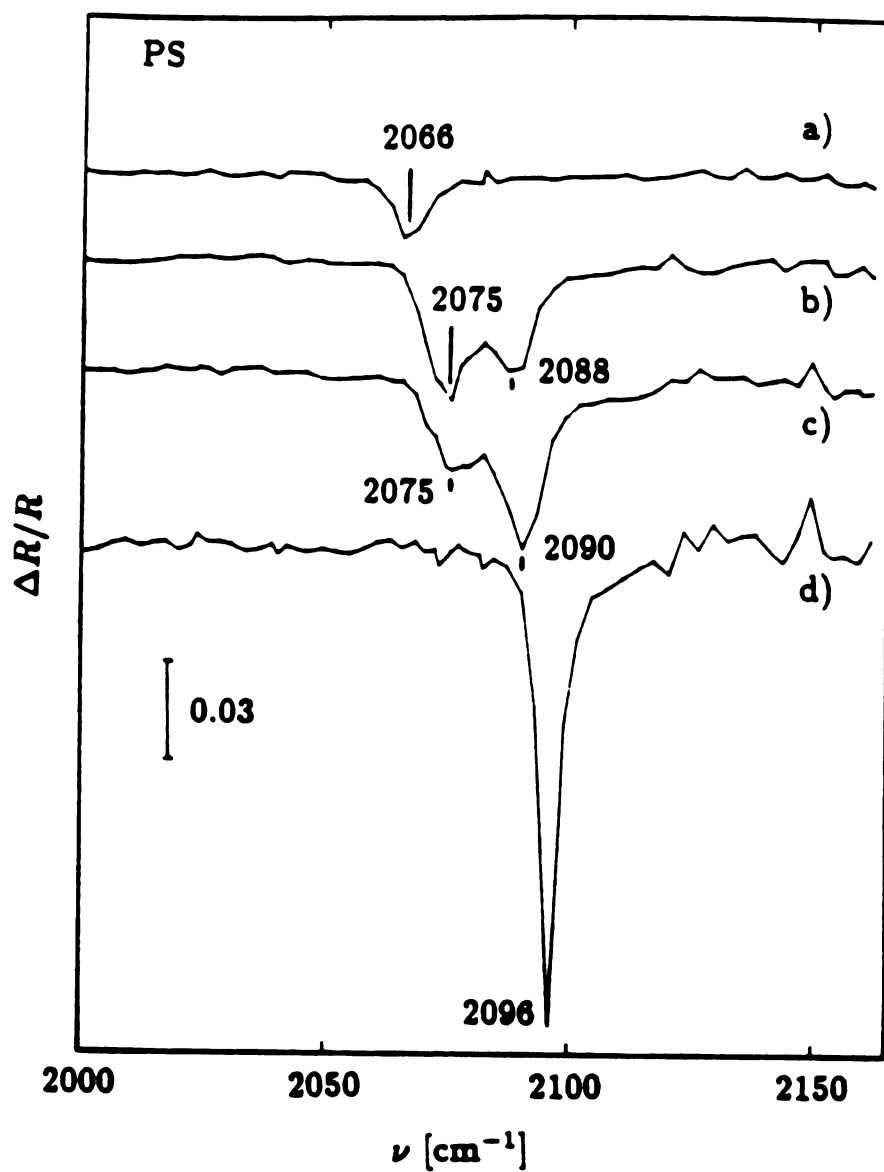


Figure 3-1. Polarization modulated RAIR spectra (PS is used instead in ref. [6] as shown) of CO on Pt(335) at 300 K obtained by Lambert and Tobin [6]. The CO coverages were 0.06, 0.5, 0.54, and 0.63 ML for spectra a - d, respectively; the determination of coverages is, however, partially incorrect as indicated in the text.

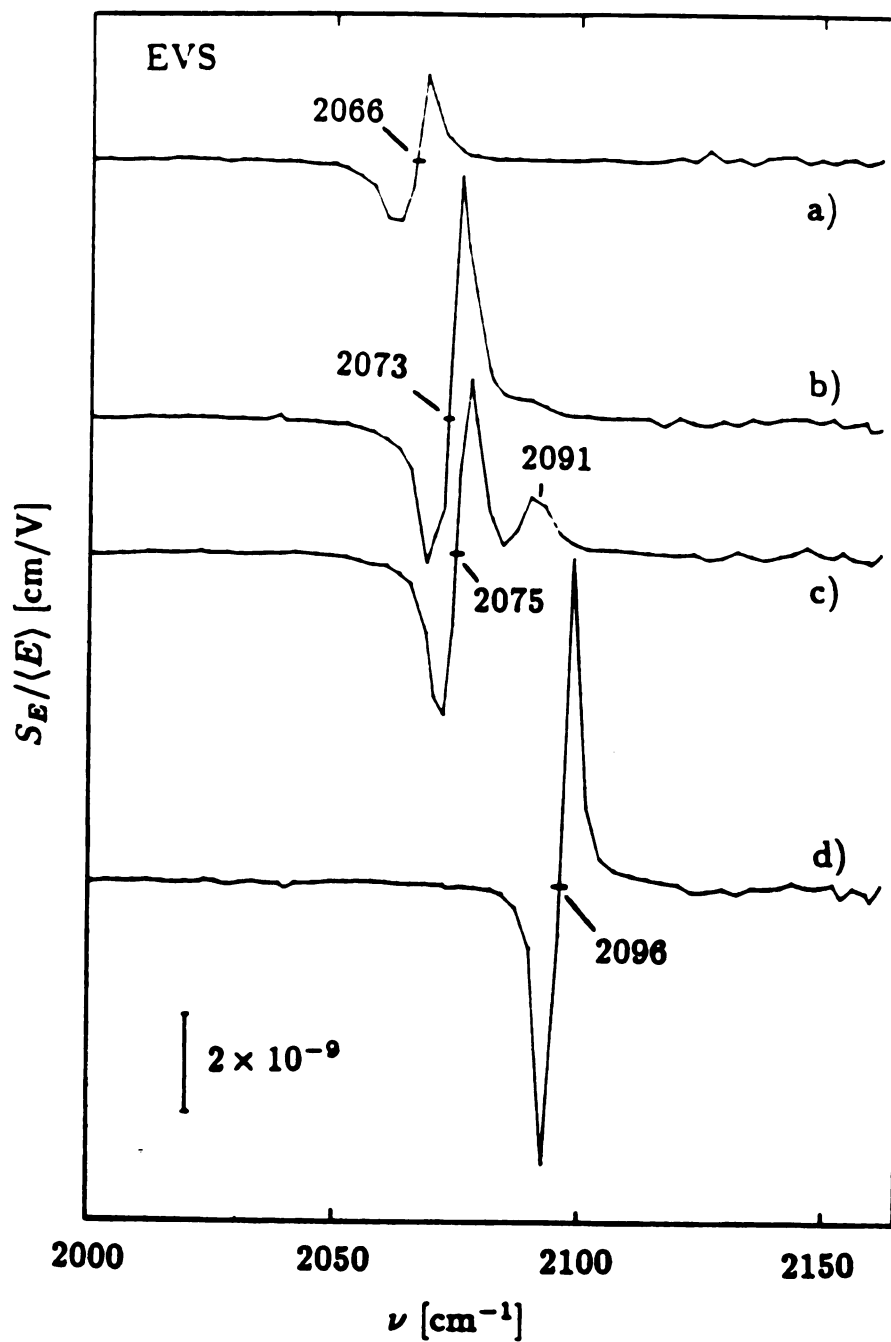
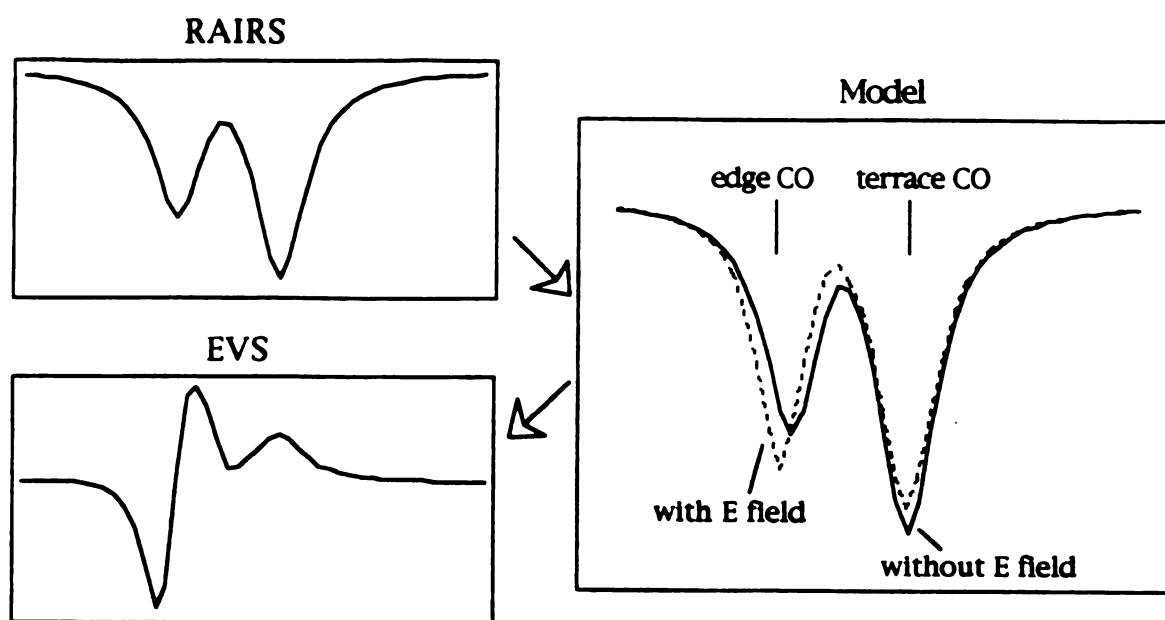


Figure 3-2. EVS spectra of CO on Pt(335) at 300 K obtained by Lambert and Tobin [6]. Spectra a - d correspond directly to spectra a - d in Figure 3-1.



**Figure 3-3. Illustration of model's dipole-dipole coupling and Stark effect of CO on Pt(335). In the model, the electrostatic field shifts the vibrational frequency for edge CO but not for terrace CO. The Stark effect that increases the difference in frequency between the two CO species results in reduced dipole-dipole coupling. Such coupling transfers absorption intensity from edge into terrace CO mode. The EVS spectrum is then obtained by subtracting the RAIR spectrum without E field from that with E field.**



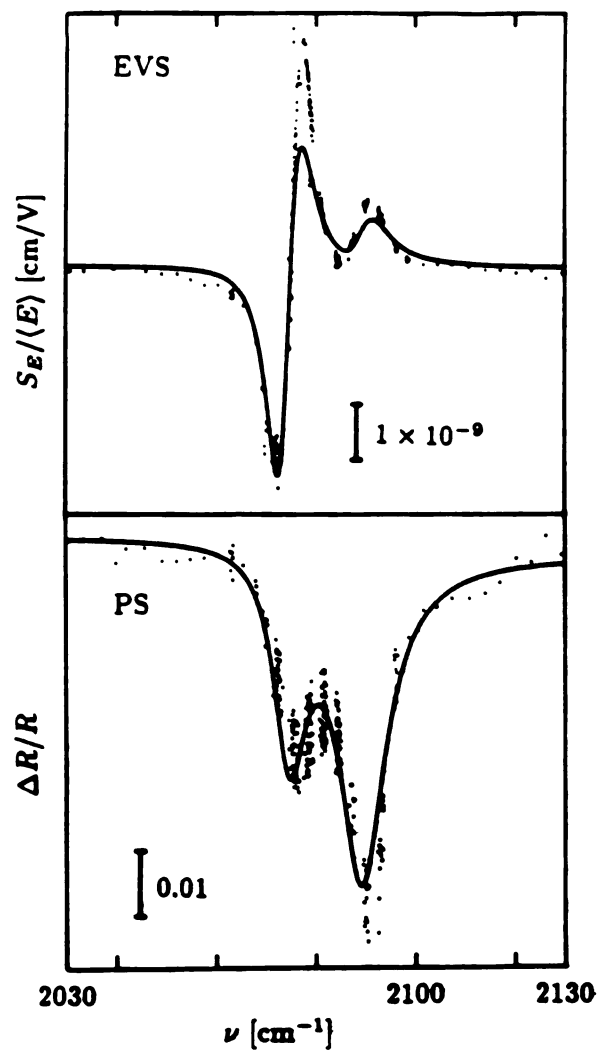


Figure 3-4. Comparison between the measured spectra at 0.54 ML and spectra calculated from the dipole coupling model discussed in the text and illustrated in Figure 3-3.

**References**

1. D.K. Lambert, J. Chem. Phys. **89**, 3847 (1988).
2. D.K. Lambert, J. Chem. Phys. **94**, 6237 (1991).
3. D.K. Lambert, Solid State Commun. **51**, 297 (1984).
4. P.S. Bagus, C.J. Nelin, W. Muller, M.R. Philpott and H. Seki, Phys. Rev. Lett. **58**, 559 (1987).
5. C.W. Bauschlicher, Jr., Chem. Phys. Lett. **118**, 307 (1985).
6. D.K. Lambert and R.G. Tobin, Surf. Sci. **232**, 149 (1990).
7. B. Diu, F. Laloe and C. Cohen-Tannoudji, *Quantum Mechanics V.2*, (Wiley, New York, 1977).
8. R.G. Greenler, J.A. Dudek and D.E. Beck, Surf. Sci. **145**, L453 (1984).
9. R.G. Greenler, F.M. Leibsle and R.S. Sorbello, Phys. Rev. B **32**, 8431 (1985).
10. F.M. Leibsle, R.S. Sorbello and R.G. Greenler, Surf. Sci. **179**, 101 (1987).
11. B.E. Hayden, K. Kretzschmar, A.M. Bradshaw and R.G. Greenler, Surf. Sci. **149**, 394 (1985).
12. J.E. Reutt-Robey, D.J. Doren, Y.J. Chabal and S.B. Christman, J. Chem. Phys. **93**, 9113 (1990).
13. J.E. Reutt-Robey, Y.J. Chabal, D.J. Doren and S.B. Christman, J. Vac. Sci. Technol. A **7**, 2227 (1989).

## CHAPTER 4

# VIBRATIONAL OVERTONES OF CO ON Pt(335): EVIDENCE FOR ANOMALOUS ELECTROSTATIC SCREENING

### I. Introduction

The experimental investigation presented in this chapter was also submitted to the *Journal of Chemical Physics* [1].

In discussing the interactions between adsorbates, it is customary and often useful to distinguish between "chemical" and "physical" effects. While the distinction is arbitrary and rarely sharp, "chemical" effects depend fundamentally on the rearrangement of electronic states arising from the chemisorption bond, while "physical" effects can be understood in terms of classical mechanics and electrodynamics. For example, the C=O stretch frequency of adsorbed CO is different from the gas phase value, in part because of dipole coupling to its own image [2] and dynamic coupling to the adsorbate-substrate vibrations [3]; these can be regarded as "physical effects". The dominant effect, however, is the backdonation of electrons from the metal into the  $2\pi^*$  orbital of the molecule [4], a "chemical" effect. A shift in the C=O stretch frequency is usually observed as the CO coverage varies. This shift is caused in part by dipole-dipole coupling within the layer ("physical") and in part by coverage-dependent changes in the electronic structure of the adsorbate ("chemical").

Even when the distinction between physical and chemical effects is conceptually clear, it is often difficult to separate them experimentally. The dipolar and chemical contributions to frequency shifts can be separated

through isotopic dilution experiments [5,6,7,8,9,10,11,12,13] (related discussion can also be found in Chapter 6). In other cases, theoretical calculations or the comparison of experiments on different adsorption systems can provide insight.

In this work, we report new electron energy loss spectroscopy (EELS) measurements of the fundamental and overtone transitions of CO on the stepped Pt(335) surface. Lambert and Tobin [14] have determined that the Stark tuning rate of atop CO on this surface is smaller by an order of magnitude at sites on the (111) oriented terraces than on the step edges; more detail can be found in Chapter 3. Through a quantitative analysis of the overtone intensity as a function of CO coverage, we assign this difference in Stark tuning rates to a "physical" mechanism -- anomalous screening of the DC electric field at terrace sites -- rather than a "chemical" mechanism -- a difference in electronic structure of CO between the two sites. Such a large difference in electrostatic screening is very surprising; we discuss its significance near the end of this chapter.

## II. Background

The motivation for this experiment comes from measurements of the vibrational Stark effect of CO on stepped and flat Pt surfaces. Results obtained by Lambert and Tobin [14] and our measurements presented in Chapter 6 indicate the following values for the apparent Stark tuning rate  $dv/dE$  of atop CO on the stepped Pt(335) and flat Pt(111) surfaces:

Pt(111)	$7.5 \pm 0.9$
Pt(335), step edge	$7.5 \pm 2.0$
Pt(335), terraces	$\leq 0.8$

The stepped Pt(335) surface consists of (111) terraces four atoms wide separated by monatomic height steps of (100) orientation as shown in Figure 4-1. The estimates of  $dv/dE$  for this surface assume (incorrectly, we will demonstrate) that the screening of the static field is the same as that of the IR field, as expected from standard dipole couple coupling models [2,6,15] (also see Chapters 3 and 6). The anomalously low tuning rate of the electrostatic field is dramatically suppressed at terrace sites compared with edge sites or sites on the flat (111) surface. The EELS measurements presented here provide the additional information necessary to distinguish between the two mechanisms.

The intrinsic (local field) Stark tuning rate  $dv/dE$  ( where  $E$  is the local electrostatic field acting on the adsorbed molecule) is closely related to the dipole matrix element of the overtone ( $\nu=0 \rightarrow 2$  transition) of the same vibration. Within the Bohn-Oppenheimer approximation, both the Stark tuning rate and the intensity of the overtone depend, to lowest order in perturbation theory, on the cubic anharmonicity  $a_{30}$  of the potential and on the quadratic term  $a_{21}$  in the dipole moment expansion [16]; detailed derivation for the Stark tuning rate can be found in Chapter 3. Specifically, the Stark tuning rate is given by [17]

$$\frac{dv}{dE} = \frac{a_{11}}{4\pi\sqrt{2\mu}a_{20}} \left( \frac{2a_{21}}{a_{11}} - \frac{3a_{30}}{a_{20}} \right) = \frac{a_{11}}{4\pi\sqrt{2\mu}a_{20}} \left( \frac{3a_{30}}{a_{20}} \right) (\beta - 1) \quad (1)$$

and the ratio of overtone intensity to fundamental intensity by EELS is [16,18]

$$\begin{aligned} \frac{I_2}{I_1} &= \frac{f_2}{f_1} \frac{\hbar}{4\sqrt{2\mu a_{20}}} \left( \frac{2a_{21}}{a_{11}} + \frac{a_{30}}{a_{20}} \right)^2 \\ &= \frac{f_2}{f_1} \frac{\hbar}{4\sqrt{2\mu a_{20}}} \left( \frac{a_{30}}{a_{20}} \right)^2 (1 + 3\beta)^2 \end{aligned} \quad (2)$$

where  $\mu$  is the reduced mass,  $f_1$  and  $f_2$  are related to the EELS sensitivity at fundamental and overtone loss, respectively, and the ratio  $\beta$  is defined as

$$\beta = \frac{2a_{21}/a_{11}}{3a_{30}/a_{20}}. \quad (3)$$

Equation (3) describes the relative significance of the anharmonicity of the potential and the non-linearity of the dipole moment. For  $\beta \approx 0$ , both the Stark tuning rate and the overtone intensity are dominated by the anharmonic term  $a_{30}$ ; this is the case for CO in the gas phase and on Ni(100) [17] and for methoxy on Ni(111) [19]. For  $\beta \approx 1$ , anharmonicity and dipole non-linearity make equal and opposite contributions to the Stark tuning rate, resulting in zero Stark shift; the overtone intensity is then dominated by the  $a_{21}$  term.

We will use Equations (1), (2), and (3) to analyze the behavior of CO on Pt(335), even though the approximation of isolated molecules is an oversimplification. Because of the strong dipole-dipole coupling between the adsorbates, a proper description would treat the fundamental and overtone transitions as surface phonons, rather than localized vibrations [6,14,19,20]. We justify our approximation by noting that dipole-dipole coupling was explicitly (if simplistically) included in determining the Stark tuning rates in Ref. [14] (more discussion can be found in Chapter 3), and that our EELS analysis will deal only with the ratio of the overtone to fundamental intensity. To a first approximation, the effect of dipole coupling on the intensity arises only from the frequency-independent electronic polarizability of the CO [6],

and should be the same for the overtone as for the fundamental. The use of formulae strictly appropriate only for isolated molecules therefore introduces no serious error. (The same could not be said, of course, if our analysis depended on the frequencies of the modes.)

The fixed parameters used in our analysis are given in Table 4-1. All parameters are determined from independent experimental data. The curvature of the potential  $a_{20}$  and the linear dynamic dipole moment  $a_{11}$  are taken from the IR measurements of Lambert and Tobin [14]. The cubic anharmonicity  $a_{30}$  is estimated by an indirect method described in detail below. The EELS parameters  $f_1$  and  $f_2$  are calculated from the known characteristics of our EELS system; this calculation is also discussed below. For free CO,  $\beta \approx 0.017$ ; we determine  $\beta_e$  (for edge CO) from the Stark tuning rate, and treat  $\beta_t$  (for terrace CO) as a parameter to be determined from our data. We assume (except as indicated) that the parameters listed in Table 4-1 are equal for edge and terrace CO. The measured Stark tuning rate for edge CO, combined with our estimate of  $a_{30}$ , requires that  $\beta_e$  lie between 0 and 0.35, consistent with the small values found for gas phase CO and for CO on Ni(100) [17].

If the small apparent tuning rate of terrace CO is to be explained by a chemical mechanism, then either the anharmonicity of terrace CO is greatly reduced,  $(a_{30})_{\text{terrace}} \approx (a_{30})_{\text{terrace}}/10$ , or the usual anharmonicity is compensated by a highly non-linear dipole moment,  $\beta = 1.0 \pm 0.1$ . It is unlikely that the anharmonicity  $a_{30}$  is significantly different at the sites, since it is closely related to the dissociation energy  $D_e$ . If the C=O potential is modeled by a Morse potential, for example,  $D_e \approx (a_{30})^{-2}$ , and a difference in  $a_{30}$  of a factor of ten would imply a difference in  $D_e$  of a factor of 100. The measured difference in  $E_a(\text{CO})$ , energy released from CO adsorption on the surface, between edge and terrace CO, however, is less than 20 kcal/mole

[21,22,23,24,25], which leads (see Equation (6)) to only about a 10% variation in  $D_e$ . Even if  $E_a(C)$ , energy released from C adsorption, were zero at edge sites,  $D_e$  would increase by only a factor of two. Accordingly, we wish to test the other possibility, that the dipole non-linearity  $a_{21}$  (or equivalently  $\beta$ ) is much larger for terrace CO than for edge CO.

A consequence of this hypothesis (evident from Equation (2)) would be an enhanced overtone intensity for terrace CO compared to edge CO. If  $\beta_e \approx 0$  and  $\beta_t \approx 1$ , as required by a chemical explanation for the Stark tuning rates, the overtone intensity per molecule would be 16 times greater for terrace than for edge CO; this difference would appear in the coverage dependence of the overall (edge + terrace) overtone intensity. At low coverage, CO on Pt(335) predominantly occupies edge sites [14,20,21]. Terrace sites begin to be occupied at  $\theta \approx 0.15$  and the terrace coverage increases rapidly between  $\theta = 0.15$  and  $\theta = 0.4$ ; refer to Chapter 5 for more detailed information. We would therefore expect a dramatic increase in the total overtone intensity in this coverage region. No such increase is observed. In fact, we find *no* significant difference in overtone intensity between terrace CO and edge CO, and therefore no significant difference in  $dv/dE$ . The apparent difference observed by Lambert and Tobin [14] must be caused instead by a difference in the local  $E$  field.

### III. Experimental

The EELS apparatus, procedures for sample preparation, and analysis of data obtained from temperature programmed desorption have been described in Chapter 2. The sample was held at 100 K for EELS measurements. Annealing significantly affected the fundamental peaks at coverage above  $\theta = 0.3$ , and



the double loss and overtone peaks were affected at all coverages. A second annealing did not change the spectra further. While EEL spectra were measured both before and after annealing, only the data for the annealed surfaces are considered here. Coverages were determined by TPD, assuming  $\theta = 0.625$  at saturation, as determined by Lambert and Tobin [14].

To reduce scanning time and the possibility of contamination by background gases, the spectra were scanned only from 1800 to 4500  $\text{cm}^{-1}$ ; the elastic peak was not routinely measured. To compensate for possible variations in spectrometer efficiency, we normalized all overtone and double loss intensities to the intensity of the appropriate fundamental peak. Since the width of each peak was limited by the spectrometer resolution, intensities were determined from the peak height above a smooth baseline. The error bars were determined from the noise in the spectra.

## IV. Results and Analysis

### IV.1. Atop Overtone Intensity

Figure 4-2 shows EEL spectra in the specular direction measured at various CO coverages. Five peaks can be detected at  $\nu_b$ ,  $\nu_a$ ,  $2\nu_b$ ,  $\nu_b + \nu_a$ , and  $2\nu_a$ , in order of increasing frequency, where the subscripts  $b$  and  $a$  refer to bridge CO and atop CO, respectively. Edge and terrace CO cannot be distinguished with EELS. We designate the intensities of these five peaks as  $I_b$ ,  $I_a$ ,  $I_{2b}$ ,  $I_{ab}$ , and  $I_{2a}$ . In Figure 4-3, we show the normalized intensities of the three high-frequency peaks:  $I_{2a}/I_a$ ,  $I_{ab}/I_a$ , and  $I_{2b}/I_a$ .

Loss features in EELS can arise from three processes: dipole scattering, impact scattering, and resonance scattering [26]. Our analysis is concerned only with dipole losses, for which a satisfactory and general theory of

intensities is available; in particular, Equation (2) applies only to dipole excitation. It is well established [27,28,29,30] that the C=O stretch fundamental is well described by dipole scattering for spectra measured in the specular direction; we will assume that  $I_a$  and  $I_b$  are purely dipole loss intensities. There is some evidence that overtone intensities are also dominated by dipole scattering [29,31,32], but a fraction of the intensity may come from non-dipole processes, and the overtone peaks usually overlap with multiple loss peaks of comparable intensity [29,31,33], which are excited primarily by non-dipole processes [26,31,32].

We focus our attention primarily on the peak at  $2\nu_a$ . Figure 4-3(a) shows that  $I_{2a}/I_a$  is nearly constant in the 0.15-0.4 ML coverage region, in contrast to the sharp increase expected from a chemical model for the Stark tuning rate variations. But a proper analysis requires that we separate the overtone dipole loss intensity from contributions from other processes. We represent the total intensity  $I_{2a}$  as a sum of two independent components, a dipole overtone  $I_{oa}$  and a non-dipole term  $I_{aa}$ , due to double losses and non-dipole excitations of the overtone.

We assume that the dipole overtone intensity per molecule for each species (edge and terrace) is given by Equation (2) with the parameters in Table 4-1 and appropriate values of  $\beta_e$  and  $\beta_i$ . Non-dipole scattering in EELS [26,27,28] is not yet well enough understood to make quantitative predictions of intensities or even of the dependence on CO coverage. There is experimental evidence, however, that the dependence on coverage is stronger than linear [32,33]. We therefore model the non-dipole intensity  $I_{aa}$  as a general power law:

$$I_{aa} = C(\theta)^\eta \quad (4)$$

where we treat the constants  $C$  and  $\eta$  as adjustable parameters. The exponent  $\eta$  is related to the degree of correlation of the two scattering events. The probability of a single loss should be proportional to  $\theta_a$ . The most natural assumption [34], that the second event is independent of the first, gives  $\eta = 2$ . Chen et al. found that  $\eta = 2$  for high coverages of  $\text{Al}_2\text{O}_3$  on Al [32]. If the probability of the second event is reduced by the occurrence of the first, the exponent  $\eta$  will be greater than 2. On the other hand, if the probability of the second event is *enhanced* by the occurrence of the first,  $\eta$  will be smaller than 2; for complete correlation,  $\eta = 1$ .

Once we have selected a value for  $\beta_i$ , the dipole overtone intensity  $I_{oa}(\theta)$  is completely specified at all coverages by Equation (2), using the other parameters from Table 4-1 and the model presented in Chapter 5 [21] for the populations of edge and terrace atop CO. We then choose an exponent  $\eta$  to characterize the coverage dependence of the non-dipole loss  $I_{aa}$ . The only other parameter required for a complete calculation of  $I_{2a}(\theta)$  is the constant  $C$  that determines the overall magnitude of  $I_{aa}$ ; we adjust  $C$  to obtain the best fit to the data. For each value of  $\beta_i$  and  $\eta$ ,  $C$  is the only freely adjustable parameter. Empirical support for this approach is discussed below.

Figure 4-4(a) compares the normalized  $2\nu_a$  intensity from Figure 4-3(a) with model calculations for several values of  $\beta_i$ , assuming uncorrelated double loss scattering,  $\eta = 2$ . Higher values of the exponent  $\eta$  give essentially identical results. Figure 4-4(b) shows a similar set of model calculations, assuming that the double loss events are completely correlated ( $\eta = 1$ ).

It is apparent from Figure 4-4 that values of  $\beta_i$  approaching 1 are excluded by the data. As expected, for  $\beta_i > \beta_c$ , the models predict a large increase in  $I_{2a}/I_a$  between  $\theta = 0.15$  and  $\theta = 0.40$ , which is not present in the

data. In fact, for the parameter values in Table 4-1, we can exclude values of  $\beta_i$  greater than about 0.4; this maximum value of  $\beta_i$  corresponds to a Stark tuning rate for terrace CO of  $5.8 \times 10^{-7} \text{ cm}^{-1}/(\text{V}/\text{cm})$ , more than seven times greater than the upper limit set by Lambert and Tobin [14]. A chemical mechanism affecting  $a_{21}$  clearly *cannot* account for the small tuning rate of terrace CO.

We have performed extensive calculations to investigate the sensitivity of our results to the values and assumptions used in Figure 4-4. While variations in any of the parameters will change the optimum value of  $\beta_i$  and the quality of the fit, by far the most significant parameters are the anharmonicity  $a_{30}$  and the EELS sensitivity ratio  $f_2/f_1$ .

We estimate  $a_{30}$  by the method described by Lambert [17], using the gas phase value of  $a_{30}$  [35] and the dissociation energies  $D_e$  of free and adsorbed CO:

$$(a_{30})_{\text{ads}} = (a_{30})_{\text{gas}} \left( \frac{(D_e)_{\text{gas}}}{(D_e)_{\text{ads}}} \right)^{1/2} \left( \frac{\nu_{\text{ads}}}{\nu_{\text{gas}}} \right)^3. \quad (5)$$

The dissociation energy of adsorbed CO is not known directly, but can be estimated as

$$(D_e)_{\text{ads}} = (D_e)_{\text{gas}} + E_a(\text{CO}) - E_a(\text{C}), \quad (6)$$

where  $E_a(\text{CO})$  and  $E_a(\text{C})$  are the adsorption energies of CO and C. For the Pt(111) surface, Shustarovich and Bell [36] give  $(D_e)_{\text{gas}} = 257 \text{ kcal/mole}$ ,  $E_a(\text{CO}) = 32 \text{ kcal/mole}$ , and  $E_a(\text{C}) = 150 \text{ kcal/mole}$ , so that  $(D_e)_{\text{ads}} = 139 \text{ kcal/mole}$ . The least certain of these is  $E_a(\text{C})$ , which is an extrapolation [37] from the measured value of 171 kcal/mole for C on Ni(111). From the values tabulated in Ref. [36] it is apparent that the heats of adsorption of small molecules on Pt(111) and Ni(111) rarely differ by more than about 25%, and that  $E_a$  on Pt is

invariably smaller than on Ni. It appears reasonable to assume that  $125 < E_a(\text{C}) < 175$  kcal/mole, which leads to the range of values for  $a_{30}$  given in Table 4-1. (The value of 63 kcal/mole used in Ref. [17] was a very crude estimate made in the absence of experimental data for carbon adsorption energies [38].) Varying  $a_{30}$  over this range does not appreciably change our conclusions; the minimum value allows  $\beta_i$  to reach about 0.6, but values close to 1.0 are still excluded unless  $f_2/f_1$  is much smaller than assumed.

The ratio  $f_2/f_1$  directly affects the size of the overtone component of  $I_{2a}$  (see Equation (2)). If this ratio is much smaller than we have assumed, then most of  $I_{2a}$  comes from the double loss, and our measurements tell little about  $\beta_i$ . In the dipole theory of specular EELS, the factor  $f(\phi, \omega, E_0)$  accounts for the finite angular acceptance of the spectrometer:

$$f = \frac{\sin^2 \phi - 2 \cos^2 \phi}{1 + \alpha^2} + (1 + \cos^2 \phi) \ln(1 + 1/\alpha^2) \quad (7)$$

$$\alpha = \hbar\omega/(2E_0 \vartheta_c), \quad (8)$$

where  $\phi$  is the angle of incidence,  $E_0$  is the primary beam energy,  $\omega$  is the loss frequency, and  $\vartheta_c$  is the acceptance angle of the spectrometer [29,30]. For our experimental conditions,  $\alpha = 1.67$  for the fundamental and 3.34 for the overtone and  $\phi = 60^\circ$ ; the first term in Equation (7) is negligible and  $f_2/f_1 \approx \alpha_1^2/(2\alpha_1)^2 = 0.25$ , where  $\alpha_1$  is the value of  $\alpha$  at fundamental frequency. A more accurate calculation gives  $f_2/f_1 = 0.3$ . This quantity is rather insensitive to the exact values of  $\alpha$  and  $\phi$ , and is in any case no lower than 0.25. To the extent that the dipole theory is adequate,  $f_2/f_1$  should be quite close to our calculated value of 0.3. There is always the possibility, however, of unexpected experimental effects, so we have explored the effect of changes in  $f_2/f_1$  on our conclusions.

Figure 4-5 summarizes the effects of the exponent  $\eta$  and the ratio  $f_2/f_1$  on our estimate of  $\beta_i$ . We plot the reduced chi-squared [39]  $\chi^2_\nu$  for the model as a function of  $\beta_i$  for various values of  $f_2/f_1$  and for both  $\eta = 2$  and  $\eta = 1$ . The minimum  $\chi^2_\nu$  for  $\eta = 2$  and  $f_2/f_1 = 0.3$  is 1.64 and occurs at  $\beta_i = 0.15$ . Since  $\chi^2_\nu \approx 1$  indicates good agreement, and in view of the uncertainties and approximations involved, we regard this as a reasonable fit to the data. For smaller values of  $\beta_i$ , the increase in  $\chi^2_\nu$  is slight, but  $\chi^2_\nu$  increases rapidly for higher values of  $\beta_i$ . If  $f_2/f_1$  is much smaller than our estimated value, but the fit also becomes significantly inferior. For  $\eta = 1$ , the trends are the same, but the values of  $\chi^2_\nu$  are consistently higher, suggesting that double loss scattering is not highly correlated. The minima are flatter than for  $\eta = 2$ , but values of  $\beta_i$  greater than 0.8 are ruled out provided that  $f_2/f_1 > 0.1$ ; only if the spectrometer sensitivity decreases unexpectedly by a factor of 3 between 2000 and 4000  $\text{cm}^{-1}$  can  $f_2/f_1$  reach such a low value. To stretch the parameters this far strains the limits of credibility.

Two observations provide empirical support for our method of analysis and choice of parameters. First, at low coverage only edge sites are occupied, so  $I_{oa}/I_a$  is completely determined by Equation (2) and the parameters in Table 4-1. At the same time, if  $\eta > 1$ , as indicated by experiment [32,33], then the non-dipole term  $I_{aa}/I_a$  is negligible at low coverage, and  $I_{2a} \approx I_{oa}$ . Our model therefore predicts  $I_{2a}/I_a$  at low coverage with no adjustable parameters. The good agreement evident in Figure 4-4(a) supports the validity of Equation (2) and the parameter values in Table 4-1. In particular, a value of  $f_2/f_1$  as low as 0.1 would result in too little intensity at low coverages.

Additional support for our model comes from loss spectra measured off the specular direction at saturation coverage, shown in Figure 4-6. These data confirm that the fundamentals  $I_a$  and  $I_b$  are dipole losses, while the double loss

$I_{ab}$  is largely non-dipole, in agreement with other research [31,32,33]. Figure 4-7(a) shows (on a log scale) the intensities of the elastic peak, the two fundamental peaks, and two of the high frequency peaks as a function of off-axis angle. The peak at  $I_{2b}$  was too weak to be measured off the specular direction. In Figure 4-7(b), the intensities  $I_a$ ,  $I_{2a}$ , and  $I_{ab}$  are replotted on a linear scale, normalized to their intensities in the specular direction. The behavior of  $I_{2a}$  is intermediate between that of the dipole loss  $I_a$  and the non-dipole double loss  $I_{ab}$ , indicating that both dipole and non-dipole processes contribute significantly to the total intensity.

A rough independent test of our separation of  $I_{2a}$  into dipole and non-dipole components can be derived from the off-specular data. If we assume that the non-dipole component  $I_{aa}$  has the same dependence on off-specular angle as the atop-bridge double loss  $I_{ab}$ , while the dipole overtone  $I_{oa}$  has the same dependence as the fundamental  $I_a$ , we estimate that between 25% and 75% of  $I_{2a}$  at saturation coverage comes from the dipole term. This is similar to the results of other groups: Andersson and Davenport [29] found  $I_{oa}/I_{2a} \approx 0.3$  for CO on Ni(100); dePaola and Hoffmann [31] found  $I_{oa}/(I_{aa} + I_{oa}) \approx 0.2$  for CO on potassium-predosed Ru(001). For our system, the ratio  $I_{oa}/I_{2a}$  at saturation for each model calculation is given in the caption to Figure 4-4. For the parameter values that best fit the data ( $\eta = 2$ ,  $\beta_i \approx 0.15$ ), the calculation gives  $I_{oa}/I_{2a} \approx 0.5$ , in the middle of the range estimated from off-specular measurements.

In summary, we can exclude the possibility of a large enhancement of the overtone intensity of terrace CO on Pt(335) compared with edge CO. Specifically, the ratio  $\beta_i$  (Equation (3)) is constrained to the range  $0 < \beta_i < 0.40$ . That is, for terrace CO on Pt(335), as for CO in the gas phase, on Ni(100), and on Pt(111), the dipole moment non-linearity  $a_{21}$  is negligible compared to the anharmonicity of the potential. The largest allowed value of  $\beta_i$  would predict a

Stark tuning rate seven times greater than the upper limit set by Lambert and Tobin [14]. The small tuning rate of terrace CO cannot be explained by a chemical mechanism.

#### IV.2. Atop-Bridge Double Loss Intensity

The consistently better fits obtained for  $\eta = 2$  than for  $\eta = 1$  suggest that the scattering events that give rise to the double loss peak are either uncorrelated or negatively correlated. For O on Pt(111), Steininger et al. found that multiple losses varied more strongly with coverage than fundamentals or overtones [40]. We have closely examined the coverage dependence of the atop-bridge double loss intensity  $I_{ab}$  in the hope of clarifying the coverage dependence of double loss scattering. In the standard model of uncorrelated scattering events, we expect

$$I_{ab} \propto \theta_a \theta_b \quad (9)$$

so that  $I_{ab}/I_a \propto \theta_b$  and  $I_{ab}/I_b \propto \theta_a$ . Figure 4-8(a) compares the normalized intensity  $I_{ab}/I_a$  with the total bridge coverage from our model presented in Chapter 5 [21]. In Figure 4-8(b), the double loss intensity is normalized to the intensity of the *bridge* fundamental  $I_b$  and compared to the total atop coverage  $\theta_a$ . The data are not inconsistent with Equation (9), but no strong conclusion can be drawn regarding the detailed coverage dependence of double loss scattering.



## V. Conclusion

By demonstrating that the difference in Stark tuning rates between edge and terrace CO is *not* caused by chemical differences between the two species, this work contributes to a growing body of evidence that there are significant differences in our understanding of electric fields at surfaces. The data imply that the local electrostatic field at terrace sites on Pt(335) is about a factor of ten weaker than the local field on either edge sites or the flat (111) surface in the same applied field. Two questions immediately arise. First, what can account for such strong screening? Second, how can the *static* field be screened so much more strongly than the IR field?

Some enhancement of the field at the step edge relative to the terrace is in fact expected, but the effects should be relatively small. The "lightning rod" concentration of the field near a corner has been crudely estimated to account for a factor 1.5 difference in field strength between the edge and the terrace on Pt(335) [41], far too little to account for the variation in tuning rates. Some difference in screening by conduction electrons is also to be expected, as "smoothing" of the charge density [42,43] results in a deficit of electron density near the edge and a corresponding surplus on the terrace. Experimentally, the local work function at the step edge is found to be smaller by 1 eV than on the terrace [44,45], supporting the idea of a reduction of electron density at the step edge. A jellium calculation by Thompson and Huntington, however, found that the surplus electron density extends less than one lattice spacing across the terrace [43]. The reduction of the Stark tuning rate of terrace CO far below that of CO on Pt(111) is thus difficult to explain. Moreover, simple estimates suggest that the electron density does not extend far enough from the surface to screen the electric field near the center of the CO molecule by even as much as a factor of two on Pt(111) [14,15]; more

discussion on this point can be found in Chapter 6. Mechanisms involving conduction electron screening therefore seem quantitatively inadequate to explain the observation.

A more basic objection to such mechanisms is their frequency dependence. While the static field at terrace sites is evidently strongly suppressed, the IR field is not, as evidenced by the observed IR absorption intensity. Both Lambert and Tobin [14,15] and Reutt-Robey et al. [22] found that the apparent IR cross-section of CO is essentially the same on edge and terrace sites. Since the characteristic frequency for the response of conduction electrons is the plasma frequency,  $\approx 40,000 \text{ cm}^{-1}$  [46], it is difficult to account for a large difference in screening between DC and  $2000 \text{ cm}^{-1}$ . A similar objection applies to mechanisms involving the electronic polarizability of the adsorbates. (Moreover, dipole-dipole screening within the layer was taken explicitly into account by Lambert and Tobin [14].) The Stark tuning rate and IR intensity measurements for CO on Pt(111) presented in Chapter 6 provide additional evidence for a difference in the screening of static and IR fields [15].

We are unable to offer a plausible explanation for these screening anomalies. Their investigation is likely to be a fruitful area for both experimental and theoretical investigation.

The present work also demonstrates the usefulness of overtone intensities as a measure of chemical changes in adsorbed molecules. The combination of Stark effect and overtone intensity measurements is particularly powerful, since the overtone intensity can strongly constrain the intrinsic Stark tuning rate. The quantitative interpretation of EELS overtone intensities faces considerable obstacles, however, most importantly that of determining the non-dipole contribution. Although our work shows that

these obstacles can be overcome in favorable cases, infrared measurements of overtones could provide much more reliable information. The recent work of Zenobi et al. [19] on methoxy on Ni(111) demonstrates the feasibility of such measurements.

Table 4-1

Parameters used in the calculation of overtone intensities and Stark tuning rates for atop CO on Pt(335). Unless otherwise indicated, all parameters are assumed equal for edge and terrace CO. The nominal values represent our best estimates and were used for Figs. 4-6 and 4-7; the ranges represent the estimated uncertainties in the parameters. The parameters were varied over these ranges to test the sensitivity of the model. The dipole non-linearity parameter for edge CO,  $\beta_e$ , was determined from the Stark tuning rate  $dv/dE$ , through Equation (1). All values listed were determined from independent experiments, without reference to the present EELS data.

Parameter	Nominal Value	Range	Units	Reference
$a_{11}$	1.0	0.85 - 1.3	e	[12,14]
$a_{20}$	5.4	5.3 - 5.5	$10^{17}$ eV/cm <sup>2</sup>	[14]
$a_{30}$	1.7	1.5 - 1.9	$10^{26}$ eV/cm <sup>3</sup>	see text
$\mu$	6.86	—	amu	
$f_1/f_2$	0.3	0.25 - 0.35		see text
$dv/dE$ (edge)	7.5	5.5 - 9.5	$10^{-7}$ cm <sup>-1</sup> /(V/cm)	[14]
$dv/dE$ (terrace)	<0.8	—	$10^{-7}$ cm <sup>-1</sup> /(V/cm)	[14]

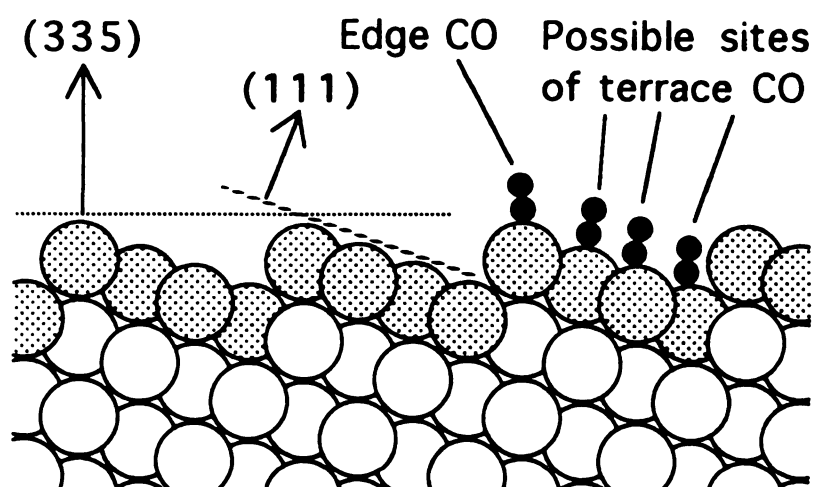


**Figure 4-1.** Side view of the Pt(335) surface, showing atop adsorption sites for edge and terrace CO.

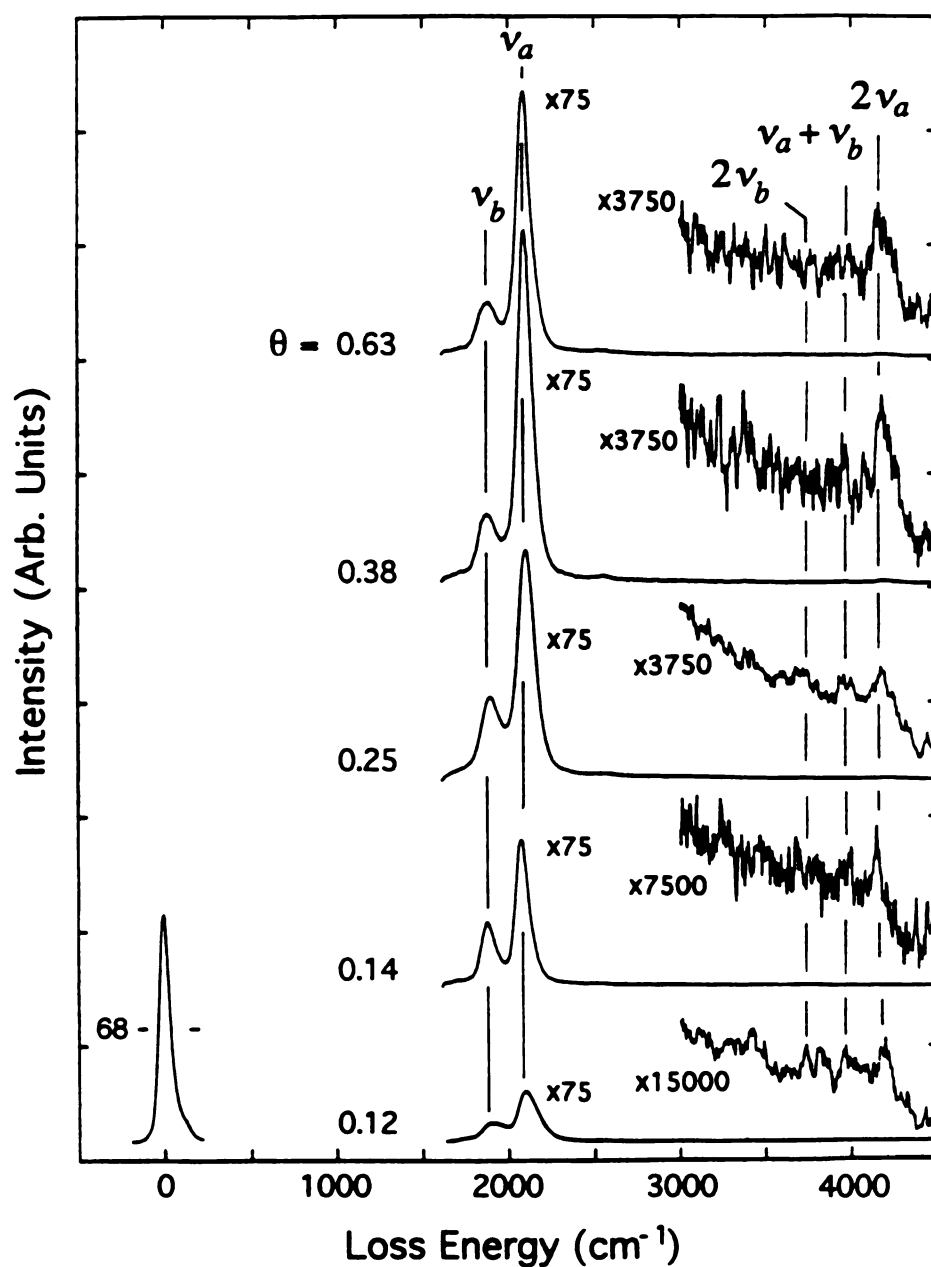


Figure 4-2. EEL spectra of CO on Pt(335) vs coverage. The sample was dosed with CO at 100 K, then annealed at 280 K for 1 minute to obtain an equilibrated layer. Spectra were measured with the sample at 100 K.

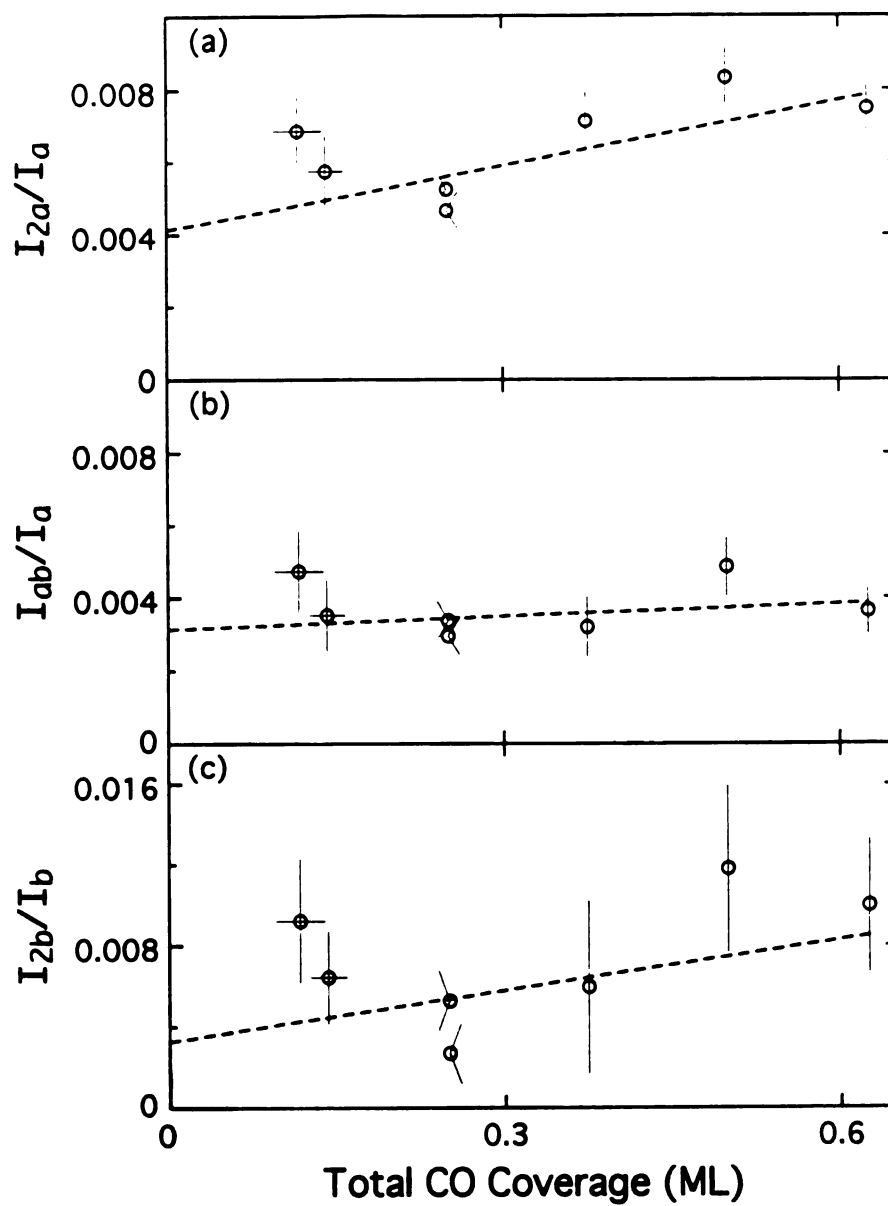


Figure 4-3. Normalized EELS intensities for the three high-frequency peaks, as a function of total CO coverage in monolayer (ML). The lines are linear fits to the data.

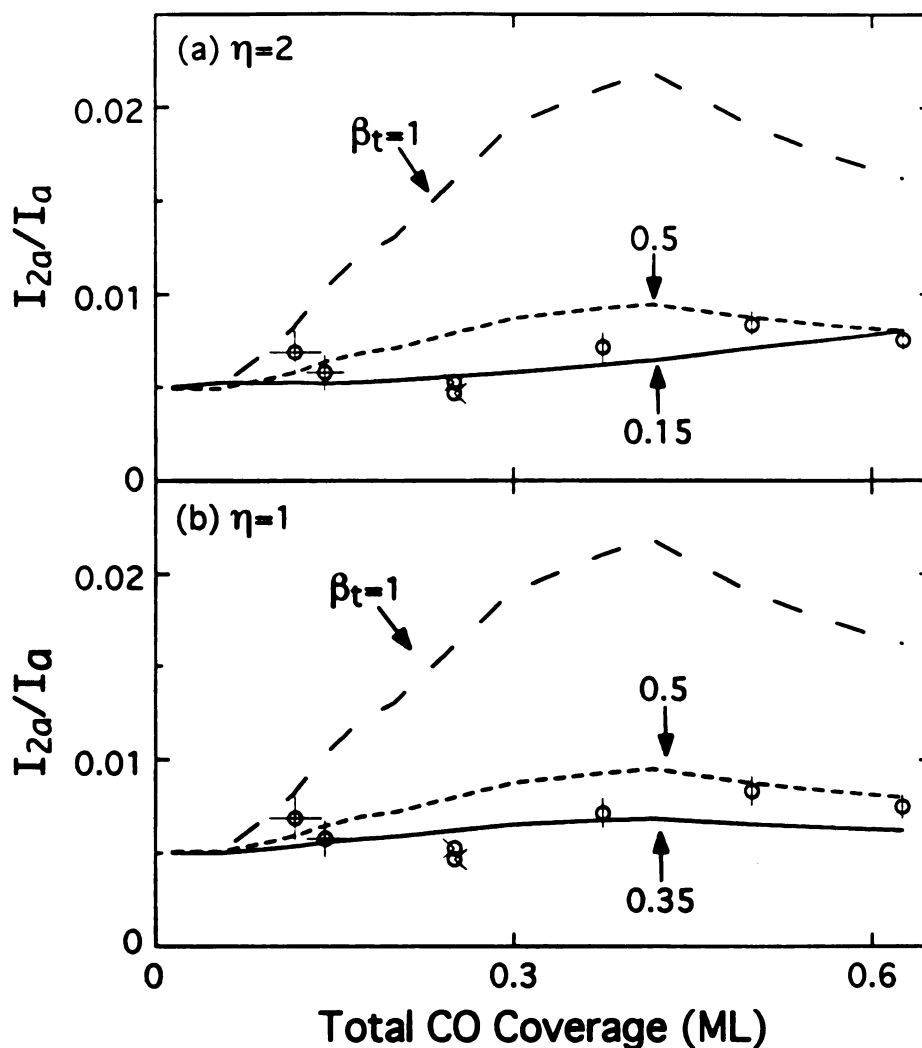


Figure 4-4. Comparison of the measured intensity ratio  $I_{2a}/I_a$  (from Figure 4-3) with calculated intensities for various values of  $\beta_t$ . A value of  $\beta_t$  close to 1 is required for a chemical explanation of the Stark tuning rate. See the text for a detailed description of the calculation. (a) Calculations assuming  $\eta = 2$  (uncorrelated double loss scattering). Only values of  $\beta_t < 0.4$  are consistent with the data; the best fit is for  $\beta_t = 0.15$ . The dipole contribution  $I_{oa}/I_{2a}$  at saturation is 0.53, 0.98 and 1.00 for  $\beta_t = 0.15$ , 0.5 and 1.0, respectively, compared to a range of 0.25 - 0.75 determined from off-specular EEL spectra. (b) Calculations assuming  $\eta = 1$  (fully correlated double scattering). The best fit is for  $\beta_t = 0.35$ .  $I_{oa}/I_{2a} = 0.98, 0.98$  and 1.00 for  $\beta_t = 0.35, 0.5$  and 1.0, respectively.



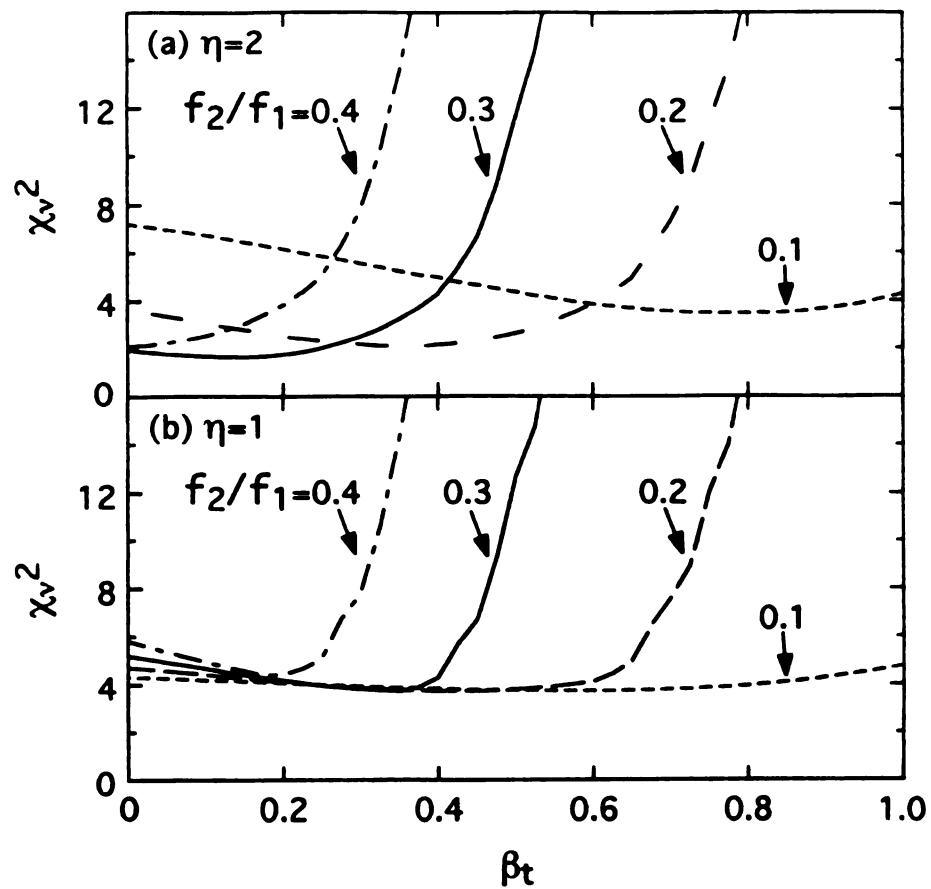


Figure 4-5. Reduced chi-squared  $\chi_v^2$  as a function of  $\beta_t$ , for various values of the EELS sensitivity ratio  $f_2/f_1$  and for (a)  $\eta = 2$  and (b)  $\eta = 1$ . Values of  $\beta_t$  approaching unity are possible only for unrealistically small values of  $f_2/f_1$ .

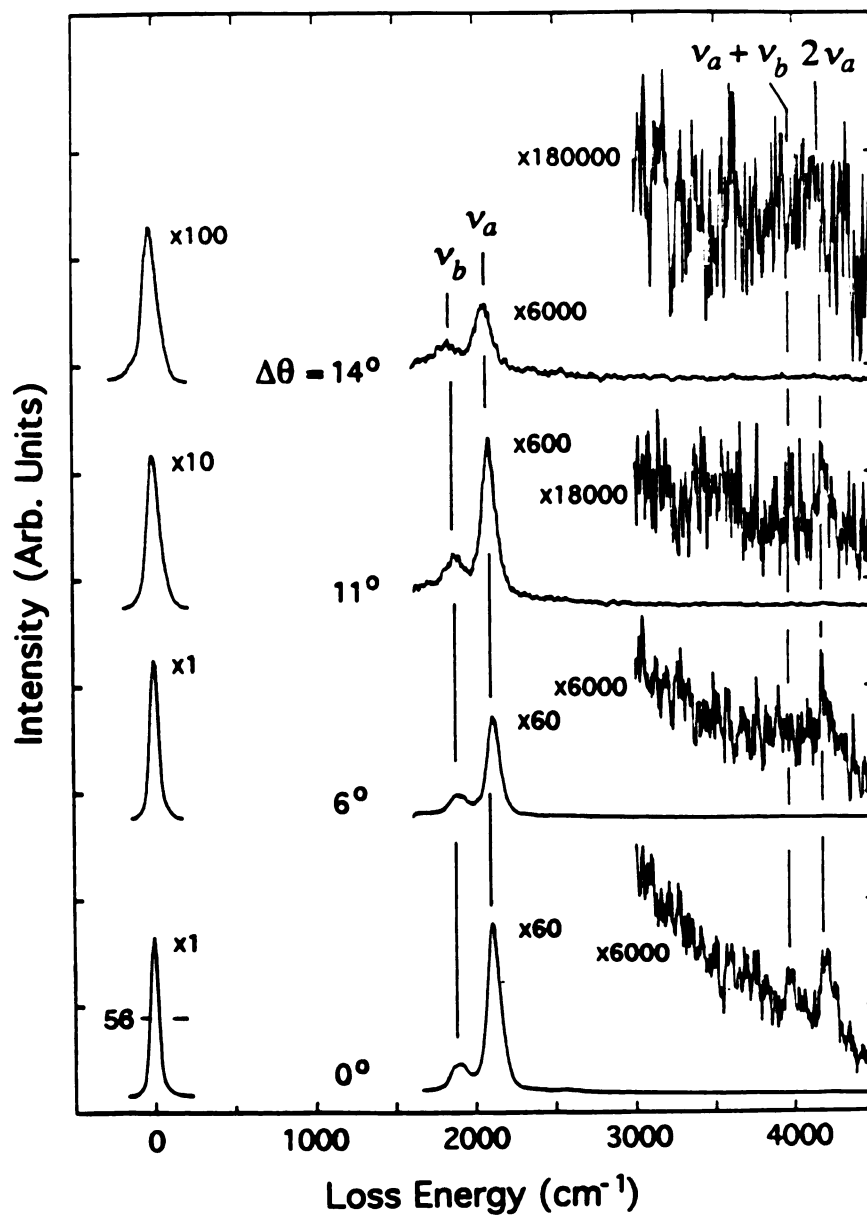


Figure 4-6. EEL spectra at saturation coverage (0.63 ML) in the specular direction and at three off-specular angles.

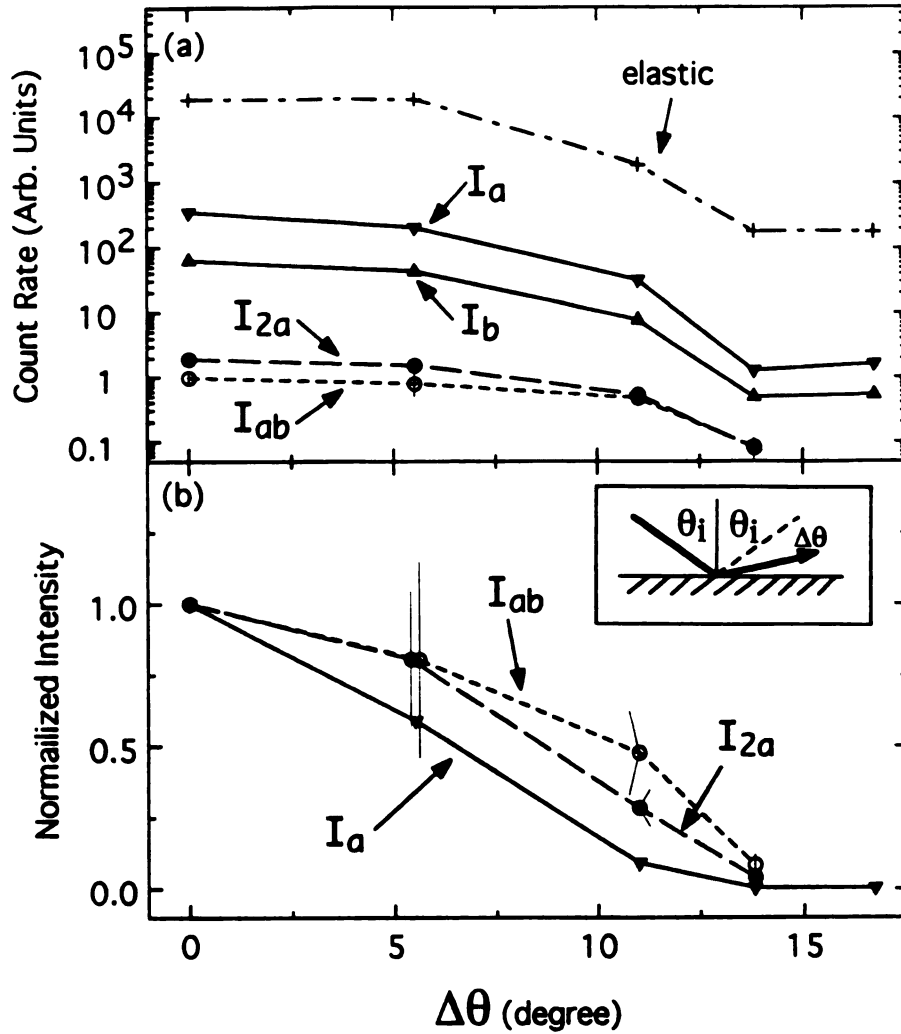


Figure 4-7. EELS intensities of the elastic peak and four loss peaks as a function of off-specular angle, from Figure 4-6. (a) Uncorrected intensities, on a logarithmic scale. (b) Intensities  $I_a$ ,  $I_{ab}$ , and  $I_{2a}$ , normalized to their respective values in the specular direction, on a linear scale. The angular dependence of  $I_{2a}$  is intermediate between the dipole loss  $I_a$  and the double loss  $I_{ab}$ .

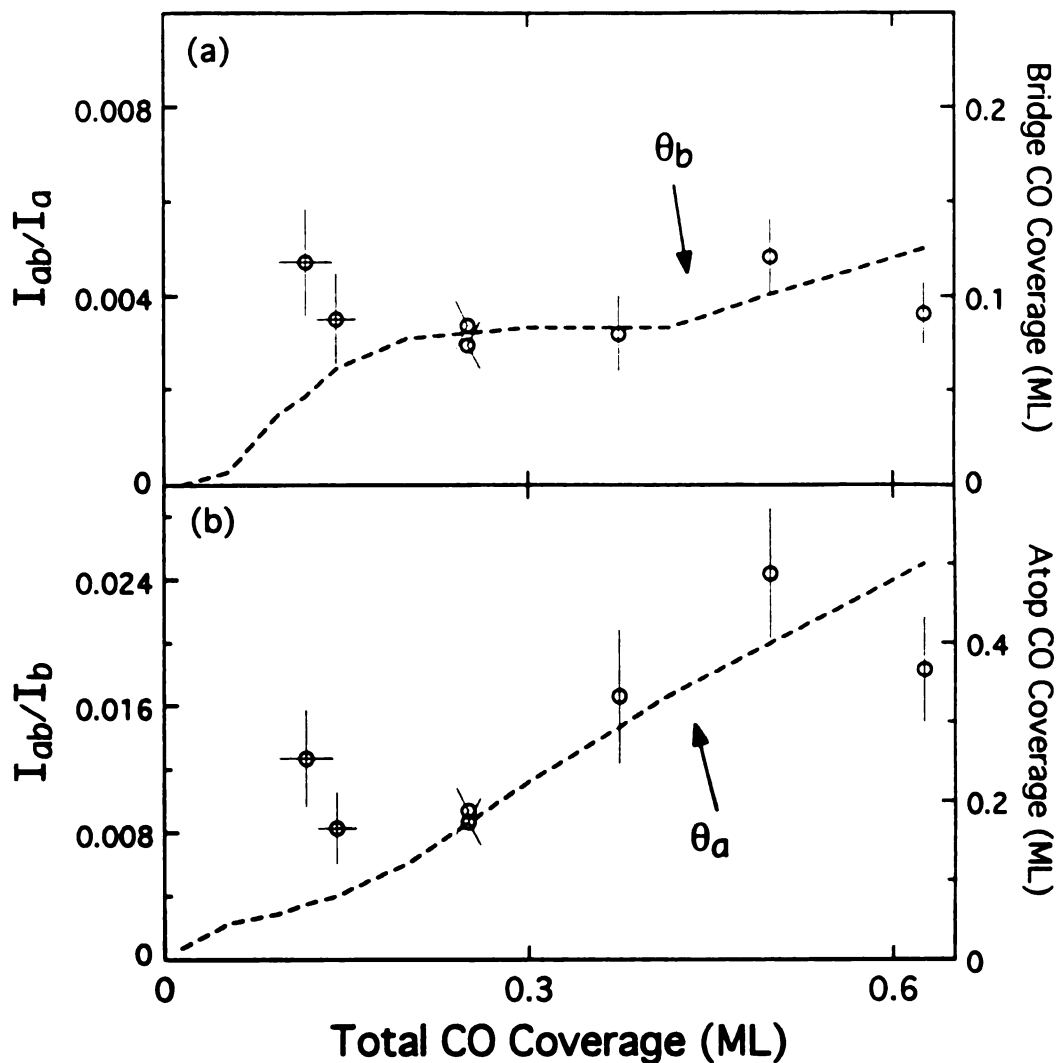


Figure 4-8. Comparison of the intensity ratios (a)  $I_{ab}/I_a$  (from Figure 4-3) with bridge coverage  $\theta_b$  (from Chapter 5) and (b)  $I_{ab}/I_b$  with atop coverage  $\theta_a$ , as a function of total CO coverage. For uncorrelated scattering, the EELS and coverage data should have the same coverage dependence in either plot. The data are too uncertain for a clear conclusion to be drawn.

**References**

1. J.S. Luo, R.G. Tobin, D.K. Lambert, G.B. Fisher and C.L. DiMaggio, (to be published).
2. M. Scheffler, Surf. Sci. **81**, 562 (1979).
3. J.W. Gadzuk, Phys. Rev. B **19**, 5355 (1979).
4. G. Blyholder, J. Phys. Chem. **68**, 2772 (1964).
5. R.A. Hammaker, S.A. Francis and R.P. Eischens, Spectrochim. Acta **21**, (1965).
6. B.N.J. Persson and R. Ryberg, Phys. Rev. B **24**, 6954 (1981).
7. A. Crossley and D.A. King, J. Chem. Phys. **68**, 1344 (1977).
8. R. Ryberg, Surf. Sci. **114**, 627 (1982).
9. B.N.J. Persson, F.M. Hoffmann and R. Ryberg, Phys. Rev. B **34**, 2266 (1986).
10. P. Hollins and J. Pritchard, Surf. Sci. **89**, 486 (1979).
11. A. Ortega, F.M. Hoffmann and A.M. Bradshaw, Surf. Sci. **119**, 79 (1982).
12. E. Schweizer, B.N.J. Persson, M. Tushaus, D. Hoge and A.M. Bradshaw, Surf. Sci. **213**, 49 (1989).
13. C.W. Olsen and R.I. Masel, Surf. Sci. **201**, 444 (1988).
14. D.K. Lambert and R.G. Tobin, Surf. Sci. **232**, 149 (1990).
15. J.S. Luo, R.G. Tobin and D.K. Lambert, (to be published).
16. J.S. Luo, R.G. Tobin, D.K. Lambert, F.T. Wagner and T.E. Moylan, J. Electron Spectrosc. Relat. Phenom. **54/55**, 469 (1990).
17. D.K. Lambert, J. Chem. Phys. **89**, 3847 (1988).
18. H. Ibach and D.L. Mills, *Electron Energy Loss Spectroscopy and Surface Vibrations*, (Academic, New York, 1982).

19. R. Zenobi, Z. Xu, J.T. Yates, Jr., B.N.J. Persson and A.I. Volokitin, (to be published).
20. B.E. Hayden, K. Kretzschmar, A.M. Bradshaw and R.G. Greenler, *Surf. Sci.* **149**, 394 (1985).
21. J.S. Luo, R.G. Tobin, D.K. Lambert, G.B. Fisher and C.L. DiMaggio, *Surf. Sci.* **274**, 53 (1992).
22. J.E. Reutt-Robey, D.J. Doren, Y.J. Chabal and S.B. Christman, *J. Chem. Phys.* **93**, 9113 (1990).
23. R.W. McCabe and L.D. Schmidt, *Surf. Sci.* **66**, 101 (1977).
24. H.R. Siddiqui, X. Guo, I. Chorkendorff and J.T. Yates, Jr., *Surf. Sci.* **191**, L813 (1987).
25. D.M. Collins and W.E. Spicer, *Surf. Sci.* **69**, 85 (1977).
26. P.A. Thiry, M. Liehr, J.J. Pireaux and R. Gaudano, *Physica Scripta* **35**, 368 (1987).
27. A.M. Baro' and H. Ibach, *Surf. Sci.* **103**, 248 (1981).
28. R.E. Palmer and P.J. Rous, *Rev. Mod. Phys.* **64**, 383 (1992).
29. S. Andersson and J.W. Davenport, *Solid State Commun.* **28**, 667 (1978).
30. H. Ibach, *Surf. Sci.* **66**, 56 (1977).
31. R.A. dePaola and F.M. Hoffmann, *Phys. Rev. B* **30**, 1122 (1984).
32. J.G. Chen, J.E. Crowell and J.T. Yates, Jr., *Phys. Rev. B* **35**, (1987).
33. H. Steininger, S. Lehwald and H. Ibach, *Surf. Sci.* **123**, 264 (1982).
34. J.C. Ariyasu and D.L. Mills, *Phys. Rev. B* **28**, 2389 (1983).
35. J.P. Bouanich, *J. Quant. Spectrosc. Radiat. Transfer* **19**, 381 (1978).
36. E. Shustarovich and A.T. Bell, *Surf. Sci.* **248**, 359 (1991).

37. E. Shustarovich, Adv. Catal. 37, 101 (1990).
38. W.H. Weinberg and R.P. Merrill, Surf. Sci. 39, 206 (1973).
39. P.R. Bevington and D.K. Robinson, *Data Reduction and Error Analysis for the Physical Science*, (McGraw-Hill, New York, 1992).
40. H. Steininger, S. Lehwald and H. Ibach, Surf. Sci. 123, 1 (1982).
41. R.G. Greenler, J.A. Dudek and D.E. Beck, Surf. Sci. 145, L453 (1984).
42. R. Smoluchowski, Phys. Rev. 60, 661 (1941).
43. M.D. Thompson and H.B. Huntington, Surf. Sci. 116, 522 (1982).
44. S. Kaiser and K. Wandelt, Surf. Sci. 128, L213 (1983).
45. Wandelt, J. Vac. Sci. Technol. A 2, 802 (1984).
46. M.A. Ordal, R.J. Bell, R.W. Alexander, Jr., L.L. Long and M.R. Querry, Appl. Opt. 24, 4493 (1985).

## Chapter 5

# CO ADSORPTION SITE OCCUPATION ON Pt(335): A QUANTITATIVE INVESTIGATION USING TPD AND EELS

### I. Introduction

The material presented in this chapter is based largely on our paper published in *Surface Science* [1].

To understand the effects of defect sites in heterogeneous catalysis, CO has been studied on stepped Pt surfaces [2,3,4]. Models for CO adsorption on the stepped Pt(335) [5] and Pt(112) surfaces have been proposed. These models assume that all the CO is adsorbed at atop sites. However, our preliminary electron energy loss spectroscopy (EELS) of CO on Pt(335) showed substantial bridge site occupation at all but the lowest coverages [6]; it is likely that CO also occupies bridge sites on the similar (112) surface. In this chapter, we present a quantitative analysis of new EELS and temperature programmed desorption (TPD) data, which together with plausible structure assumptions leads to a new model for CO adsorption on Pt(335). Because there is no direct structural information, our model is still speculative, but it does indicate major tendencies.

The Pt(335) surface is stepped with (111) terraces four atoms wide separated by monatomic (100) steps. Previous studies [2,3] of CO on this surface found two distinct CO species, identified as edge and terrace CO, as shown in Figure 4-1 of Chapter 4. Only edge CO is present at low coverage. Both edge and terrace CO coexist at higher coverages.

A structural model consistent with reflection-absorption infrared spectroscopy (RAIRS) and TPD was proposed by Greenler et al. [5]. Since



bridge-bonded CO was not detected with RAIRS, it was assumed, by analogy with Pt(111), that all the CO is at atop sites and the saturation layer has a  $(\sqrt{3} \times \sqrt{3})R30^\circ$  structure as shown in Figure 5-1 [7,8]. (Even on Pt(111), however, the  $(\sqrt{3} \times \sqrt{3})R30^\circ$  structure includes both bridge-bonded and atop CO [9].) In this model, the saturation coverage is 1/4 ML, 1/3 of the edge sites are occupied, and the ratio of edge to terrace CO is 1:2.

The measured saturation coverage of CO on Pt(335) is higher than this model predicts. For the similar Pt(112) surface, which differs from Pt(335) only in that the terraces are three rather than four atoms wide, the CO saturation coverage is  $(1.00 \pm 0.07) \times 10^{15} \text{ cm}^{-2}$  [10]. Lambert and Tobin estimated the saturation CO coverage on Pt(335) by a TPD comparison with CO on Pt(112). They assumed the height of the high-temperature peak at saturation to be proportional to the step density, a factor 0.73 smaller on Pt(335) than on Pt(112). The estimated saturation CO coverage was  $(8.3 \pm 0.6) \times 10^{14} \text{ cm}^{-2}$ , which corresponds to  $0.63 \pm 0.05 \text{ ML}$  [2].

In a RAIRS study of CO on Pt(335), Hayden et al. [3] saw no absorption band in the  $1800\text{--}1900 \text{ cm}^{-1}$  range characteristic of bridge-bonded CO. The later RAIRS experiments of Lambert and Tobin *did not* examine that spectral range [2]. In an ESDIAD (electron stimulated desorption ion angular distributions, a technique that measures orientation of adsorbed molecules) study of CO on Pt(112), Henderson et al. [4] did not observe the elliptical pattern expected for bridge species (although they later found that their detection method was actually not sensitive to bridge CO [11], their conclusion was not changed as indicated in their recent paper [12]). A total energy calculation in the dilute limit also predicted that bridge sites would not be occupied on Pt(112) [13]. All previous models have therefore considered only atop CO [2,4,5], even though CO at bridge sites on the flat Pt(111) surface is well documented [7,9,14].

Preliminary EELS results for the (335) surface clearly show CO at bridge sites at all but the lowest coverages and substantial bridge site occupation both on the edges and on the terraces [6]. Our observation of bridge CO species has been confirmed in RAIR spectra of CO on our Pt(335) crystal by Yates and his coworkers [11]. CO at bridge sites has also been observed on Pt(321) [15], a stepped surface that has three-atom-wide (111) terraces, and additionally on a stepped Pt surface with six-atom-wide (111) terraces [7]. There is currently no direct experimental evidence as to whether CO occupies bridge sites on Pt(112).

In this work, TPD and EEL spectra have been obtained as a function of CO coverage on Pt(335). A model for CO adsorption on Pt(335) is proposed that incorporates all available information. TPD is used to determine absolute edge and terrace populations, based on the saturation CO coverage determined by Lambert and Tobin [2]. EELS is used to obtain the relative concentrations of bridge and atop CO. The EELS analysis requires crucial assumptions regarding the EELS cross sections of the various CO species. Both Lambert and Tobin [2] and Reutt-Robey et al. [16] found no difference in the IR cross sections of atop CO on the edge and on the terrace; we assume that the same is true of the EELS cross sections, at all coverages. For CO on Pt(111), Mieher et al. determined that the EELS cross section of atop CO is greater than that of bridge CO by a factor of 1.8 at all coverages [14]. Lacking other information, we use this cross section ratio for both edge and terrace CO on Pt(335), at all coverages.

We use the edge and terrace coverages, and the bridge/atop ratio, together with plausible assumptions, to estimate the populations of the four CO species (edge atop, edge bridge, terrace atop, and terrace bridge) as a function of coverage. At selected coverages, possible structures are proposed, but we emphasize that we have no direct evidence for these structures. Finally, we

compare and contrast our results with those of Henderson et al. for CO on Pt(112) [4].

## II. Experimental

Details of the EELS apparatus, sample preparation, and coverage determination are given in Chapter 2. CO was adsorbed with the sample at 100 K. At coverages below 0.3 ML, annealing has no perceptible effect on the vibrational spectrum. At higher coverages, as we discuss later, annealing did irreversibly change the vibrational spectrum. Hence, for the data used in developing our model, the overlayer was annealed by heating to 280 K for 10 s and then cooled to 100 K. No increase in CO partial pressure could be detected during annealing; 280 K is below the temperature where CO desorbs even at saturation coverage, but much above the temperature ( $\approx 160$  K) where CO is mobile [17].

## III. Results

In the following discussion,  $\theta$  is total CO coverage in ML, where 1 ML corresponds to one CO per surface Pt atom.  $\theta_e$  and  $\theta_t$  are the coverages of edge and terrace CO in ML.  $I_{b/a}$  is the EELS intensity ratio of bridge to atop CO; we assume  $\theta_b/\theta_a = 18I_{b/a}$  (Note that  $I_{a,b}$  is defined as the EELS intensity of atop-bridge double loss in Chapter 4).

### III-1. TPD

The TPD spectra shown in Figure 5-2a indicate that at least two CO species are present on Pt(335). It has been shown that the high-temperature peak in TPD data of CO on stepped Pt is associated with steps [7,18,19]. We thus

assume that the high-temperature peak on Pt(335) is due entirely to edge CO [2,3]. This assumption is discussed in section 6.1. To determine the relative weight in each peak, and thus the edge and terrace coverages, we fit the TPD data to Equation (38) of Chapter 2 [20], assuming that both species follow first order kinetics. To determine absolute coverages, we use Lambert and Tobin's measurement at saturation of  $\theta = 0.63 \pm 0.05$  ML [2]. The resulting experimental values of edge and terrace coverages are shown as points in Figure 5-3a.

An example of the fit is shown in Figure 5-2b. The "tail" at high temperature is not fit well. The discrepancy does not appear to be caused either by a low pumping speed or by surface defects; the tail was not seen with the same sample mounted in two other chambers. In determining surface coverages, the high-temperature tail is assumed to be a background desorption artifact and is ignored.

The TPD data were also used to estimate activation energies and pre-exponential factors for CO desorption from edge and terrace sites, although these quantities are not necessary for our model. For edge CO, the desorption activation energy  $E_d$  is about 32.0 kcal/mole at low coverage, 28.5 kcal/mole at saturation, and the pre-exponential factor is about  $3 \times 10^{12} \text{ s}^{-1}$  independent of coverage.

The TPD data we observe are consistent with previous TPD studies of CO desorption from Pt(111) and stepped surfaces. On a stepped surface, when allowance is made for heating rate, the temperature of the CO desorption peak from the (111) terrace matches the peak from CO on Pt(111). However, TPD is not the most reliable way to determine  $E_d$  [21]. For CO on Pt(111), for example, two TPD studies [10,18] estimated the limiting  $E_d$  at low CO coverage as 29.6 and 27 kcal/mole. Three other studies that used work function data [22], thermal

He scattering [23], and laser-induced thermal desorption [24] all found that  $E_d$  in the low coverage limit is 32 kcal/mole. The work function study of Norton et al. [25] provided direct evidence that CO on Pt(111) is not in thermal equilibrium during TPD.

On stepped Pt surfaces, most of the available information about  $E_d$  is from TPD. In a TPD study of CO on Pt(112), in step-terrace notation Pt(S)-[3(111)×(100)], McCabe and Schmidt [10] found that  $E_d$  was in the range of 22.5 to 28.5 kcal/mole. On the same surface, Siddiqui et al. [26] used TPD data to estimate that  $E_d$  is 8 kcal/mole larger for CO on the step edge than for CO on the terrace. In a TPD study of CO on Pt(S)-[3(111)×(31 $\bar{1}$ )], McClellan et al. [15] found that  $E_d$  = 36 kcal/mole for CO at edge sites and 23 kcal/mole for CO on the terrace. For CO on Pt(S)-[6(111)×(100)], Collins and Spicer [18] used TPD to estimate that  $E_d$  for CO at the step edge is 33 kcal/mole and that  $E_d$  for CO on the (111) terrace is in the range of 24 to 27 kcal/mole. They obtained the same respective values of  $E_d$  for CO at the step and terrace sites on Pt(S)-[6(111)×(111)]. Also, in an IR study of CO on Pt(S)-[29(111)×(1 $\bar{1}$ 01)] that did not rely on TPD, Reutt-Robey et al. [27] found that CO is about 8 kcal/mole more tightly bound at step sites than it is at terrace sites.

### III-2. EELS

We observed both bridge and atop CO on Pt(335), as in our previous EELS study [6]. The spectra for CO adsorbed at 100 K and annealed at 280 K are shown in Figure 5-4. The ratio  $I_{b/a}$  is plotted as a function of coverage in Figure 5-3b (hollow circle). At the most dilute coverages ( $\theta \leq 0.05$ ), only edge CO is observed with TPD and only atop CO with EELS, so the only species present is edge atop. Bridge CO is seen in the EEL spectra for all  $\theta \geq 0.05$  ML. Initially,

between  $\theta = 0.05$  and  $\approx 0.15$ , bridge CO is seen only on edge sites, since TPD shows only edge CO. As the coverage increases ( $\theta \geq 0.15$ ) and edge and terrace CO begin to coexist, the EELS intensity of bridge CO relative to that of atop CO diminishes. The maximum  $I_{ba}$  is about 0.42 and occurs at  $\theta = 0.14$ . At high coverage,  $I_{ba}$  decreases to about 0.2. The observed  $I_{ba}$  implies that the ratio  $\theta_b/\theta_a$  of bridge to atop coverages rises to a maximum of 0.76 and then falls to 0.36 as  $\theta$  continues to increase (based on a constant ratio 1 : 1.8 of bridge to atop EELS cross section).

It is interesting that edge bridge sites are occupied in the  $\theta = 0.05$  to 0.14 ML range, before occupation of terrace atop sites begins, since generally atop sites are energetically favored over bridge sites. In addition, the total energy calculation [13] of Pancir et al. for CO on Pt(112) suggests that, in the limit of very dilute coverage, adsorption at atop sites on the terrace is favored over bridge sites on the edge. A strong attractive potential at the edge could explain why less energy is needed to "squeeze" bridge CO onto edge sites, rather than adsorb on empty terrace sites.

The effect of annealing the adsorbed layer to 280 K is also shown in Figure 5-3b. Annealing decreases  $I_{ba}$  at higher coverage, but has no effect on  $I_{ba}$  at low coverage. This effect is discussed in section 6.2.

#### IV. Model and Analysis of Site Occupation

We wish to determine the individual coverage of four CO species as a function of total CO coverage: edge atop, edge bridge, terrace atop, and terrace bridge. The TPD and EELS data provide three numbers at each coverage studied:  $\theta_e$ ,  $\theta_t$ , and  $\theta_b/\theta_a$ . Three numbers are insufficient to determine four unknowns. We therefore introduce supplementary constraints motivated by

trends in the data, structural considerations, and analogy with Pt(111). The need for such assumptions could be eliminated by additional data. For example, Henderson et al. observed ordered CO structures on Pt(112) using digital LEED [4]; none of the studies of CO on Pt(335), however, has observed such structures [2,3]. IR spectroscopy could also provide more detailed information, but the interpretation of the spectra is complicated by strong dipole coupling [2,3].

#### IV-1. Very low coverage ( $\theta \leq 0.12$ )

Because only edge CO is present ( $\theta \approx 0$ ), the TPD and EELS data uniquely determine the edge bridge and edge atop populations. At very dilute coverage, there is only edge atop CO, consistent with theoretical predictions for CO on Pt(112) [13]. The coverage of edge atop CO versus  $\theta$  flattens out soon after edge bridge CO is seen at  $\theta \geq 0.05$ . However,  $I_{ba}$  increases sharply, indicating that the population of edge bridge CO increases quickly with  $\theta$ . At  $\theta = 0.14$ ,  $I_{ba}$  reaches a maximum and the populations of edge atop and edge bridge CO are comparable ( $\theta_b/\theta_a \approx 1.8 \times 0.42 = 0.76$ ).

#### IV-2. Low coverage ( $0.12 < \theta \leq 0.22$ )

In this coverage region, the TPD data show that terrace CO appears and increases rapidly, while edge CO grows slowly, reaching a plateau at  $\theta = 0.22$ . At the same time,  $I_{ba}$  drops, indicating that most terrace adsorption occurs at atop sites, consistent with a structure in which 2/3 of the edge sites are occupied ( $\theta_e = 0.17$ ) with equal populations of edge bridge and edge atop CO, as shown in Figure 5-5a. The remaining 0.05 ML is then on terrace atop sites. Based on the observation of Poelsema et al. that defect sites on Pt(111) nucleate island formation [17], and the strong tilting of edge CO on Pt(112) observed at

comparable coverages by Henderson et al. [4], we suggest that the terrace CO occupies sites adjacent to the step edges, as shown in Figure 5-5c. (Similar suggestions have been made by Greenler et al. [5] and by Henderson et al. [4].)

#### IV-3. Intermediate coverage ( $0.22 < \theta \leq 0.42$ )

In this range, the TPD data show that edge coverage remains fixed at  $2/3$  of site occupation ( $\theta_e = 0.17$ ). We therefore assume that the edge CO structure of Figure 5-5a remains unchanged. The decrease of  $I_{ba}$  with  $\theta$  up to  $\theta \approx 0.42$  indicates that the adsorption occurs predominantly on terrace atop sites. For simplicity, we assume that all the adsorption in this range occurs on atop sites. At  $\theta \approx 0.42$ , the model gives  $\theta_t = 0.25$  ( $1/3$  of terrace sites filled) with only atop CO on the terraces. An ordered ( $3 \times n$ ) structure with these characteristics is shown in Figure 5-5b.

The model does not agree perfectly with the data. The observed  $I_{ba}$  in Figure 5-3b has a plateau between  $\theta = 0.2$  and  $0.3$ . At  $\theta \geq 0.42$ , the observed  $I_{ba}$  is also slightly too large to give the constant  $\theta_b/\theta_a = 0.25$  predicted by the model. A good fit can be obtained by adding a finely tuned population of terrace bridge CO, amounting to  $0.03$  ML, or  $12\%$  of the total terrace population. It seems equally likely, however, that these discrepancies are caused by other effects, such as different tilt angles for bridge and atop CO or a change in the EELS cross section ratios.

#### IV-4. High coverage ( $\theta \geq 0.42$ )

At saturation coverage, the TPD data of Figure 5-3a show that  $\theta_e = 0.25$ , one CO molecule for every edge Pt atom. Such a dense structure with both atop and bridge CO is implausible. The observed  $I_{ba}$  rules out the possibility that all



the edge CO is in bridge sites; we therefore conclude that at saturation the edge has only atop CO. This is consistent with the tendency of compressed CO structures on Pt(111) to favor atop CO [28]. On the average, then, each CO added to the edge must occupy an atop site and displace an existing bridge CO to an adjacent atop site, as shown schematically in Figure 5-6. We assume that this process occurs at a constant rate between  $\theta = 0.42$  and saturation, as shown in Figure 5-3c.

Once this assumption is made, the other coverages are fixed by the fact that both the edge-to-terrace and bridge-to-atop ratios are constant. The population of terrace atop CO remains constant at 0.25 ML (1/3 of terrace sites) while the population of terrace bridge CO increases linearly to 0.13 ML (1/6 of terrace sites). If we allow a small amount of terrace bridge CO in the 0.25-0.40 coverage range, and adjust the terrace atop population accordingly, we can greatly improve the fit. At most, the terrace bridge population reaches 0.03 ML in the  $0.25 < \theta < 0.40$  range.

At saturation, all edge sites are occupied with atop CO and 50% of terrace sites are occupied with a 2 : 1 atop-to-bridge ratio on the terrace. Figures. 5-5d and 5-5e show two such structures. Both are  $(2 \times n)$ . The structure in Figure 5-5d is most likely to show the strong tilting of edge CO observed by Henderson et al. on Pt(112) [4].

The trend in terrace site occupation versus coverage for CO on Pt(335) shown in Figure 5-3c is similar to those for CO on Pt(111) shown in Figure 5-7, obtained by Mieher et al. [14]. Atop CO adsorbs first. Bridge CO starts to adsorb after the atop CO coverage reaches a plateau and continues to increase up to saturation.

## V. Discussion

### V-1. Comparison between Pt(335) and Pt(112)

Our observations of CO on Pt(335) can be compared with an ESDIAD study of CO on Pt(112) by Henderson et al. [14]. In discussing Pt(112) ESDIAD patterns, CO oriented along (112) is said to be untilted, CO tilted away from (112) toward (111) is tilted "upstairs", and CO tilted from (112) away from (111) is tilted "downstairs", as illustrated in Figure 5-8. Henderson et al. assumed that CO tilted downstairs was edge CO, while CO tilted upstairs was terrace CO. This assumption led to an unconventional interpretation of their TPD data. At  $\theta \approx 0.25$ , a clear low-temperature peak was observed in TPD, but upstairs-tilted CO was not seen with ESDIAD. They concluded, in contrast to this and other work [2,3,10,15,18], that some edge CO, as well as terrace CO, desorbed in the low temperature peak [4,26]. Such an effect could arise either from a discontinuous reduction of the binding energy of edge CO at high edge coverage or from net migration of CO from edge to vacant terrace sites during TPD.

We do not believe that edge CO contributes to the low temperature TPD peak from the (335) surface. First, enough CO desorbs in the high-temperature peak to occupy all of the edge sites; if the low-temperature peak contained additional edge CO the edge site occupation would be greater than 100%, which we regard as implausible. Second, partial desorption experiments, in which the temperature ramp was stopped during or after the low-temperature peak, showed no evidence for net edge-to-terrace migration, even at the highest coverages. Finally, the data of Hayden et al. for CO on Pt(335) show that the low-temperature TPD peak and the high-frequency IR absorption peak associated with terrace atop CO appear simultaneously, at a coverage of 30-35% of saturation or  $\theta = 0.19 - 0.22$  [3].

It is true that there is rapid exchange of CO between edge and terrace sites. In one isotope labeling experiment [26], the exchange was fast enough to mix the isotope ratio in the edge and terrace populations to equilibrium in 10 s at 300 K. It has also been suggested [29] that desorption from the edge generally involves an intermediate step of first moving to the terrace. Neither effect, however, necessarily affects the interpretation of TPD spectra.

We suggest that many of the ESDIAD results obtained for CO on Pt(112) may also apply to CO on Pt(335), especially at low coverage where only edge sites are occupied, since the surfaces differ only in terrace width. Because the edge-edge distance on both surfaces is longer than the nearest neighbor distance of CO on Pt(111) in the  $(\sqrt{3} \times \sqrt{3})R30^\circ$  structure, Henderson et al. argue that spatial correlations between edges can be neglected at low coverage [4]. Conversely, the observation of bridge CO at edge sites on Pt(335) suggests that there may be bridge CO on Pt(112). The structures proposed by Henderson et al. do not include bridge CO [4].

For CO on Pt(112), Henderson et al. reported a  $(2 \times n)$  LEED pattern when  $\theta = 0.19$  or about 50% of edge sites are occupied. On Pt(335), we start to observe bridge CO when only 20% of edge sites are occupied. When 50% of the edge sites are occupied, the populations of bridge and atop CO are equal. It is not possible to construct a plausible  $(2 \times n)$  structure containing equal numbers of atop and bridge CO. Our proposed structure with 2/3 of the edge sites occupied is  $(3 \times n)$ , as shown in Figure 5-5a, but we did not observe an ordered LEED pattern.

At  $\theta = 0.19$ , Henderson et al. observed tilting downstairs from (112), with no tilting along the edge direction. Our model predicts a similar situation for CO on Pt(335) at  $\theta \approx 0.12$ , with 50% of edge sites and no terrace sites occupied. At  $\theta = 0.24$ , Henderson et al. observed three CO orientations, all tilted  $20^\circ$

downstairs relative to (112), but tilted by  $-13^\circ$ ,  $0^\circ$ , and  $+13^\circ$  along the step edge. Since no upstairs tilted CO was seen, they concluded that no terrace CO was present, even though TPD showed a clear low-temperature peak. No LEED pattern was observed; they proposed a structure with 75% edge site occupation [4]. In contrast, in our model, terrace CO is present on Pt(335) at all  $\theta > 0.12$ . At  $\theta \approx 0.22$ , we would expect ESDIAD of the edge CO to show a pattern qualitatively similar to the broad pattern observed on Pt(112), due to the influence of CO adsorbed on terrace sites adjacent to the edge (see Figure 5-5c). Possibly, terrace CO was present on Pt(112) but was not observed with ESDIAD. It is notable that for CO on Pt(335), terrace CO begins to be seen at these coverages in the RAIR spectra of Hayden et al. [3].

At higher coverages, terrace site occupation becomes significant on both surfaces, so overlayer structures on the (112) and (335) surfaces are likely to be different. Even so, our structural models have  $(3 \times n)$  periodicity at  $\theta \approx 0.42$  and  $(2 \times n)$  periodicity at saturation, similar to the LEED patterns observed on Pt(112):  $(3 \times 1)$  at  $\theta = 0.46$  and  $(2 \times 1)$  at saturation [4].

Since Henderson et al. observed that CO tilted as much as  $38^\circ$  from the average surface normal in their experiments on Pt(112) [4], it is necessary to consider the effect such tilts could have on our interpretation of EELS intensities (although an EXAFS study of CO on Pt(335) concluded that any tilting was much less extreme [30]). Within the dipole approximation, the cross section of a molecule tilted by angle  $\phi$  is reduced by a factor of  $\cos^2 \phi$ , or 0.88 for  $\phi = 20^\circ$  and 0.62 for  $\phi = 38^\circ$ . This could affect our experiment in two ways. First, if  $\phi$  of atop and bridge CO are radically different, either on the edge or on the terrace, our assumption of a fixed 1 : 1.8 cross section ratio is incorrect. A large difference in  $\phi$  is unlikely, however. Second, if edge CO is tilted more than terrace CO, then it contributes less EELS signal than we assume, and our

interpretation of  $I_{ba}$  is inaccurate. On Pt(112), a large difference in  $\phi$  is seen only at the highest coverage; at edge sites, half of the CO is tilted  $38^\circ$  downstairs, the remaining edge CO is oriented nearly along (112), and the terrace CO is tilted  $13^\circ$  [4]. We have modeled both the intermediate coverage and high coverage structures and find that such tilts change  $I_{ba}$  by less than 10%.

Another difference between our results for Pt(335) and those of Henderson et al. for Pt(112) is that several attempts to observe an ordered overlayer pattern with LEED, both at 100 K and after annealing up to the desorption temperature, were unsuccessful even though the clean surface gave clearly defined substrate spots. The explanation may be technical; the digital LEED used by Henderson et al. is far more sensitive to weak spots on a diffuse background than is the visual LEED that we used. As Henzler has shown [31], point defects such as kinks increase the background brightness and reduce the sharpness of the diffraction spots.

## V-2. Effect of Annealing

Our EELS data for CO on Pt(335), shown in Figure 5-3b, indicate that with  $\theta > 0.4$ , annealing the overlayer to 280 K transfers population irreversibly from bridge to atop sites; the effect is not observed at low coverages. Hayden et al. [3] also observed that annealing irreversibly changed the vibrational spectrum of CO on Pt(335), while for CO on Pt(111), Mieher et al. observed reversible site exchange between bridge and atop CO as a function of temperature [14]. The site-to-site hopping rate of CO on Pt(111) terraces increases by five orders of magnitude between 105 and 195 K [16], so it is not surprising that the layer does not reach equilibrium within minutes at 100 K. It is interesting that the effect of annealing depends on coverage.

At low coverage, below  $\theta = 0.3$ , annealing has no observed effect, indicating that bridge-atop equilibration occurs within a few minutes even at 100 K. We cannot prove with EELS that edge-terrace equilibration also occurs, but substantial movement of CO from terrace to edge would probably affect the bridge-to-atop ratio, especially at coverages near  $\theta = 0.1$ , where added edge CO increases the population on bridge sites, while on the terrace only atop sites are occupied. It appears that with  $\theta < 0.3$ , the overlayer is fully equilibrated within a few minutes at 100 K. In our model of the adsorption process, some rearrangement is needed to reach the edge structure shown in Figure 5-5a. Apparently the barrier to motion along the edge is low enough to allow this to happen. The CO that adsorbs on the terrace is also able to migrate the few sites needed to reach the edge.

At  $\theta > 0.14$ , adsorption occurs both at terrace bridge and at edge atop sites, and annealing has a dramatic effect. The barrier to equilibration is greater. We believe the barrier is associated with the rearrangement involved in adding CO at the edge, as shown in Figure 5-6. Each new CO at the edge goes to an atop site and displaces a bridge CO to an adjacent atop site. The increase of two atop molecules and loss of one bridge molecule affects the bridge-to-atop ratio. The activation energy of a complicated two-molecule process like this one is likely to be larger than that of a simple one-molecule process. This explains the inability to reach equilibrium at 100 K with  $\theta > 0.4$ .

## VI. Summary

There are four CO species on Pt(335): edge atop, edge bridge, terrace atop, and terrace bridge. We have proposed a model for the populations of these species as a function of CO coverage that explains our TPD and EELS data. The interpretation of the EELS data is sensitive to certain assumptions. The model should therefore be taken only as indicative of general trends.

These trends are as follows: At low coverage, edge sites are favored, with edge atop sites filling first, followed by edge bridge sites. The edge structure is stabilized when 2/3 of the edge sites are filled, with roughly equal concentrations of bridge and atop CO. As terrace sites then begin to fill, terrace CO adsorbs preferentially on atop sites until 1/3 of the terrace sites are filled. Subsequent terrace adsorption then occurs on bridge sites. Simultaneously, CO adsorbs on edge atop sites, displacing the existing edge bridge CO. At saturation, the edge is fully saturated with atop CO, 1/2 of the terrace sites are occupied, and the ratio of atop to bridge CO on the terrace is 2 : 1. The activation barrier to equilibrium is greater at  $\theta > 0.4$  than at  $\theta < 0.3$ . For  $\theta < 0.3$ , equilibrium is reached within a few minutes at 100 K. For  $\theta > 0.4$ , annealing to 280 K allows the overlayer to reach an equilibrium state.

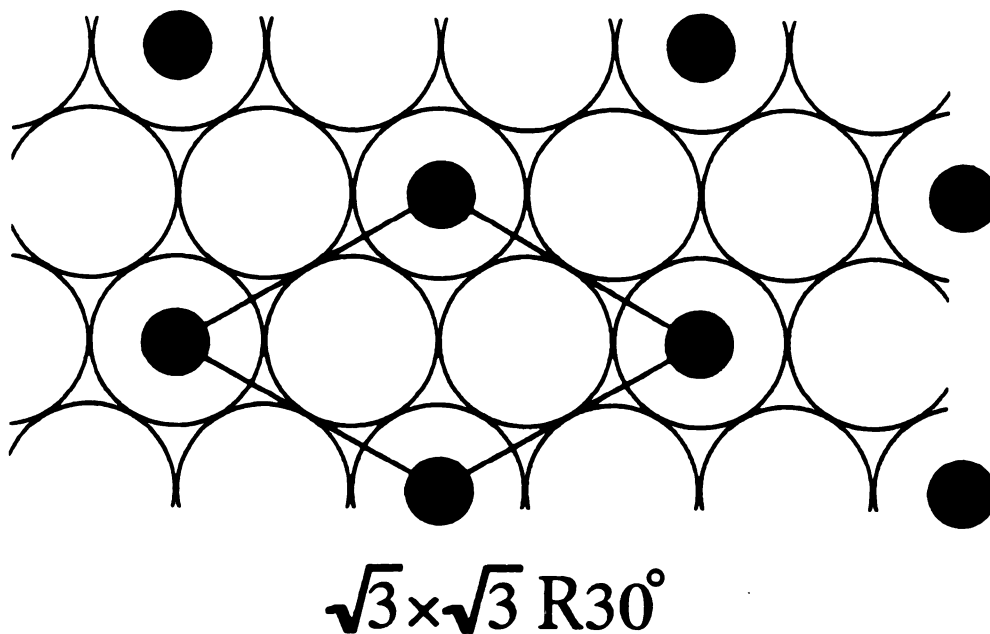


Figure 5-1. Proposed geometrical ( $\sqrt{3} \times \sqrt{3}$ )  $R30^\circ$  structure of CO on the (111) surface.



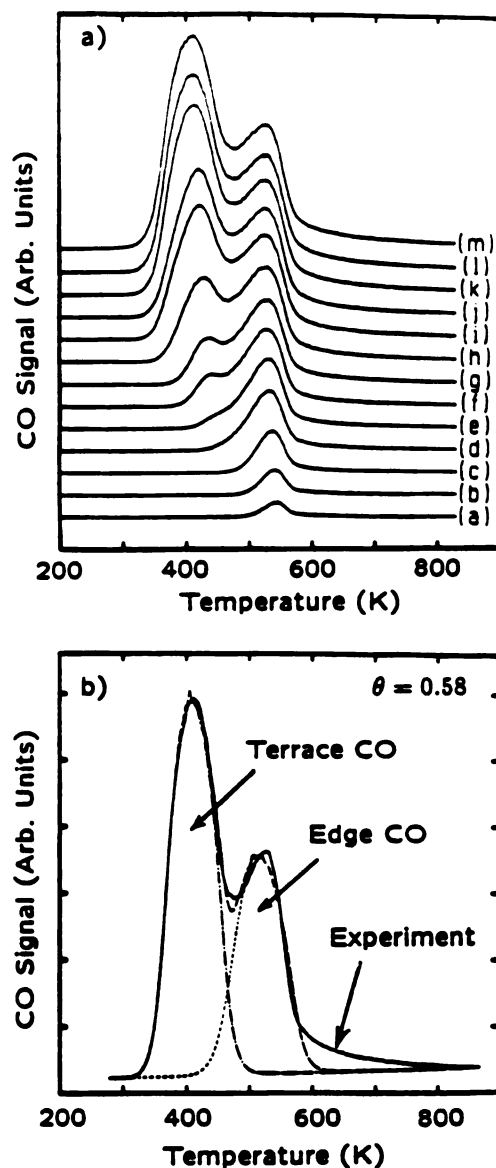


Figure 5-2. (a) TPD spectra of CO on Pt(335) at various coverages. The overlayer was annealed to 280 K and cooled to 100 K before desorption. The individual spectra have CO coverages of (a) 0.015, (b) 0.026, (c) 0.053, (d) 0.10, (e) 0.13, (f) 0.17, (g) 0.21, (h) 0.30, (i) 0.42, (j) 0.46, (k) 0.56, (l) 0.58, and (m) 0.63 ML. (b) Typical two-component fit to the TPD data, at  $\theta = 0.58$  ML.

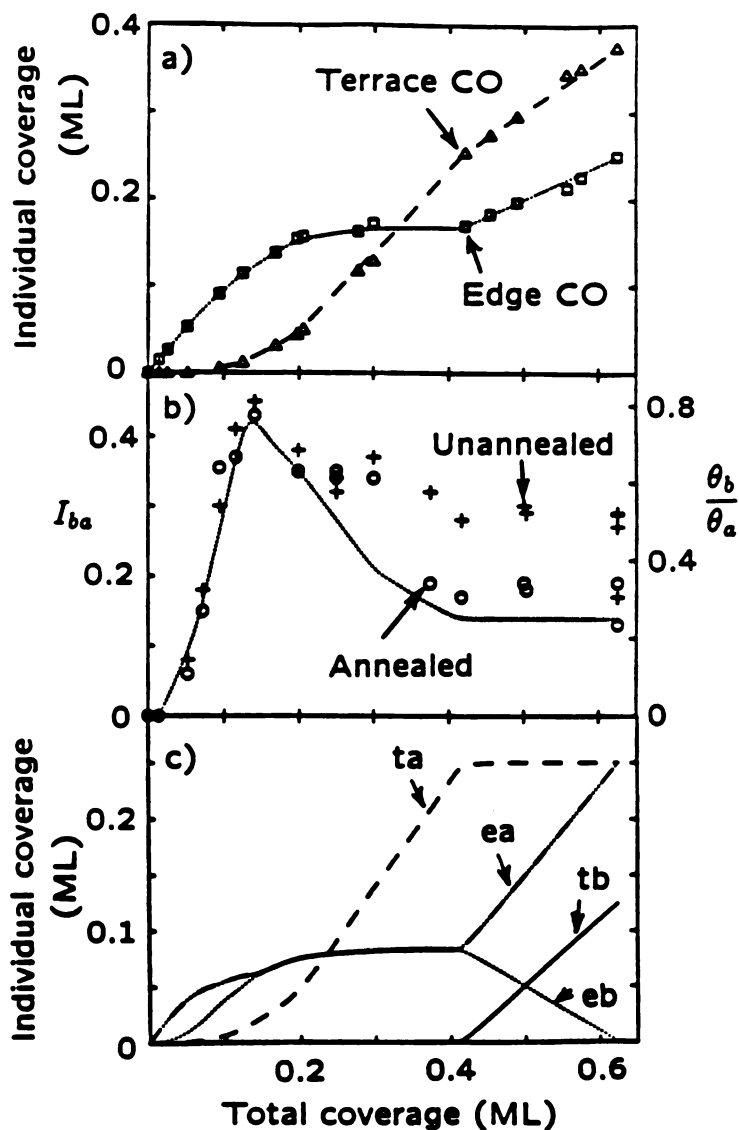


Figure 5-3. (a) Points are coverages of edge and terrace CO as determined from the TPD data. The lines are from our model. (b) Ratio  $I_{ba}$  of atop to bridge EELS intensity versus total CO coverage. The right axis shows the corresponding population ratio  $\theta_b/\theta_a$ . Crosses were measured after annealing; open circles were measured after annealing to 280 K. The line is from our model. (c) Model's population of the four CO species versus total CO coverage; ta = terrace atop; ea = edge atop; tb = terrace bridge; eb = edge bridge.

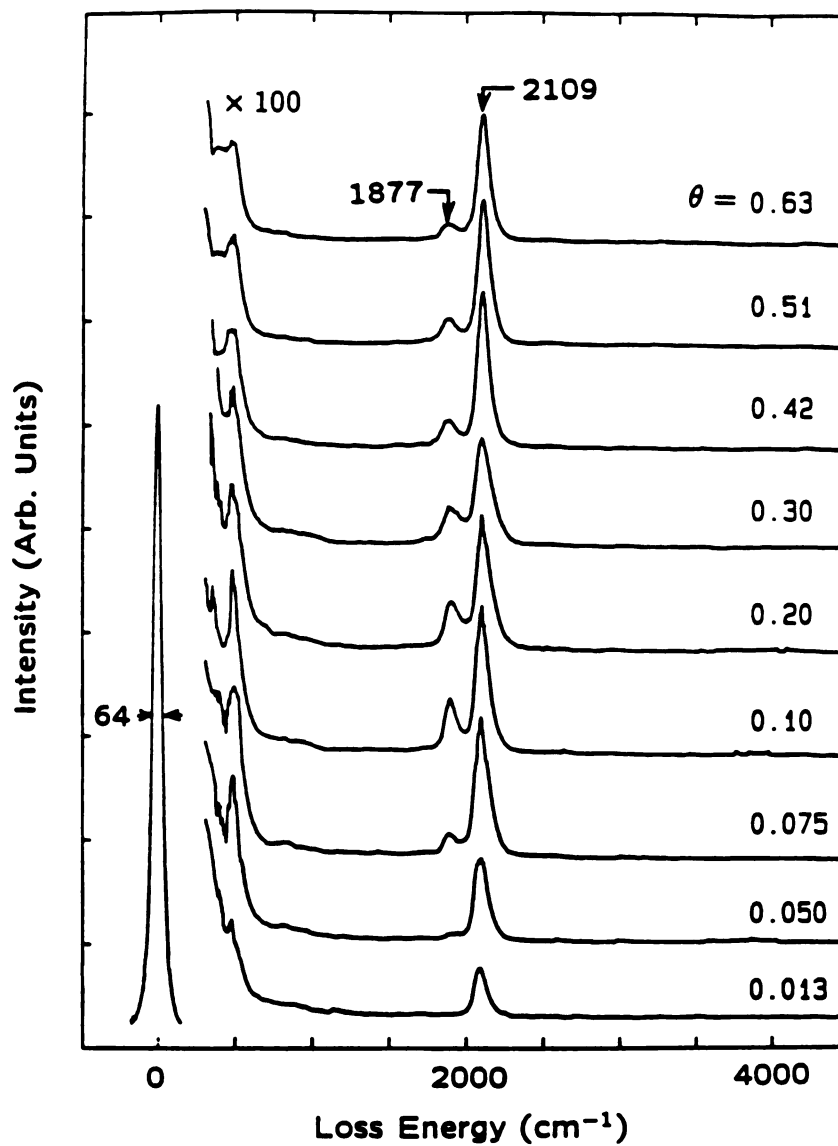


Figure 5-4. EELS spectra of CO on Pt(335) versus coverage. The sample was annealed to 280 K after dosing, then cooled to 100 K before the measurement.

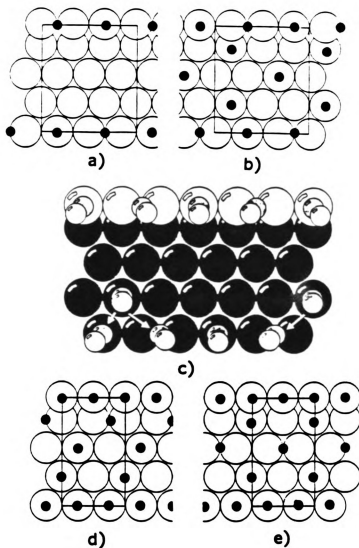
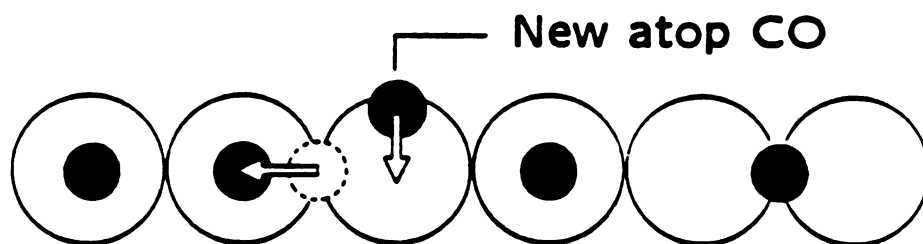


Figure 5-5. Possible structures of CO on Pt(335). (a) Edge structure with 2/3 of edge sites filled. (b) Proposed structure at  $\theta = 0.42$ . (c) Proposed structure at  $\theta = 0.22$ , showing partial occupation of terrace sites adjacent to the edge and possible tilting of edge CO. (d) Two possible structures at saturation ( $\theta = 0.63$ ).



**Figure 5-6. Sketch showing the addition of an atop molecule to the edge, accompanied by the displacement of one bridge CO to an adjacent atop site. Each additional molecule adds two atop COs and removes one bridge CO.**

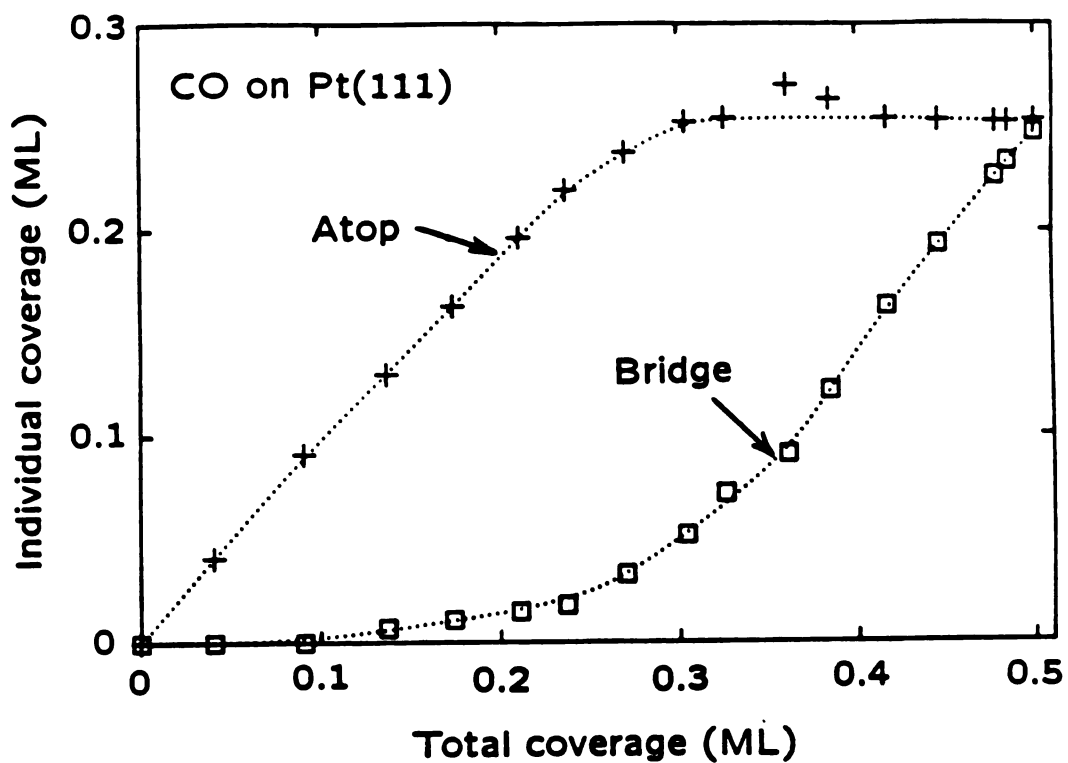


Figure 5-7. Coverages of bridge and atop CO on Pt(111) versus total CO coverage, from ref. [14]. The lines are guides to the eye.

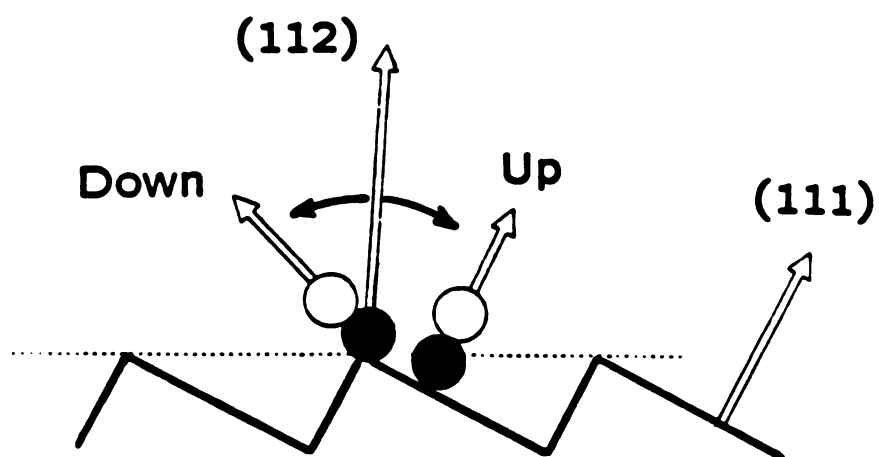


Figure 5-8. Sketch to illustrate the tilting of CO on Pt(112). Adapted from ref. [4].

**References**

1. J.S. Luo, R.G. Tobin, D.K. Lambert, G.B. Fisher and C.L. DiMaggio, *Surf. Sci.* 274, 53 (1992).
2. D.K. Lambert and R.G. Tobin, *Surf. Sci.* 232, 149 (1990).
3. B.E. Hayden, K. Kretzschmar, A.M. Bradshaw and R.G. Greenler, *Surf. Sci.* 149, 394 (1985).
4. M.A. Henderson, A. Szabo and J.T. Yates, Jr., *J. Chem. Phys.* 91, 7245 (1989).
5. R.G. Greenler, F.M. Leibsle and R.S. Sorbello, *Phys. Rev. B* 32, 8431 (1985).
6. J.S. Luo, R.G. Tobin, D.K. Lambert, F.T. Wagner and T.E. Moylan, *J. Electron Spectrosc. Relat. Phenom.* 54/55, 469 (1990).
7. H. Hopster and H. Ibach, *Surf. Sci.* 77, 109 (1978).
8. J.P. Biberian and M.A. Van Hove, *Surf. Sci.* 138, 361 (1984).
9. H. Steininger, S. Lehwald and H. Ibach, *Surf. Sci.* 123, 264 (1982).
10. R.W. McCabe and L.D. Schmidt, *Surf. Sci.* 66, 101 (1977).
11. J.T. Yates, Jr., Private communication (1992).
12. M.A. Henderson and J.T. Yates, Jr., *Surf. Sci.* 268, 189 (1992).
13. J. Pancir, I. Haslingerova and P. Nachtigall, *Chem. Phys.* 91, 3228 (1988).
14. W.D. Mieher, L.J. Whitman and W. Ho, *J. Chem. Phys.* 91, 3228 (1989).
15. M.R. McClellan, J.L. Gland and F.R. McFeeley, *Surf. Sci.* 112, 63 (1981).
16. J.E. Reutt-Robey, D.J. Doren, Y.J. Chabal and S.B. Christman, *J. Chem. Phys.* 93, 9113 (1990).
17. B. Poelsema, L.K. Verheij and G. Comsa, *Phys. Rev. Lett.* 49, 1731 (1982).
18. D.M. Collins and W.E. Spicer, *Surf. Sci.* 69, 85 (1977).
19. F.P. Netzer and R.A. Wille, *Surf. Sci.* 74, 547 (1978).



20. C.-M. Chan and W.H. Weinberg, *Appl. Surf. Sci.* 1, 377 (1978).
21. A.M. deJong and J.W. Niemantsverdriet, *Surf. Sci.* 233, 355 (1990).
22. G. Ertl, M. Neumann and K.M. Streit, *Surf. Sci.* 64, 393 (1977).
23. B. Poelsema, R.L. Palmer and G. Comsa, *Surf. Sci.* 136, 1 (1984).
24. E.G. Seebauer, A.C.F. Kong and L.D. Schmidt, *Surf. Sci.* 176, 134 (1986).
25. P.R. Norton, J.W. Goodale and E.B. Selkirk, *Surf. Sci.* 83, 189 (1979).
26. H.R. Siddiqui, X. Guo, I. Chorkendorff and J.T. Yates, Jr., *Surf. Sci.* 191, L813 (1987).
27. J.E. Reutt-Robey, D.J. Doren, Y.J. Chabal and S.B. Christman, *Phys. Rev. Lett.* 61, 2778 (1988).
28. B.N.J. Persson, M. Tushaus and A.M. Bradshaw, *J. Chem. Phys.* 92, 5034 (1990).
29. J.A. Serri, J.C. Tully and M.J. Cardillo, *J. Chem. Phys.* 79, 1530 (1983).
30. J.S. Somers, T. Lindner, M. Surman, A.M. Bradshaw, G.P. Williams, C.F. McConville and D.P. Woodruff, *Surf. Sci.* 183, 576 (1987).
31. M. Henzler, *Appl. Surf. Sci.* 11/12, 450 (1982).

**CHAPTER 6**  
**ELECTRIC FIELD SCREENING IN AN ADSORBED LAYER:**  
**CO ON Pt(111)**

**I. Introduction**

In this chapter, we present important measurements of CO on Pt(111). We then compare the measured Stark tuning rate for CO on Pt(111) with that for edge CO and terrace CO on Pt(335) [1]. Our data indicate that the Stark tuning rate of terrace CO is significantly suppressed and not that the Stark tuning rate of edge CO is significantly enhanced.

The conclusion in Chapter 4 suggests that the observed difference between the Stark tuning rates of the two CO species on Pt(335) results from different screening of the IR and DC fields; the physical mechanism is suggested. Surprisingly, we observed another example of such a difference in CO on Pt(111). The presently adopted physical picture of electric field screening at surfaces cannot explain the observed data.

A conceptual model that is widely used to explain infrared (IR) vibrational spectra of adsorbates on metal surfaces provides the physical picture of electric field screening at surfaces. The model assumes that the interaction between the IR electric field and the adsorbate is local. In this standard model, coverage-dependent effects are caused by dipole-dipole coupling [2,3,4,5,6,7,8]. Support for the model has come from isotope substitution experiments. Deviations from the standard model are explained as a chemical effect: as coverage changes, the individual molecules change. The standard model is generally presumed to be correct and is reviewed in section II.

In this chapter, we present material largely based on an experimental paper submitted to *Chemical Physics Letters* [9]. In the present experiment, CO on Pt(111) was studied as a function of CO coverage. Vibrational spectra were obtained with reflection absorption IR spectroscopy (RAIRS) and electroreflectance vibrational IR spectroscopy (EVS) [10]. A single tunable diode laser was used for both. The combination of RAIRS and EVS gives the Stark tuning rate and IR absorption cross section of CO, which are indicative of CO's response to the static and the IR electric field separately. In the standard model, coverage dependence comes from induced dipole fields that screen the applied electric field. The same screening is expected for CO responses to both static and IR fields. Our data indicate that the static and the IR screening depend differently on coverage. The standard model does not explain our data.

Our measurements were carried out in ultrahigh vacuum (UHV). Other researchers have measured the vibrational Stark effect of CO on Pt(111) electrodes in electrochemical cells [11,12,13,14,15,16,17]. A simple model would predict the same response to the local field in the two environments. Our data show that with CO on Pt(111) in UHV, at low CO coverage, the effect of applied electric field is only half that inferred from measurements in electrochemical cells. Such a direct comparison is made for the first time.

## **II. Dipole-Dipole Screening**

### **II-1 The Standard Model**

The dipole-dipole coupling model was originally proposed by Hamaker, Francis and Eischens [3]. The model has since been refined by Mahan and Lucas [4], Scheffler [5], and Persson and Ryberg [7]. The development of the model has been summarized well by Hollins and Pritchard

[8]. The dipole coupling model has been successful in explaining certain aspects of the vibrational spectra of adsorbates, but we will show in later sections that it fails to account for the difference we observe in the screening of the IR and electrostatic fields at CO's adsorption site.

In the remainder of this section, we intend to derive screening within the standard model for the IR cross section and the electrostatic field of a uniform adsorbed layer, of identical molecules.

In the standard model, many molecule systems are considered. The equation of motion can be written by treating adsorbates as point dipoles and coupled oscillators:

$$\mu \ddot{x}_i + (2\pi c \mu \Delta) \dot{x}_i + (4\pi^2 c^2 \mu) \nu_i^2 x_i = e^* (E_0 - \sum_{j \neq i} E_{dip}^{(j \rightarrow i)}). \quad (1)$$

We have included the vibrational damping term  $\Delta$  in Equation (1);  $\mu$  is the reduced mass of adsorbate,  $\nu_i$  is the singleton (intrinsic) frequency of adsorbate  $i$ ,  $e^*$  is the dynamic dipole moment of the adsorbate ( $e^*$  is the same as  $a_{11}$  used in previous chapters),  $E_0$  is the external applied field, and  $E_{dip}^{(j \rightarrow i)}$  is an induced dipole field from adsorbate  $j$  to adsorbate  $i$ . If consider every dipole moment as a harmonic oscillator where  $x_i \propto \exp(-i2\pi c \nu t)$ , in Equation (1) can be written as

$$4\pi^2 c^2 \mu (\nu_i^2 - \nu^2 - [i\nu\Delta]) x_i = e^* (E_0 - \sum_{j \neq i} E_{dip}^{(j \rightarrow i)}). \quad (2)$$

Similarly, the dipole field is

$$E_{dip}^{(j \rightarrow i)} = -P_j U_{ij} \quad (3)$$

$$\text{with } P_j = e^* x_j + \alpha_e (E_0 + \sum_{k \neq j} E_{dip}^{(k \rightarrow j)}). \quad (4)$$

Here,  $U_{ij}$  is dipole coupling between molecules  $i$  and  $j$ . For a point dipole well outside an ideal planar surface,  $U_{ij} \propto 1/x_{ij}^3$  [4,5,6]; where  $x_{ij}$  is the distance between molecules  $i$  and  $j$ , and the summation includes both real and image

dipoles. However, Persson and his co-workers [7,18] have pointed out that the distance from the center of the CO bond to its image is so small (about  $2 \text{ \AA}$ ) that a classical treatment of the image fields is unrealistic. Instead, self-image effects are incorporated into the values of  $e^*$  and  $\nu_i$ , and the coupling  $U_{ij}$  is determined by a fit to the data.

In Equations (3) and (4),  $P_j$  is the total dipole moment of adsorbate j, ( ) in second term in Equation (4) is the total electric field acting on adsorbate j, and  $\alpha_e$  is the electronic polarizability of adsorbate j. By rearranging Equation (2), we obtain

$$e^* x_i = \frac{(e^*)^2}{4\pi^2 c^2 \mu (\nu_i^2 - \nu^2 - [i\nu\Delta])} (E_0 - \sum_{j \neq i} E_{dip}^{(j \rightarrow i)})$$

$$= \frac{\alpha_e}{1 - (\nu/\nu_i)^2 - i(\nu\Delta/\nu_i^2)} (E_0 - \sum_{j \neq i} E_{dip}^{(j \rightarrow i)}) \quad (5)$$

$$\text{with } \alpha_e = (e^*)^2 / (4\pi^2 c^2 \mu \nu_i^2). \quad (6)$$

In Equation (6), the vibrational line shape for molecule i is approximated as Lorentzian at  $\nu \approx \nu_i$ . Here,  $\alpha_v$  is defined as vibrational polarizability of adsorbate i, and  $\Delta$  is correlated to the line width of the vibrational band. For CO on Pt(111), line width is usually about  $3\text{-}5 \text{ cm}^{-1}$ .

If we substitute dummy variables of  $j \rightarrow i$  and  $k \rightarrow j$  in Equation (4) and apply Equations (3) and (5) to it, we get

$$P_i = (\alpha_e + \frac{\alpha_v}{1 - (\nu/\nu_i)^2 - i(\nu\Delta/\nu_i^2)}) (E_0 - \sum_{j \neq i} U_{ij} P_j). \quad (7)$$

The second term in Equation (7) is usually called local field at site i, which can be expressed as

$$(E_{loc})_i = E_0 - \sum_{j \neq i} U_{ij} P_j = \gamma_i E_0 \quad (8)$$

where  $\gamma_i$  is a screening factor. The first term in Equation (7) is called polarizability of molecule i,  $\alpha_i(\nu)$ . Therefore, Equation (7) can be rewritten as

$$P_i = \alpha_i(\nu)(E_{loc})_i \quad (9)$$

$$\text{with } \alpha_i(\nu) = \alpha_e + \frac{\alpha_v}{1 - (\nu/\nu_i)^2 - i(\nu\Delta/\nu_i^2)}. \quad (10)$$

Note that we approximate Equation (10) as Lorentzian at  $\nu \approx \nu_i$ :  $(\nu\Delta/\nu_i^2) \approx \Delta/\nu_i$ .

The physical picture of this derivation can be viewed as follows: when simple molecules, such as CO, adsorb on a transition metal surface, electric dipole coupling between adsorbed molecules results in screening of an applied field. To be more specific, if we apply an external electric field  $E_0$  onto the surface, it induces a dipole moment  $P_i$  on adsorbate  $i$ . At the same time, the dipole moments of other adsorbates, induced by the same field, provide opposite fields to cancel partially the applied field as shown in Figure 6-1. If the applied field is small enough that only linear response needs to be considered, the local field at site  $i$  can then be obtained as indicated in Equation (8).

In the model,  $\alpha_e$  is treated as frequency independent. Applying Equation (9), the screening factor for an ordered layer of identical molecule species can be written as

$$\gamma = \frac{E_{loc}}{E_0} = \frac{1}{1 + \alpha\tilde{U}(0)} \quad (11)$$

where  $\tilde{U}(0) = \sum_{j \neq i} U_{ij}$ , the coverage-dependent dipole coupling parameter, and we replace  $\nu_i$  with  $\nu_0$  for all molecules being identical.

When the applied field has frequency different from resonance frequency,  $|1 - (\nu/\nu_0)^2| \gg (\nu\Delta/\nu_i^2)$ , the screening factor can be straightforwardly written as

$$\gamma = \frac{E_{loc}}{E_0} = \frac{1 - (\nu/\nu_0)^2}{[1 + \alpha_e\tilde{U}(0)][1 - (\nu/\nu_0)^2] + \alpha_v\tilde{U}(0)} \quad (12)$$

When the frequency of the applied electric field (IR field) is about the same as the resonant frequency, the screening of the applied field becomes quite complicated. We defined  $\gamma_R$  as the screening factor of the IR cross section instead of the screening factor of the IR field, so  $\gamma_R$  is directly measurable from RAIRS experiments. We state that the IR cross section is reduced by a factor of  $(\gamma_R)^2$  due to the dipole coupling effect. The derivation of  $\gamma_R$  is presented below.

The relationship between the applied field and the final dipole moment of an adsorbate in an ordered layer of identical molecules can be derived from Equation (9):

$$P = \alpha(\nu)(E_{loc}) = \tilde{\alpha}(\nu)E_0$$

$$\text{with } \tilde{\alpha} = \frac{\alpha(\nu)}{1 + \alpha(\nu)\tilde{U}(0)}. \quad (13)$$

As mentioned in the Chapter 2, reflectivity changes due to adsorbed molecules are measured in RAIRS. For the angle of incidence of an IR beam being  $85^\circ$ , as in our case and most of the cases, the change in reflectivity at near resonant frequency is, to good approximation [19],

$$\frac{\Delta R}{R} = -32\pi^2\nu \frac{\sin^2\phi}{\cos\phi}(\theta \times n_s)\text{Im}(\tilde{\alpha}). \quad (14)$$

Here,  $\alpha_0$  is defined in Equation (13) and  $\phi$  is the angle of incidence. Also,  $\theta$  is coverage of adsorbed molecules and  $n_s$  is the number of substrate atoms per  $\text{cm}^2$ . By performing the  $\text{Im}[\tilde{\alpha}]$  calculation in Equation (14) and assuming  $\Delta$  in Equation (10) to be infinitesimally small, equation (14) gives [7]

$$\frac{\Delta R}{R} \approx -8\pi\nu_0^2 \frac{\sin^2\phi}{\cos\phi}(\theta \times n_s) \frac{\alpha_\nu}{[1 + \alpha_\nu\tilde{U}(0)]^2} \delta(\nu - \nu^*) \quad (15)$$

$$\text{with } \nu^* = \nu_0 \sqrt{1 + \frac{\alpha_\nu\tilde{U}(0)}{1 + \alpha_\nu\tilde{U}(0)}} \quad (16)$$

Here,  $\nu^*$  is the observed vibrational frequency in RAIRS and  $\nu_0$  is the vibrational frequency at coverage  $\theta$  without dipole-dipole interaction between adsorbates;  $\nu_0$  is affected by the chemical effect only and is discussed in the next section. Using Equation (15), the (integrated) absorption cross section can be readily obtained:

$$I(\theta) = \int \frac{\Delta R}{R} d\nu \propto \nu_0^2 \theta \frac{\alpha_\nu}{[1 + \alpha_\nu \tilde{U}(0)]^2} \quad (17)$$

As stated in Equation (6),  $\alpha_\nu \propto (e^*)^2$ , so Equation (17) can also be expressed in terms of  $e^*$ :

$$I(\theta) \propto \nu_0^2 \theta (\gamma_R e^*)^2 \quad (18)$$

$$\text{with } \gamma_R = \frac{1}{1 + \alpha_\nu \tilde{U}(0)}. \quad (19)$$

Here,  $\gamma_R e^*$  is the screened dynamic dipole moment. In Equations (17) and (19),  $\tilde{U}(0)$  is related to the structure of the adsorbed layer, so is strongly coverage dependent. For CO on Ru [7],  $\alpha_\nu$  is approximately coverage independent. Although  $\nu_0$  is observed to be coverage dependent, the change due to coverage is less than 2%. The frequency shift in  $\nu_0$  is significant enough to be observable but is not significant enough to change the intensity;  $\nu_0$  is approximated to be coverage independent in the calculation. Also,  $\tilde{U}(0) = 0$  at  $\theta \rightarrow 0$ ; no dipole coupling occurs as the total coverage  $\theta$  approaches zero. From Equation (18), IR field absorption per adsorbate,  $I(\theta)/\theta$ , at  $\theta$  is a factor of  $\gamma_R^2$  less than at zero coverage; note that  $\gamma_R = 1$  at  $\theta \rightarrow 0$ . Experimentally, we obtain  $\gamma_R$  from the IR absorption cross-section:

$$\gamma_R = \sqrt{\frac{I(\theta)/\theta}{I_0}} \quad (20)$$

where  $I_0 = \lim_{\theta \rightarrow 0} [I(\theta)/\theta]$



Using the result in Equation (12) at zero frequency, electrostatic field, we obtain

$$\gamma_{DC} = \frac{1}{1 + (\alpha_e + \alpha_v)\tilde{U}(0)}. \quad (22)$$

For CO,  $\alpha_v/\alpha_e \approx 0.1$  [7,18], so the model predicts that with a single species the screening factors  $\gamma_R$  and  $\gamma_{DC}$  are nearly equal. For CO on Pt(111), two different species are observed. The line of derivation along the standard model can be extended straightforwardly. While the final results for both  $\gamma_R$  and  $\gamma_{DC}$  become much more complicated, the major conclusion stands:  $\gamma_R \approx \gamma_{DC}$ .

As indicated above,  $\gamma_R$  can be measured in RAIRS. In Chapter 3, we showed that  $\gamma_{DC}$  can be determined in the Stark tuning rate measurements. Usually, the standard model provides good explanation for RAIRS data. The Stark tuning rate measurement provides another aspect to test the standard model.

## II-2. Determination of $\alpha_v$ , $\alpha_e$ , and $\tilde{U}(0)$

In the standard model, physical and chemical effects are divided rather distinctively. From Equation (16), observed frequency  $\nu^*$  is equal to singleton  $\nu_0$  when the dipole coupling is turned off by setting  $\tilde{U}(0) = 0$ . In the model, the frequency difference between  $\nu^*(\theta)$  and  $\nu_0(\theta)$  at  $\theta$  is attributed to a "physical effect" (dipole coupling), while the difference between  $\nu_0(\theta)$  and  $\nu_0(0)$  (singleton frequency at near zero coverage) is attributed to "chemical effect". The coverage-dependent  $\nu_0$  is considered to be attributable to charge rearrangement between surface atoms and adsorbates.

The singleton frequency  $\nu_0$  is determined from the dilute limit of isotope substitution experiments. The experiments are carried out with fixed total adsorbate coverage. One measures the vibrational frequency of adsorbate in a uniform molecular layer, say  $^{12}\text{C}^{16}\text{O}$ . The next step is to partially substitute  $^{12}\text{C}^{16}\text{O}$  by a different isotope of CO,  $^{13}\text{C}^{18}\text{O}$  for example. Because  $\nu \propto \sqrt{1/\mu}$ , the frequencies of the two isotopes are different. For CO on Pt(111), the difference can be as big as  $100\text{ cm}^{-1}$  and can significantly reduce the coupling between oscillators, while the chemical interactions should be independent of isotope. When  $^{13}\text{C}^{18}\text{O}$  replaces almost all the  $^{12}\text{C}^{16}\text{O}$ , the coupling effect to  $^{12}\text{C}^{16}\text{O}$  is considered to be about zero. This condition is called dilute limit and the vibration frequency of  $^{12}\text{C}^{16}\text{O}$  measured at the dilute limit is called singleton frequency.

In applying the standard model for a quantitative analysis, determining the values of three parameters,  $\alpha_s$ ,  $\alpha_s$ , and  $\tilde{U}(0)$ , is critical. In earlier stage of studying CO on Pt(111), for example, Mahan and Lucas [4] employed a gas phase value for  $\alpha_s$ . They also determined  $\alpha_s$  from analyses of EELS and RAIRS measurements; their value for  $\alpha_s$  is quite similar to the gas phase value because they did not take screening (due to surrounding adsorbates) into account. As a consequence, they were not able to obtain a correct frequency shift in this case; their calculated frequency-shift is far too small.

Later, Persson and his co-workers [7,18] combined the standard model with isotope substitution measurements to determine correct values for  $\alpha_s$ ,  $\alpha_s$ , and  $\tilde{U}(0)$  that enabled them to reproduce the correct frequency shift and absorption intensity for CO on Cu [18]. For  $\alpha_s$  of CO molecules, the value obtained from their calculations is about four times bigger in adsorbed phase than in gas phase. The difference is related to significant charge rearrangement between CO and metal atoms, a chemical effect [7,20]. Values of

$\alpha_v$  and  $\alpha_s$  employed in our analysis for CO on Pt(111) are obtained by this means by Schweizer et al [21].

One can also estimate  $\tilde{U}(0)$  using classical approaches that require the knowledge of adlayer structure and the spacing between adsorbed molecule and image plane,  $d$  (Note that  $\tilde{U}(0) = \sum_{j \neq i} U_{ij}$  with  $U_{ij} \propto 1/x_{ij}^3$ ; where  $x_{ij}$  is the distance between molecules  $i$  and  $j$ , and the summation includes both real and image dipoles). Usually, the adlayer structure is determined from a low energy electron diffraction (LEED) measurement [22]. Using LEED to determine surface (two-dimensional) structure is very similar to using x-ray diffraction to determine the bulk (three-dimensional) structure of a crystal. However, due to the small mean free path of an electron with the energy range (around 100 eV) applying to the LEED measurement [23], observed LEED pattern is restricted to surface only. With progress in instrumentation, it may be possible to measure adlayer structure more directly by using a scanning tunneling microscope [24].

The concept of image plane in classical electrodynamics, for  $d$  greater than  $500 \text{ \AA}$ , is considered clear. However, the definition of image plane becomes ambiguous when  $d$  is very close, say within a couple of  $\text{\AA}$ . To simplify the problem, a transition metal in this case is approximated by a jellium model [18,25] that replaces the discrete ion cores with a uniform, positive charge background with a density equal to the spatial average of the ion charge distribution. The distribution of the positive charge background is assumed to have a sharp edge where the charge density goes discontinuously to zero. This sharp edge is called the "jellium edge". The jellium edge is set at one half of the spacing between neighboring metal molecules, i.e., by  $a/4$  where  $a$  is the metal lattice constant as indicated in Figure 6-2 [18]. Electrons are free in a jellium model and spill out into the vacuum region, creating an electrostatic

dipole layer at the surface. There is no sharp edge to the electron distribution. We can, however, locate an effective surface, or image plane, at

$$z_0 = \int_{-x}^x dz \left( z \frac{dn(z)}{dz} \right) \quad (23)$$

where  $n(z)$  is electron density and  $z_0$  is the distance between jellium edge and image plane. Consequently, the spacing between an adsorbed molecular dipole and image plane is approximately, as shown in Figure 6-2

$$d = d_{Cu-C} + \frac{1}{2}d_{C-O} - \frac{1}{4}a - z_0 \quad (24)$$

where Cu, C, and O refer to surface copper atoms, carbon, and oxygen atoms, respectively, in the case of CO on Cu(100). Usually  $d$  is very close to 0.8 - 1 Å. For CO on Cu and Pt,  $\tilde{U}(0)$  is actually not very sensitive to the exact value of  $d$ .

### II-3 Summary

In summary, the standard model provides a way to estimate screening of an applied field. For an ordered array of identical molecules, the screening factor can be written as

$$\gamma = \frac{1}{1 + \alpha \tilde{U}(0)} \quad (11)$$

where  $\tilde{U}(0) = \sum_{j \neq i} U_{ij}$ . Suppose  $\alpha$  is Lorentzian as a function of optical frequency  $\nu$ :

$$\alpha(\nu) = \alpha_e + \frac{\alpha_v}{1 - (\nu/\nu_0)^2 - i[\Delta/\nu_0]} \quad (10)$$

where  $\nu_0$  is the resonant frequency,  $\Delta$  is the width, and  $\alpha_e$  and  $\alpha_v$  are the electronic and vibrational polarizabilities, respectively. Then it has been

shown that the effect of  $\alpha_e$  is to reduce the IR cross section per molecule by the factor  $(\gamma_R)^2$ , where

$$\gamma_R = \frac{1}{1 + \alpha_e \tilde{U}(0)}. \quad (21)$$

The effect of  $\alpha_e$  on the IR cross section is the same as if  $E_{loc}$  had been reduced at all  $\nu$  by a factor  $\gamma_R$ . The same model predicts that at  $\nu = 0$

$$\gamma_{DC} = \frac{1}{1 + (\alpha_e + \alpha_v) \tilde{U}(0)}. \quad (22)$$

For CO,  $\alpha_v/\alpha_e \approx 0.1$  [7,18], so the model predicts that with a single species the screening factors  $\gamma_R$  and  $\gamma_{DC}$  are nearly equal.

### III. Experimental

Technical details such as sample preparation and RAIRS, EVS and TPD method used in the experiments are described in Chapter 2. The CO overlayer was prepared by dosing with the sample at 200 K, annealing at 260 K, and finally cooling back to 200 K before beginning IR spectroscopy. During EVS, a 100 kHz potential was applied between the sample and a spherical counter electrode. The rms average of static electric field applied to the surface, weighted by light intensity at the surface, was measured to be about  $3 \times 10^4$  V/cm. The CO coverage was determined with TPD. The TPD coverage was referenced to the 0.5-ML coverage obtained by saturating the surface with CO at 200 K and then annealing at 298 K. The present IR spectra are of the C=O stretch mode of atop  $^{13}\text{C}^{18}\text{O}$ . The resolution for the diode laser was about  $0.3 \text{ cm}^{-1}$ . The angle of incidence of the light was  $85.0 \pm 0.2^\circ$ .

#### IV. Results

Spectra of CO on Pt(111) obtained with RAIRS and EVS are shown in Figures 6-3 and Figure 6-4. The RAIRS and EVS spectra at each coverage were measured sequentially. Similar spectra measured on other days are not shown in these figures, but are included in the analysis presented below. Numerous other RAIRS studies of CO on Pt(111) in UHV have been reported [6,21,22,26,27,28,29,30,31,32,33,34,35,36,37,38]. In Figures 6-5 and 6-6 we compare our data with other measurements on single-crystal samples for which sufficient information was reported to extract the frequency and integrated intensity as a function of coverage. The coverage dependence of our data is in general agreement with earlier results.

In Figure 6-5, we present the peak frequency as a function of coverage; to facilitate comparison, we have scaled our measured frequencies by a factor of 1.049 to correct for the difference in reduced mass between  $^{13}\text{C}^{18}\text{O}$  and  $^{12}\text{C}^{16}\text{O}$ . Our measured integrated intensities are presented in Figure 6-6, together with those of other groups. The intensities reported by Beckerle et al. [27], using an angle of incidence of  $87^\circ$ , are a factor of  $2.6 \pm 0.2$  larger than ours, measured at  $85^\circ$ , while the expected ratio of 1.14 is significantly smaller [39]. The difference between the two experiments is not understood. The line widths are consistent, but the peak absorptions are not: With 0.5 ML coverage, we saw a FWHM of  $\approx 3.5 \text{ cm}^{-1}$  at 200 K in our fully resolved spectra, and a peak absorption (on four different days) of 5.5%, 5.8%, 6%, and 7%; at the same coverage, Beckerle et al. saw a FWHM of  $3.5 \text{ cm}^{-1}$  at 150 K using a spectrometer slit width of  $0.9 \text{ cm}^{-1}$ , and a peak absorption of 14.5%. The angle of incidence was not reported for the other data sets. It is noteworthy that none of the intensity curves extrapolate to the origin; presumably this is due to systematic errors in the coverage determination or background subtraction. As a result,

determinations of the IR absorption cross section per molecule at very low coverages are subject to large uncertainties.

The spectra in Figures 6-3 and 6-4 are sensitive to  $\gamma_{DC}$  and  $\gamma_R$ . One finds  $\gamma_R$  from RAIR spectra, as indicated in Equation (20):

$$\gamma_R \propto \left( \int \frac{\Delta R}{R} d\nu / \theta_a \right)^{1/2} \quad (25)$$

where  $\theta_a$  is the coverage of atop CO; both bridge and atop CO are observed on Pt(111) and we focus on atop CO spectra here. The data are also sensitive to the coverage dependence of the screening of the static electric field. The measured Stark tuning rate (or external field Stark tuning rate) from equivalent coverage RAIRS and EVS spectra is

$$(d\nu/dE_0) = \gamma_{DC}(d\nu/dE_{loc}). \quad (26)$$

Here,  $E_0$  and  $E_{loc}$  are the static applied and local electric fields, respectively (also see Chapter 3). In the approximation that the response of the molecule to  $E_{loc}$  is independent of coverage, then  $(d\nu/dE_{loc})$ , the intrinsic or local field Stark tuning rate, is independent of coverage and

$$\gamma_{DC} \propto (d\nu/dE_0). \quad (27)$$

A plot of  $(d\nu/dE_0)$  versus  $\theta$  is shown in Figure 6-7a. If the standard model is correct, individual molecules independently interact with  $E_{loc}$ , and the observed  $(d\nu/dE_0)$  versus  $\theta$  should have the same functional form as  $\gamma_R$ .

The coverage dependence of  $\gamma_{DC}$  and  $\gamma_R$  are compared in Figure 6-7b. Both are normalized to the values at 0.5 ML coverage. To obtain  $\gamma_R$  from Equation (8), it is necessary to know  $\theta_a$ . To estimate  $\theta_a$  from  $\theta$  we used the experimental correlation observed by Mieher et al. [40] and shown in Figure 5-7 of Chapter 5. There is more scatter in  $\gamma_R$  at low coverage than at high coverage. This is probably due to error in measured  $\theta$ . Since  $\gamma_R$  is related to

the intensity per atop CO it is very sensitive to error in measured  $\theta$  at low coverage.

## V. Discussion

Both  $\gamma_R$  and  $\gamma_{DC}$  in Figure 6-7b decrease monotonically with increasing total CO coverage, as one would expect; with more CO on the surface there is more screening. But the coverage dependence of the two quantities is not the same, and this difference is surprising. The standard model of dipole-dipole coupling would predict that  $\gamma_R \approx \gamma_{DC}$ . This prediction is rigorous if all the molecules are equivalent. Because of the statistical distribution of adsorbates and the presence of two species (bridge and atop), the true situation is more complicated, but the large systematic difference between  $\gamma_R$  and  $\gamma_{DC}$  remains inconsistent with the standard model.

One explanation for the difference between  $\gamma_R$  and  $\gamma_{DC}$  in Figure 6-7b is that IR and static electric are screened differently. There is reason to expect some difference between  $\gamma_R$  and  $\gamma_{DC}$ , but a difference as large as we observe is unexpected. Jellium models predict [41] only a small change in distance between the image plane and the outermost layer of atomic nuclei between  $\nu = 0$  and  $2000 \text{ cm}^{-1}$ . Ab initio calculations of  $\gamma_{DC}$  at the Al(100) [42] and Ag(100) [4] surfaces have found a strong dependence on lateral position, but the frequency dependence has not been investigated. The standard dipole - dipole coupling model, based on the data of Schweizer et al. [21] for CO on Pt(111), and with  $1 \text{ \AA}$  spacing between the dipole moment center and the image plane for both CO species, bridge and atop, gives  $\gamma_R = 1$  at  $\theta = 0$  and  $\gamma_R = 0.71$  at  $\theta = 0.5$ . (The  $1 \text{ \AA}$  distance was used by Crossley and King in Ref. [6]. Independent estimates of  $0.41 \text{ \AA}$  and  $1.29 \text{ \AA}$  are discussed near the end of this section.) The standard model is consistent with a linear fit to our data for  $\gamma_R$ . The standard



model would also predict the same coverage dependence for  $\gamma_{DC}$ , which is inconsistent with our data.

In the standard model,  $\gamma_R$  and the integrated absorption are related through a sum rule. It is plausible that the same rule continues to apply in situations where the nuclei and surrounding charge move together. The situation with CO on Pt(111) is more complicated: a current flows between the molecule and the metal as the molecule vibrates. This current makes an important contribution to IR absorption. On a transition metal, charge exchange between the  $2\pi^*$  orbital of adsorbed CO and the metal generally enhances  $e^*$  by about a factor of two [7,18,20,43] as discussed in section II-2. In particular, for CO on Pt(111) [21] the vibrational polarizability of atop CO is  $\alpha_v = 0.22 \text{ \AA}^3$ , so  $e^*$  is a factor 1.9 larger than in free CO. The IR absorption is proportional to  $(e^*)^2$ . Direct evidence of current between adsorbed CO and Pt is seen with nuclear magnetic resonance (NMR) [44].

Even with current between the molecule and the metal, it is still true that C and O nuclei vibrate in response to  $E_{loc}$  acting on them at the IR frequency. The vibration of the C and O nuclei is ultimately responsible for the IR absorption. Likewise, the Stark effect arises because static  $E_{loc}$  changes the equilibrium positions of the nuclei [43,45]. As CO coverage changes, however, there is no simple relationship between vibrational amplitude of the nuclei at a fixed IR frequency and the integrated IR absorption. Proportionality between integrated IR absorption per molecule and  $(\gamma_R)^2$  depends on a subtle sum rule, which has not been proven for a situation as complicated as this. An excellent summary of screening calculations has been given by Mahan and Subbaswamy [46].

A chemical effect -- that is, variation of the properties of the individual molecules with coverage -- could in principle account for the observed

difference between  $dv/dE_0$  and  $\gamma_{IR}e^*$ , but such an explanation can be excluded. As indicated in Chapter 3, Lambert has shown [47] that for CO,  $(dv/dE_0) \propto e^* a_{30}$ , where  $a_{30}$  is the coefficient of the cubic term in the Taylor expansion of the CO potential. Because both of the quantities plotted in Figure 6-7b are proportional to  $e^*$ , no variation of this quantity with coverage (caused, for example, by a variation in  $2\pi^*$  backbonding) can account for the difference between them. A chemical explanation would require a strongly coverage-dependent  $a_{30}$ ; its value at  $\theta = 0.15$  would need to be  $\approx 1.6$  times larger than at  $\theta = 0.5$ . This could occur only if the dissociation energy  $D_e$  of CO at the lower coverage were  $\approx 2.5$  times smaller than at  $\theta = 0.5$ , since for a Morse potential  $D_e \propto 1/(a_{30})^2$ . (As indicated in Chapter 4,  $D_e$  is in the range 140 - 200 kcal/mole at  $\theta = 0.5$  [48]). According to Weinberg and Merrill [49], such a large change in  $D_e$  would change the C-O bond length by 0.4 Å; a LEED study by Ogletree et al. [50] found that the bond length changes by less than 0.03 Å. a chemical explanation for our results can therefore be ruled out.

Our measured values of  $(dv/dE_0)$  are shown in Figure 6-7a. In the limit of low coverage, screening by coadsorbates should be negligible, so if there is no other screening mechanism  $(dv/dE_0)$  should approach  $(dv/dE_{loc})$ . From our data, in the limit of low coverage,  $(dv/dE_0) = (7.5 \pm 0.9) \times 10^{-7} \text{ cm}^{-1}/(\text{V/cm})$ . As mentioned in Chapter 3, surprising results for  $(dv/dE_0)$  were reported in a previous experiment [1] with CO on Pt(335). The Pt(335) surface is stepped with four-atom-wide (111) terraces. In the experiment, RAIRS and EVS were used to study atop CO both at edge sites and at terrace sites. The observed  $(dv/dE_0)$  for CO at edge sites was at least ten times larger than for CO at terrace sites. Our measured value of  $(dv/dE_0)$  for CO on Pt(111) is quite comparable to  $(7.5 \pm 2.0) \times 10^{-7} \text{ cm}^{-1}/(\text{V/cm})$  of  $(dv/dE_0)$  for edge CO, while it is much larger than the value of  $(dv/dE_0)$ ,  $< 0.8 \times 10^{-7} \text{ cm}^{-1}/(\text{V/cm})$  for terrace CO on Pt(335). We thus

conclude that  $(d\nu/dE_0)$  of terrace CO on Pt(335) is significantly suppressed rather than that  $(d\nu/dE_0)$  of edge CO being significantly enhanced.

Our observation of  $\gamma_R \approx \gamma_{DC}$  with CO on Pt(111) makes a physical explanation that accounts for the  $(d\nu/dE_0)$  data of CO on Pt(335) more plausible. The observed  $(d\nu/dE_0)$  for CO at edge sites was at least ten times larger than for CO at terrace sites. However, the IR cross section of CO is about the same at either site. In other experiments, Reutt-Robey et al. [51] have also found that the IR cross section of CO on stepped Pt is the same at edge and terrace sites, while Borguet and Dai [52] have found some evidence that on Cu, electric field enhancement slightly increases the IR cross section of CO at edge sites. If  $E_{loc}$  response of CO at edge (e) and terrace (t) sites is assumed to be about the same, then  $\gamma'_{IR} \approx \gamma'_{DC}$  but  $\gamma'_{DC} > 10\gamma'_{DC}$ . This is similar to, but even more dramatic than, the effect that we observe with CO on the flat Pt(111) surface.

Similar measurements have been reported by others for CO at a Pt(111) electrode in electrochemical cells [11,12,13,14,15,16,17]. In the electrochemical experiments, the strong dependence of  $E_{loc}$  in the double layer on electrode potential  $\Phi$  is used to vary the resonant vibrational frequency of the adsorbed CO. The measured quantity is  $(d\nu/d\Phi)$  where  $\Phi$  is the Pt(111) electrode's potential relative to a reference electrode. The electrochemical experiments observe a factor of two change in  $(d\nu/d\Phi)$  between low CO coverage and high CO coverage [11] similar to the coverage dependence of  $(d\nu/dE_0)$  seen in UHV. A model of the double layer relates  $E_{loc}$  to  $\Phi$ . Consequently, the electrochemical experiments can also be used to estimate  $(d\nu/dE_{loc})$ . For an aqueous electrolyte, Chang et al. [11] found that  $(d\nu/d\Phi) = 44 \text{ cm}^{-1}/\text{V}$  with a CO coverage of 0.12 ML. Models of the aqueous double layer predict [43] that  $(dE_{loc}/d\Phi) \approx 2.8 \times 10^7 \text{ (V/cm)/V}$ . Consequently,  $(d\nu/dE_{loc}) \approx 16 \times 10^{-7} \text{ cm}^{-1}$

$1/(V/cm)$  at 0.12 ML. Consistent results are also obtained with non-aqueous electrolytes [13,17,53].

The difference between  $(dv/dE_{loc})$  from experiments in vacuum and at the electrochemical double layer for CO on Pt(111) is very surprising. A previous measurement of  $(dv/dE_{loc})$  for CO on Ni(100) in UHV [43] is consistent with  $(dv/d\Phi)$  observed for CO on other metals when allowance is made for the effect of the metal on  $e^*$ . (No IR spectra with CO on Ni at the double layer have been reported.) The present [9,26] experiment of CO on Pt(111) provides the first direct comparison between  $(dv/dE_{loc})$  measured in UHV and at the electrochemical double layer.

A possible explanation for the apparent difference in  $(dv/dE_{loc})$  between UHV and the double layer is that in UHV there is a significant amount of screening of  $E_0$  by conduction electrons from the metal; this screening is much less at the electrochemical double layer. The model of Schmickler and Henderson [54] for the aqueous double layer includes a 3 eV repulsion barrier that electrons from the metal must surmount to enter the liquid. There is experimental evidence [55] for such a barrier.

The plausibility of screening as the explanation for the apparent difference in Stark tuning rate in UHV and in electrochemical cells can be tested by comparison to simple models. For screening to explain the observed difference, conduction electrons on Pt(111) in UHV would need to cause  $\gamma_{DC} < 0.5$ . This is only possible if the image plane is outside the point at which the local field is evaluated.

One estimate comes from fits of the standard model to RAIR spectra of CO on Pt(111). The best fit is with the center of the CO bond  $\approx 1.1 \text{ \AA}$  relative to the image plane.

A free-electron jellium model gives another estimate.. A free-electron jellium model does not necessarily apply to a d-band metal like Pt [56], but it is a reasonable first approximation. The equivalent free-electron density is estimated as the formal valence charge of the Pt atom (8e) in each unit cell [57]; in atomic units, the radius of a sphere containing one electron is  $r_s = 1.45$ . The jellium model of Lang and Kohn [25] places the jellium edge on Pt(111)  $1.13 \text{ \AA}$  outside the top layer of atoms (half the layer spacing). They do not solve the model for  $r_s > 2$ , but a linear extrapolation puts the image plane  $0.89 \text{ \AA}$  outside the jellium edge. The total distance from the outer plane of metal atoms to the image plane is  $2.02 \text{ \AA}$ . In comparison, the measured [50] Pt-C bond length for atop CO on Pt(111) is  $1.85 \text{ \AA}$  and the C-O bond length is  $1.15 \text{ \AA}$ . The center of the C-O bond is  $2.43 \text{ \AA}$  outside the outer plane of metal atoms. Since the center of the C-O bond is outside the image plane,  $\gamma_{DC} > 0.5$ .

A third estimate comes from spectroscopic studies [58] of image potential induced surface states. On Pt(100), the distance from the outer plane of Pt atom nuclei to the image plane is  $1.05 \text{ \AA}$ . In the approximation that the distance between the jellium edge and the image plane is independent of crystal face, on Pt(111) the image plane is  $1.14 \text{ \AA}$  outside the outer plane of metal nuclei. Consequently, the center of the C-O bond is  $1.29 \text{ \AA}$  outside the image plane.

The available evidence does not support screening at the center of the C-O bond by conduction electrons as the source of the difference in apparent Stark tuning rates for CO on Pt(111) in UHV and in electrochemical cells.

In summary, our experimental data with CO on Pt(111) suggest that the CO coverage dependence of screening for the static electric field is stronger than it is for the IR electric field. Dipole coupling models, on the other hand, predict that the coverage dependence of screening should be the same for static and IR electric fields. Our quantitative measurement of  $(d\nu/dE_0)$  for CO

on Pt(111) indicates that  $(dv/dE_0)$  of CO on the (111) terrace of the stepped (335) is significantly suppressed. The suppression is possibly due to an extra screening of the static electric field on terrace sites. A quantitative difference in apparent  $(dv/dE_{loc})$  is also seen between CO on Pt(111) in UHV and at Pt(111) electrodes in electrochemical cells. We examined models of screening by conduction electrons to explain both effects. Conduction electrons screen the interaction between CO and the static electric field better than between CO and the IR field. Conduction electrons are also expected to screen CO at a vacuum interface more than at an electrochemical interface. Present understanding of conduction electron screening, however, suggests that it is too small to explain our data. Also, the treatment of image effects needs to be significantly improved. It is clear that a classical model is *not* a good approximation, and the best approaches just treat  $\tilde{U}(0)$  as a parameter.

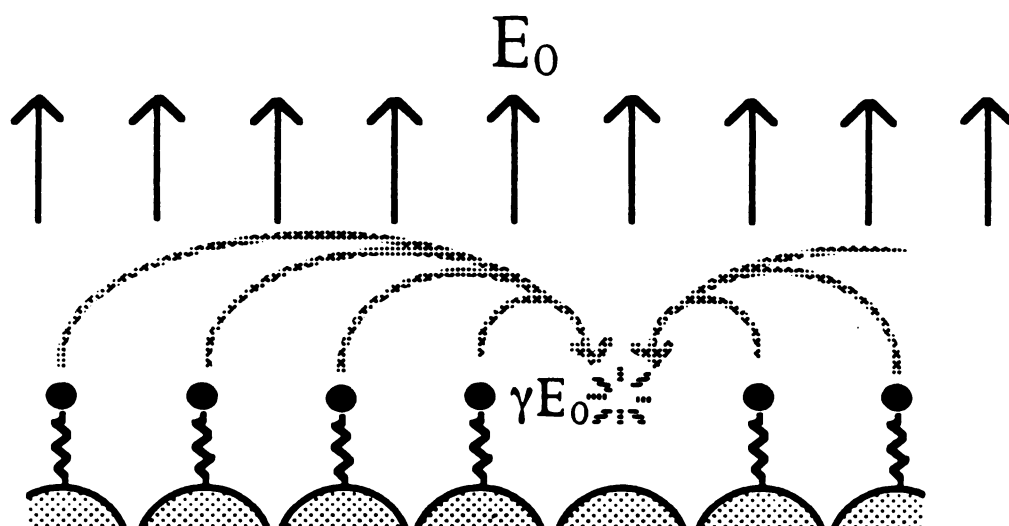


Figure 6-1. Sketch showing the partial cancellation of the applied field  $E_0$  due to the induced fields from adsorbed molecules that are treated as polarizable points. This gives  $\gamma E_0$  to be the final field.

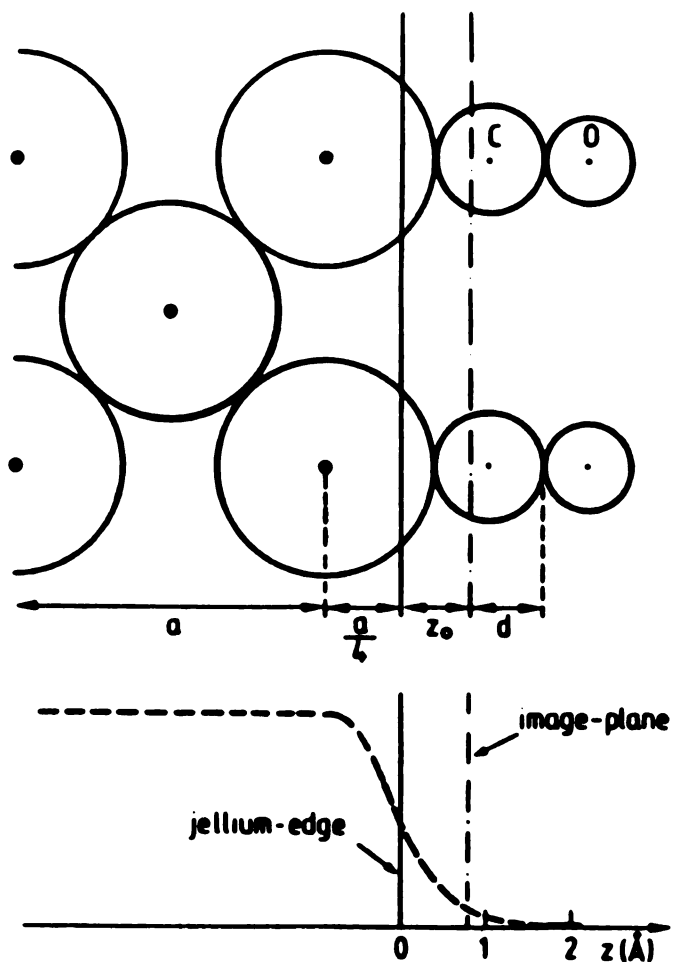


Figure 6-2. Illustration of the jellium edge and image plane. The jellium edge lies at  $a/4$  above the nuclei of the surface substrate layer;  $a$  is the lattice constant of the substrate. The position of the image plane and the spacing between the image plane and CO are discussed in the text (Persson and Liebsch [18]).



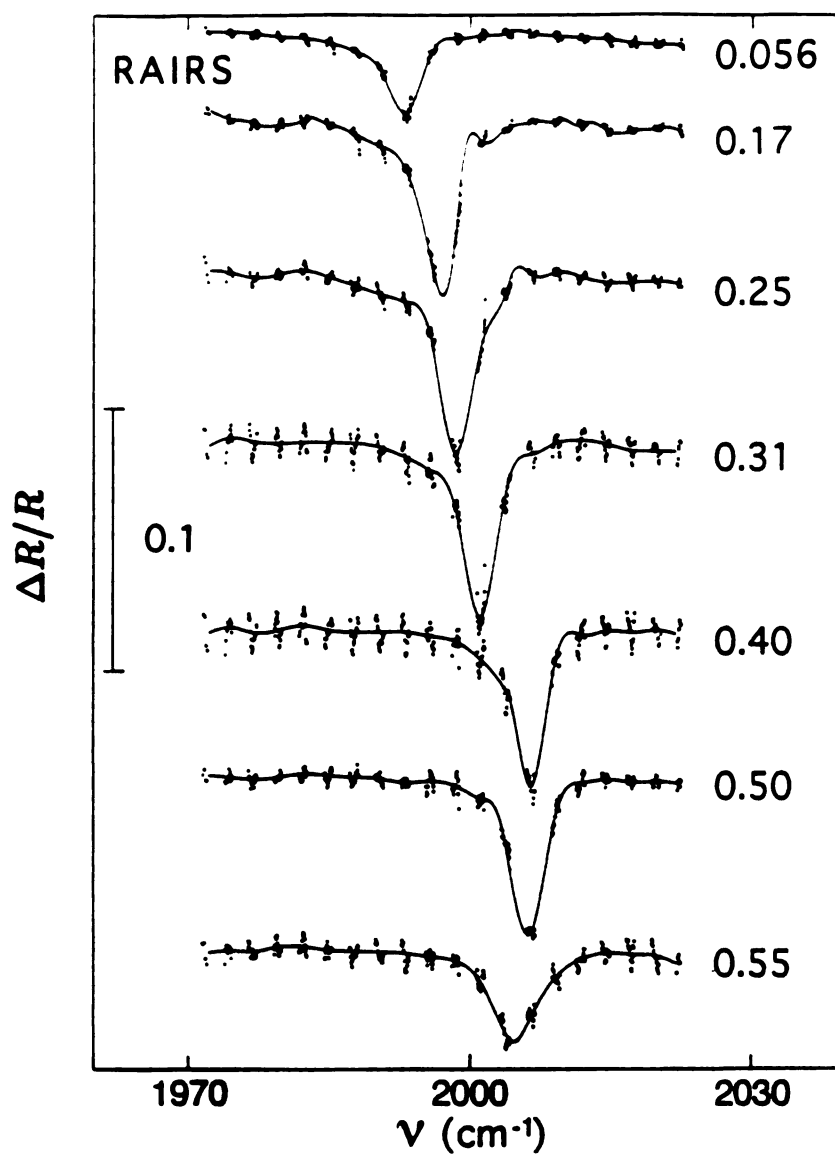


Figure 6-3. Vibrational spectra of the C=O stretch mode of atop  $^{13}\text{C}^{18}\text{O}$  on Pt(111) in UHV obtained with RAIRS. The CO coverages (in ML) are indicated. The curve is a smoothed fit to the data.

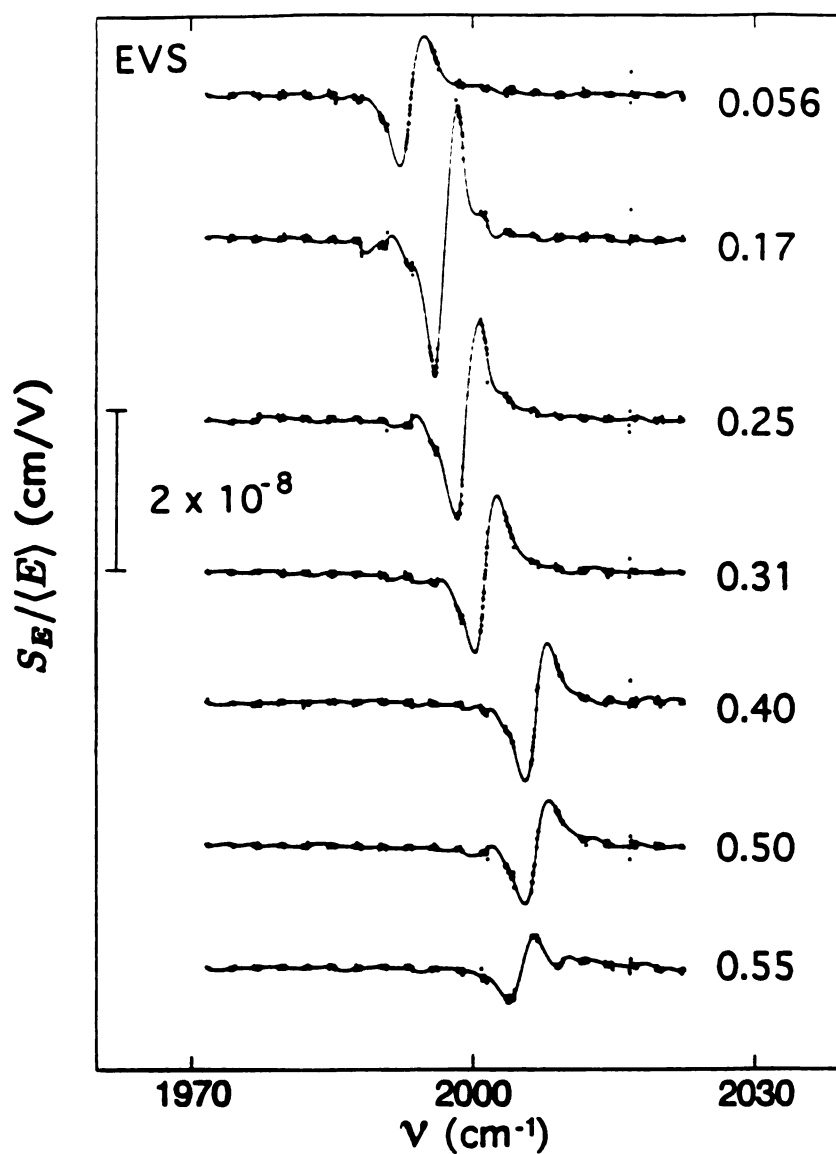


Figure 6-4. Vibrational spectra obtained with EVS that correspond to those in Figure 6-3. The measured  $S_E / \langle E \rangle$  is the fractional modulation of reflected intensity, normalized by  $E$  applied to the surface.

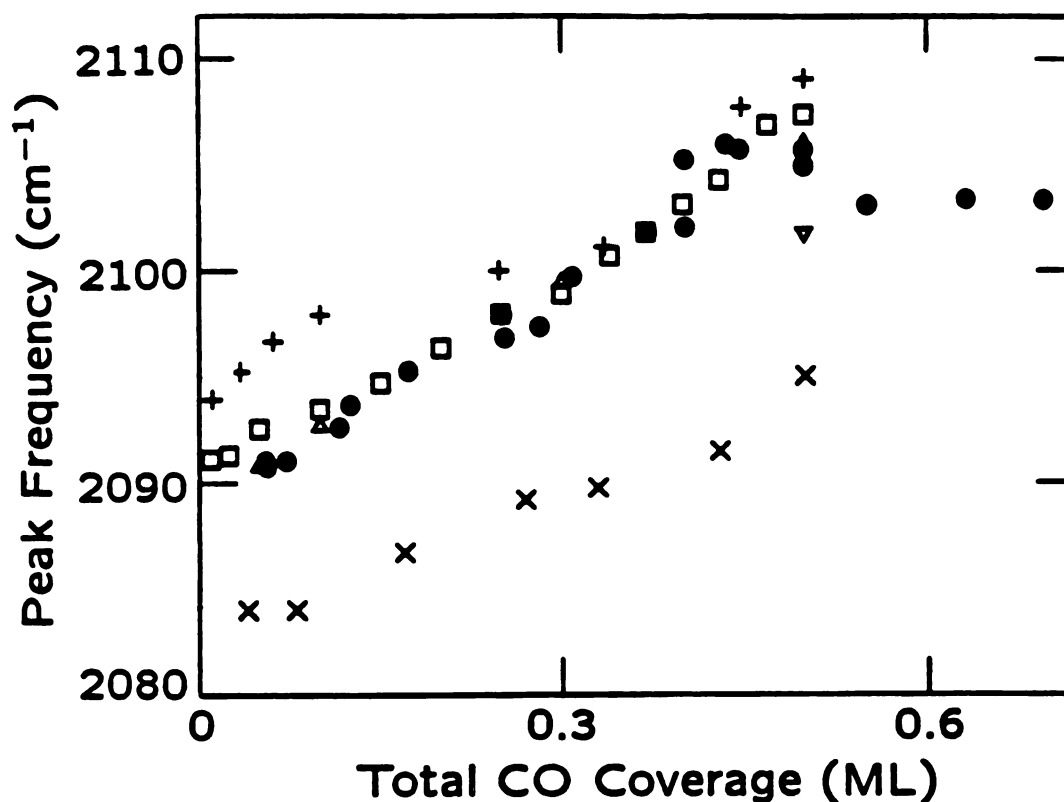


Figure 6-5. Frequency  $\nu$  of peak IR absorption vs total CO coverage. Our measured  $\nu$  for  $^{13}\text{C}^{18}\text{O}$  have been multiplied by the factor 1.049 to compare with  $\nu$  for  $^{12}\text{C}^{16}\text{O}$  (to account for the isotope difference). The sources of data are: ● this work (200 K), + Hayden and Bradshaw in ref. [31] (95 K), □ Tushaus et al. in ref. [38] (125 K), Δ Beckerle et al. in ref. [27] (150 K), ▽ Beckerle et al. in ref. [27] (300 K), and × Olsen and Masel in ref. [33] (300 K).

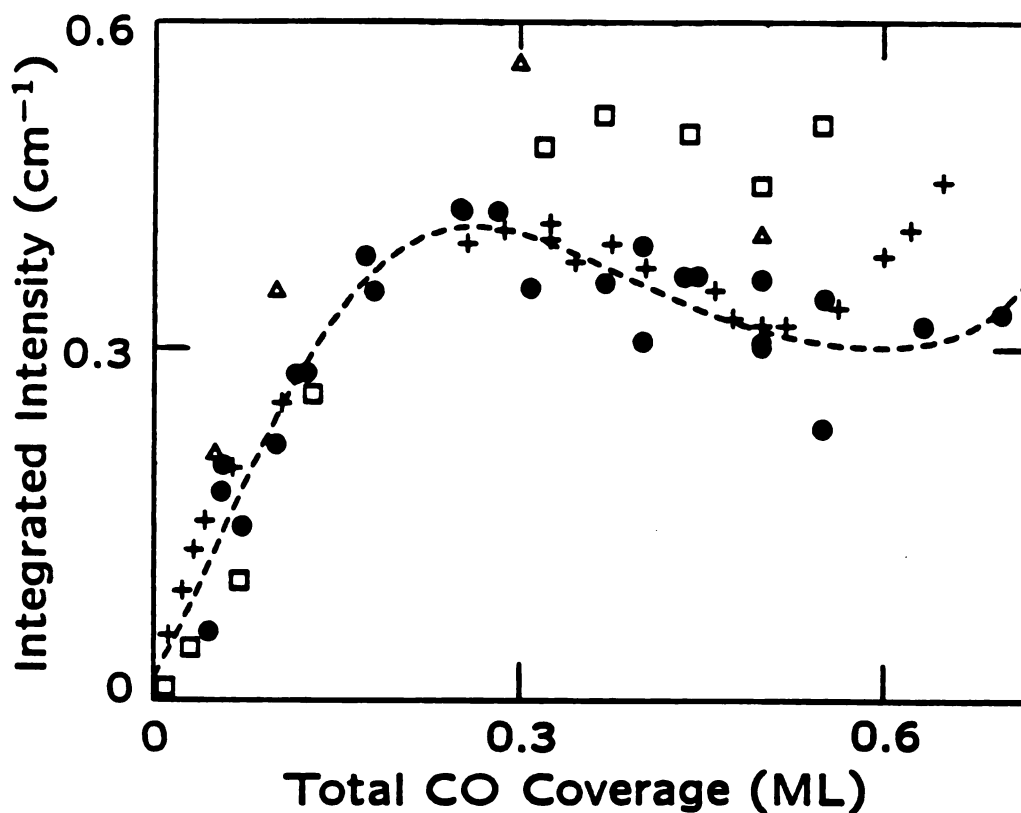


Figure 6-6. Integrated IR absorbance of CO vs total CO coverage. Our data are compared with previous experiments. The symbols have the same meaning as in Figure 6-5. A curve is fitted to our data as a guide to the eye. Different angles of incidence were used for the different experiments so exact agreement is not expected. In the plot, the data of Beckerle et al. ( $\Delta$ ) have been multiplied by a factor 0.5. The ratio of their intensity to ours, calculated as in Appendix of Ref. [43], is expected to be 1.14. The actual ratio is  $2.6 \pm 0.2$ .

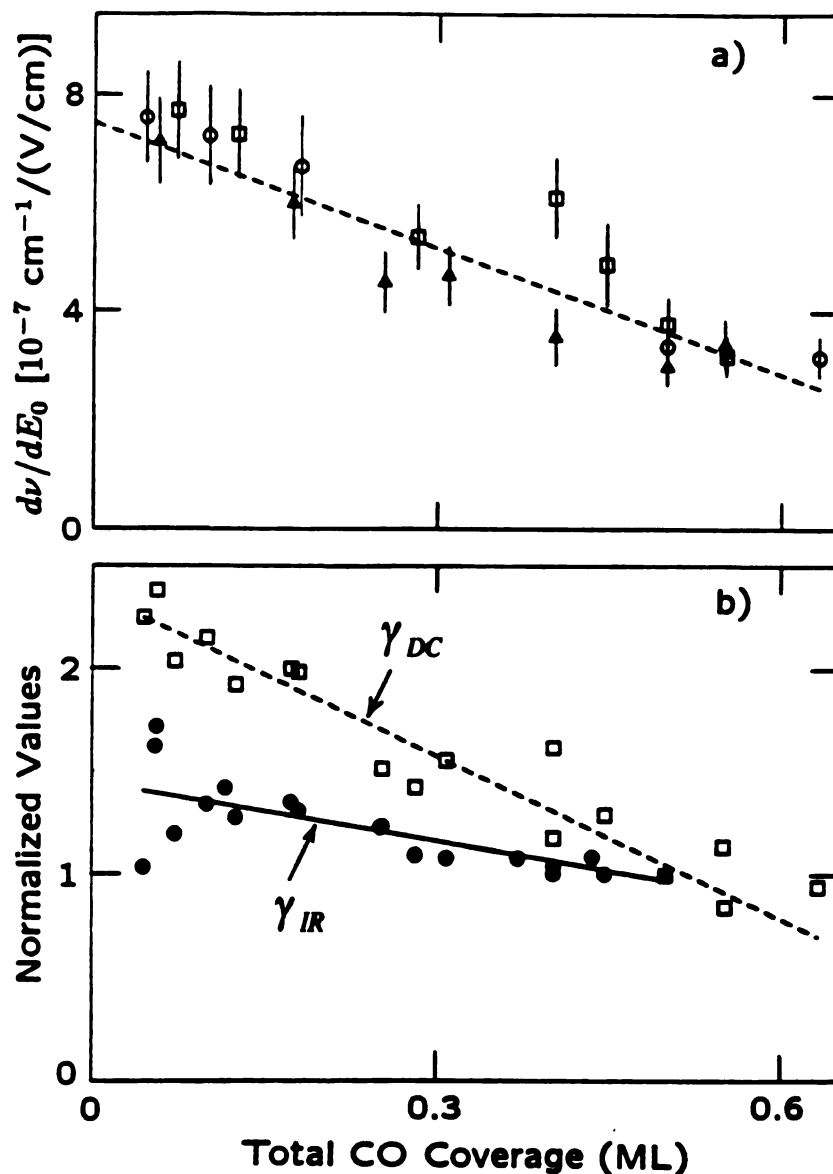


Figure 6-7. (a) Measured Stark tuning rate ( $d\nu/dE_0$ ) vs. total CO coverage. Data were taken on three different days as indicated by the three symbols. The error bars are  $1\sigma$  random error + systematic error.

(b) Comparison between the coverage dependence of  $\gamma_{DC}$   $\square$  [from Figure 6-7a and Equation (26) and  $\gamma_{IR}$   $\bullet$  [from Figure 6-6 and Equation (25)]. We assume that  $e^*$  and  $d\nu/dE_{loc}$  are independent of coverage. Both  $\gamma_{DC}$  and  $\gamma_{IR}$  are normalized to the values measured on the same day with 0.5 ML of CO. Linear fits to both sets of data are shown.

**References**

1. D.K. Lambert and R.G. Tobin, *Surf. Sci.* **232**, 149 (1990).
2. R.P. Eischens, S.A. Francis and W.A. Pliskin, *J. Phys. Chem.* **60**, 194 (1956).
3. R.A. Hammaker, S.A. Francis and R.P. Eischens, *Spectrochim. Acta* **21**, 1295 (1965).
4. G.D. Mahan and A.A. Lucas, *J. Chem. Phys.* **68**, 1344 (1978).
5. M. Scheffler, *Surf. Sci.* **81**, 562 (1979).
6. A. Crossley and D.A. King, *J. Chem. Phys.* **68**, 1344 (1977).
7. B.N.J. Persson and R. Ryberg, *Phys. Rev. B* **24**, 6954 (1981).
8. P. Hollins and J. Pritchard, *Prog. Surf. Sci.* **19**, 275 (1985).
9. J.S. Luo, R.G. Tobin and D.K. Lambert, (to be published).
10. D.K. Lambert, *Appl. Opt.* **27**, 3744 (1988).
11. S.C. Chang, L-W.H. Leung and M.J. Weaver, *J. Phys. Chem.* **93**, 5341 (1989).
12. S.-C. Chang and M.J. Weaver, *J. Chem. Phys.* **92**, 4582 (1990).
13. S.-C. Chang, X. Jiang, J.D. Roth and M.J. Weaver, *J. Phys. Chem.* **95**, 5378 (1991).
14. F. Kitamura, M. Takeda, M. Takahashi and M. Ito, *Chem. Phys. Lett.* **142**, 318 (1987).
15. F. Kitamura, M. Takahashi and M. Ito, *Chem. Surf. Sci.* **223**, 493 (1989).
16. L-W.H. Leung, A. Weichowski and M.J. Weaver, *J. Phys. Chem.* **92**, 6985 (1988).
17. J.D. Roth, S.-C. Chang and M.J. Weaver, *J. Electroanal. Chem.* **288**, 285 (1990).
18. B.N.J. Persson and A. Liebsch, *Surf. Sci.* **110**, 356 (1981).
19. R.G. Tobin, *Phys. Rev. B* **45**, 12110 (1992).

20. K. Herman, P.S. Bagus and C.W. Bauschlicher, Jr., *Phys. Rev. B* **30**, 7313 (1984).
21. E. Schweizer, B.N.J. Persson, M. Tushaus, D. Hoge and A.M. Bradshaw, *Surf. Sci.* **213**, 49 (1989).
22. G. Ertl, M. Neumann and K.M. Streit, *Surf. Sci.* **64**, 393 (1977).
23. T.N. Rhodin and J.W. Gadzuk, in *The Nature of the Surface Chemical Bond*, edited by T.N. Rhodin and G. Ertl, (Plenum, New York, 1979).
24. D.M. Eigler, P.S. Weiss, E.K. Schweizer and N.D. Lang, *Phys. Rev. Lett.* **66**, 1189 (1991).
25. N.D. Lang and W. Kung, *Phys. Rev. B* **7**, 3591 (1973).
26. J.S. Luo, R.G. Tobin, D.K. Lambert, F.T. Wagner and T.E. Moylan, *J. Electron Spectrosc. Relat. Phenom.* **54/55**, 469 (1990).
27. J.D. Beckerle, R.R. Cavanagh, M.P. Casassa, E.J. Heilweil and J.C. Stephenson, *J. Chem. Phys.* **95**, 5403 (1991).
28. D.S. Bethune, M.D. Williams and A.C. Luntz, *J. Chem. Phys.* **88**, 3322 (1988).
29. D.H. Ehlers, A.P. Esser, A. Spitzer and H. Luth, *Surf. Sci.* **191**, 466 (1987).
30. W.G. Golden, D.S. Dunn and J. Overend, *J. Catalysis* **71**, 395 (1981).
31. B.E. Hayden and A.M. Bradshaw, *Surf. Sci.* **125**, 787 (1983).
32. H.J. Krebs and H. Luth, *Appl. Phys.* **14**, 337 (1977).
33. C.W. Olsen and R.L. Masel, *Surf. Sci.* **201**, 444 (1988).
34. L.F. Sutcu, J.L. Wragg and H.W. White, *Phys. Rev. B* **41**, 8164 (1990).
35. L.F. Sutcu, H.W. White and J.L. Wragg, *Surf. Sci.* **249**, L343 (1991).
36. R.G. Tobin, R.B. Phelps and P.L. Richards, *Surf. Sci.* **183**, 427 (1987).
37. W.J. Tornquist and G.L. Griffin, *J. Vac. Technol. A* **4**, 1437 (1986).

38. M. Tushaus, E. Schweizer, P. Hollins and A.M. Brashaw, J. Electron Spectrosc. Relat. Phenom. **44**, 305 (1987).
39. To calculate the ratio of CO's IR absorption at ( $85^{\circ}$ ,  $2005\text{ cm}^{-1}$ ) and at ( $87^{\circ}$ ,  $2100\text{ cm}^{-1}$ ), Equation (A1) of Reference [43] was used with the dielectric constant of Pt interpolated from: M.A. Ordal, R.J. Bell, R.W. Alexander, Jr., L.L. Long and M.R. Querry, Appl. Opt. **24**, 4493 (1985).
40. W.D. Mieher, L.J. Whitman and W. Ho, J. Chem. Phys. **91**, 3228 (1989).
41. A. Liebsch, Phys. Rev. B **33**, 7249 (1986).
42. J.E. Inglesfield, Surf. Sci. **188**, L701 (1987).
43. D.K. Lambert, J. Chem. Phys. **89**, 3847 (1988).
44. P.-K. Wang, J.-P. Ansermet, S.L. Rudaz, Z. Wang, S. Shore, C.P. Slichter and J.H. Sinfelt, Science **234**, 35 (1986).
45. P.W. Fowler and A.D. Buckingham, Chem. Phys. **98**, 167 (1985).
46. G.D. Mahan and K.R. Subbaswamy, *Local Density Theory of Polarizability*, (Plenum, New York, 1990).
47. D.K. Lambert, Solid State Commun. **51**, 297 (1984).
48. The lower limit comes from: E. Shustarovich and A.T. Bell, Surf. Sci. **248**, 359 (1991). The high limit comes from combining the measured bond length from Reference [50] with Reference [49]. The difference in bond length between the two estimates is  $0.08\text{ \AA}$ .
49. W.H. Weinberg and R.P. Merrill, Surf. Sci. **39**, 206 (1973).
50. D.F. Ogletree, M.A. Van Hove and G.A. Somorjai, Surf. Sci. **173**, 351 (1986).
51. J.E. Reutt-Robey, D.J. Doren, Y.J. Chabal and S.B. Christman, J. Chem. Phys. **93**, 9113 (1990).
52. E. Borguet and H.-L. Dai, Chem. Phys. Lett. **194**, 57 (1992).



- 53. M.R. Anderson and J. Huang, *J. Electroanal. chem.* **319**, 335 (1991).
- 54. W. Schmickler and D. Henderson, *J. Chem. Phys.* **80**, 3381 (1984).
- 55. Y. Pleskov and Z.A. Rotenberg, in *Advances in Electrochemistry and Electrochemical Engineering*, edited by P. Delahay and C.W. Tobias, (Wiley, New York, 1978), Vol. 11, pp 1-124.
- 56. J.R. Smith, F.J. Arlinghaus and J.G. Gay, *J. Vac. Sci. Technol.* **18**, 411 (1981).
- 57. J.R. Smith, *Phys. Rev.* **181**, 522 (1969).
- 58. N.V. Smith, C.T. Chen and M. Weinert, *Phys. Rev. B* **40**, 7565 (1989).

## Chapter 7

### CONCLUSIONS

In conclusion, we have obtained several significant results from RAIRS and EVS measurements of CO on Pt(111) and EELS measurements of CO on Pt(335).

First, we determined that the Stark tuning rate of CO on the (111) terrace of a stepped Pt(335) surface is significantly suppressed compared to that of CO on the flat Pt(111) surface. We observe the Stark tuning rate of atop CO on Pt(111) at low coverage to be  $(7.5 \pm 0.9) \times 10^{-7} \text{ cm}^{-1}/(\text{V}/\text{cm})$ . Our result is very comparable to the Stark tuning rate of edge atop CO on Pt(335),  $(7.5 \pm 2.0) \times 10^{-7} \text{ cm}^{-1}/(\text{V}/\text{cm})$ , and nearly an order of magnitude larger than that of terrace atop CO,  $\leq 8.0 \times 10^{-8} \text{ cm}^{-1}/(\text{V}/\text{cm})$ , measured by Lambert and Tobin. This indicates that there is no significant enhancement for CO adsorbed at edges but a significant suppression for CO adsorbed on terraces.

We also found that the Stark tuning rate of CO on Pt(111) in UHV is about a factor of two smaller than that in electrochemical cells. This is the first direct comparison between the Stark tuning rate measured on the same metal surface in the two environments. This deviation is rather surprising since the Stark tuning rate of CO on Ni(100) measured previously in UHV is consistent with that observed for CO on other metals in electrochemical cells. Conduction electrons that screen CO at a vacuum interface more than at an electrochemical interface give a qualitative explanation, but present understanding of conduction electron screening suggests that the effect is too small to account for our data. A better model is needed.

The small Stark tuning rate of terrace CO on Pt(335) cannot be explained by a chemical mechanism. The chemical explanation requires a significant

enhancement of the quadratic term in the dipole moment function of terrace CO. This would result in significant enhancement of the overtone intensity for terrace CO in an EELS measurement. However, we observed no such enhancement. Our result shows that chemical differences at the two sites account for at most a small part of the effect. The data must be explained by an alternative, physical mechanism: a substantial difference in electrostatic screening between edge and terrace sites. The physical mechanism results in a surprising outcome -- the screening effect for the IR electric field is about the same at the two sites while that for the static field at terrace sites is at least ten times larger than at edge sites.

Our experimental data with CO on Pt(111) suggest that the CO coverage dependence of screening for the static electric field is stronger than it is for the IR electric field. This result is very important in supporting the physical explanation of the observed Stark effect of the two atop CO species on Pt(335). The difference between screening effects of the two fields for CO on Pt(335) is much more dramatic than that observed for CO on Pt(111). Since the screening effect is observable even for CO on the flat and simple Pt(111) surface, it is plausible that such an effect is enhanced for CO on the stepped and complicated Pt(335) surface.

One other surprising aspect of the screening effects of CO on Pt(111) is that our data contradict the prediction from a standard dipole coupling model. The standard model predicts that the screening effect is about equal for the IR and the static electric fields. The standard model usually gives good agreement with the measured screening effect for the IR field, while our measurement of CO on Pt(111) provides the first test of the standard model regarding the screening of the static electric field. We conclude that the standard model is

oversimplified, and a new theoretical approach is necessary as discussed below.

Finally, for the first time, our EELS and TPD measurements show comparable bridge CO coverage compared to atop CO coverage on Pt(335). Our data indicate that there are four CO species on Pt(335): edge atop, edge bridge, terrace atop, and terrace bridge. In contrast, previous measurements of CO on Pt(335) and on the similar stepped Pt(112) surface observed only two atop CO species. We have proposed a model for the populations of all four species as a function of CO coverage that explains our TPD and EELS data. The interpretation of the EELS data is sensitive to certain assumptions. The model should therefore be taken only as indicative of general trends. We have used the model to analyze the EELS overtone intensity of CO on Pt(335). In all our analyses of CO on Pt(335), bridge CO is negligible only at very low coverage:  $\theta \leq 0.12$  ML.

Our intriguing results should stimulate further theoretical and experimental work. Our results are quite significant in many ways. First, it is surprising to have new findings on the screening effect of the static and IR fields in one of the most studied systems: CO on the flat Pt(111). Prior to our work, it was believed that the standard model should, at least, explain the data obtained from relatively simpler systems like CO on Pt(111). Most importantly, our data suggest that the observed screening effects for the static and IR fields are fundamentally different. This difference is particularly surprising because the frequencies for both fields,  $< 2500 \text{ cm}^{-1}$ , are much smaller than the plasma frequency,  $\approx 50000 \text{ cm}^{-1}$ : Frequency dependence of the electronic properties should be insignificant. Therefore, it is unlikely that minor modifications of current models can account for our observed data. Results from CO on both Pt(111) and Pt(335) indicate that there seems to be something

qualitatively wrong with our picture of screening at surfaces. New physics needs to be included.

It was also previously believed that the Stark tuning rate measured in UHV could be directly used to explain the observed Stark shift in chemical cells. Our conclusion indicates that this shift is more subtle than we previously thought. For electro-chemists to better use the information obtained from the Stark effect measurements in UHV, it is important to have a model that explains the difference between the Stark effect observed in UHV and in electrochemical cells.

Our observation of bridge CO species on the high step density Pt(335) surface should stimulate other researchers who have studied the same or similar surfaces but have not included bridge CO in their analyses to review their conclusions.

In summary, we hope this work will be of interest to surface scientists interested in using stepped surfaces as models for practical catalysts or in distinguishing electrostatic from chemical effects in chemisorbed systems, to electro-chemists seeking a quantitative understanding of adsorption at the metal-electrolyte interface, and to theorists working to understand the complex response of metal surfaces to applied electric fields.